

Advanced Characterization of Large Zeolite Crystals and Their Use in the Methanol-to-Hydrocarbons Process

Geavanceerde Karakterisering van Grote Zeoliet Kristallen
en Hun Gebruik in het Methanol-naar-Koolwaterstoffen Proces
(met een samenvatting in het Nederlands)

Proefschrift

ter verkrijging van de graad van doctor aan de Universiteit Utrecht op gezag van
de rector magnificus, prof. dr. H.R.B.M. Kummeling, ingevolge het besluit
van het college voor promoties in het openbaar te verdedigen op woensdag
21 november 2018 des middags te 4.15 uur

door

Özgün Attila

geboren op 15 maart 1988 te Izmir, Turkije

Promotor: Prof. dr. ir. B. M. Weckhuysen

This PhD Thesis was accomplished with financial support from the European Research Council (ERC) in the form of an Advanced ERC grant (321140).

"We don't have to save the world. The world is big enough to look after itself. What we have to be concerned about is whether or not the world we live in will be capable of sustaining us in it."

Douglas Adams, 2001

Author: Özgün Attila

Cover design: Özgün Attila

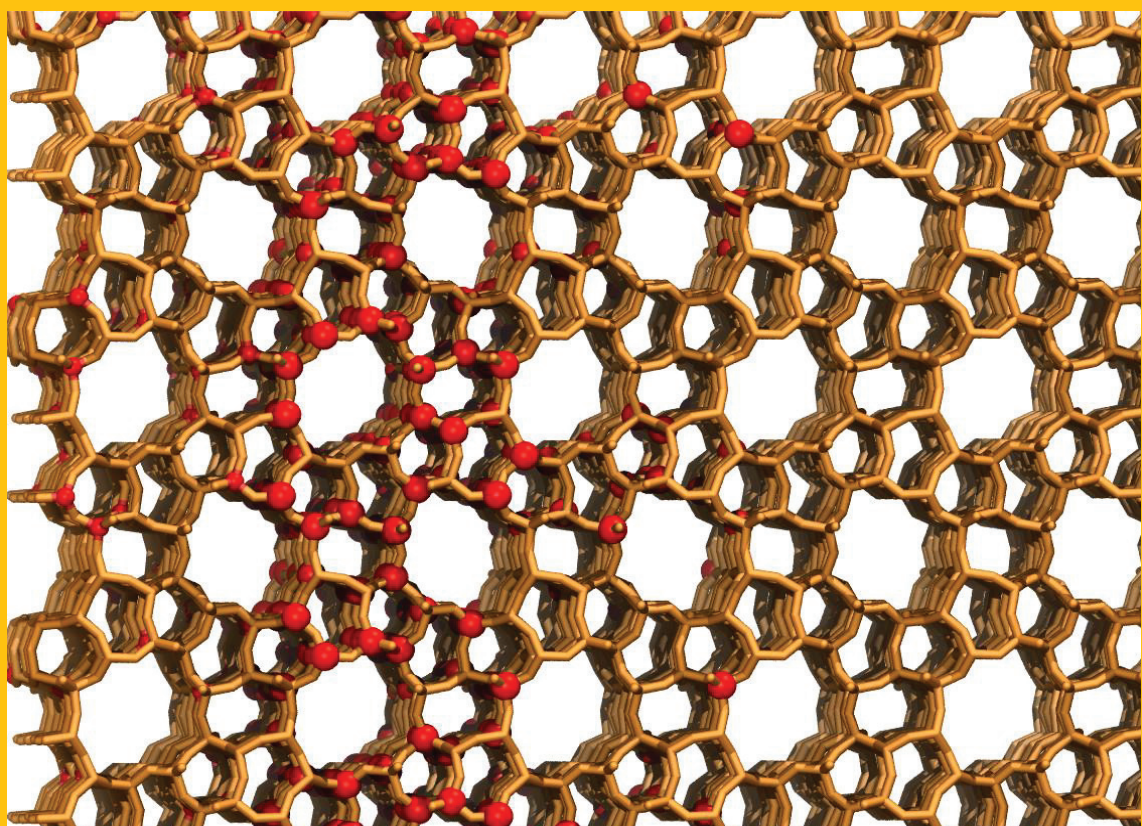
Title: Advanced Characterization of Large Zeolite Crystals
and Their Use in the Methanol-to-Hydrocarbons Process

ISBN: 978-94-9301-488-6

Printed by: Gildeprint, The Netherlands

Table of Contents

Chapter I	Introduction: Catalysis, from Alchemy to Knowledge-based Chemistry	7
Chapter II	3-D Raman Spectroscopy of Large Zeolite ZSM-5 Crystals	31
Chapter III	Coke Formation in Large Zeolite ZSM-5 Crystals during the Methanol-to-Hydrocarbons Process as Studied with Operando Optical Spectroscopy and Microscopy	55
Chapter IV	Coke Formation in Large Zeolite ZSM-5 Crystals during the Methanol-to-Hydrocarbons Process as Studied with Nano-Secondary Ion Mass Spectrometry	75
Chapter V	Coke Formation in Large Zeolite ZSM-5 Crystals during the Methanol-to-Hydrocarbons Process as Studied with Atom Probe Tomography	95
Chapter VI	Summary, Future Outlook and Nederlandse Samenvatting	115
	List of Abbreviations	131
	List of Publications and Presentations	132
	Acknowledgments	135
	About the Author	138

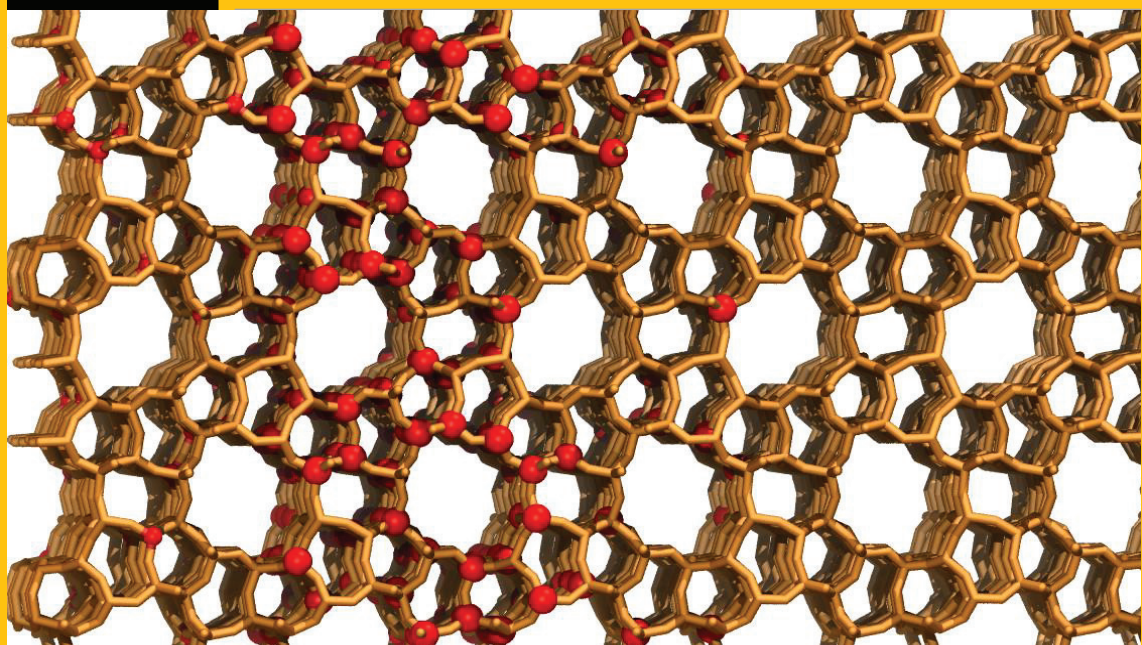


CHAPTER

I

Introduction:

Catalysis, from Alchemy to Knowledge-based Chemistry



1.1. A Brief History of Catalysis

Catalysis is a phenomenon known from very ancient times when mankind began producing alcohol through fermentation even though its theory and fundamental characteristics were not yet known as we know it today. It was the alchemical era when the fermentation process was initially formulated. The core aspect of the alchemy was to transmute the base metals into noble metals through the use of *magical stones*.^[1] Over the years, alchemy was replaced by knowledge-based chemistry and we nowadays call these previously known magical stones just catalysts.



Figure 1.1. J. J. Berzelius (1779-1848).
Reproduced from reference.^[93]

The term 'catalysis' has been introduced into the scientific literature in 1836 by Jöns Jakob Berzelius who is shown in Figure 1.1. He found analogies between the effects of sulfuric acid on ethanol to the decomposition of hydrogen peroxide and the conversion of starch into sugar.^[1] He earned the well-deserved role as one of the founding fathers of modern chemistry. The discovery of the elements of cerium, selenium and thorium, as well as the isolation of silicon, calcium, barium, strontium, tantalum and zirconium in their pure forms are some of his scientific achievements. He also originated the nowadays chemical nomenclature using the initial letter(s) of the Latin names of the elements i.e., argentum (silver), Ag and aurum (gold), Au. Berzelius also formed a code for naming compound particles as using atomic symbols written next to each other. For instance, the atoms in water would be $2\text{H}+\text{O}$, which became H_2O today.^[2] Apart from being a pioneering chemist, Berzelius was also a gifted pharmacist and a mineralogist. Being the first to recognize that silicon oxide was an acid, he has addressed the composition of stony minerals as silica-based compounds.^[3]

Nowadays, catalysis plays a fundamental role in the manufacture of the vast majority of fuels, chemicals and materials including a wide variety of plastics, used by our society. This role makes the catalysis industry a multibillion-dollar market.^[4] The role of a catalyst material is to enable chemical conversions by

lowering the activation barrier of a particular chemical reaction. As a result of this phenomenon, the efficiency and the overall selectivity of these chemical reactions can be altered. Catalysts can be sorted into three categories based on their nature, i.e., heterogeneous, homogeneous, and bio-catalysis. It is estimated that more than 85% of the chemical processes involve solid catalysts.^[5] The solid catalysts are especially used for environmental and petrochemical processes and one family of solid catalysts consist of zeolites or zeo-type materials.

This PhD Thesis focuses on the deactivation of zeolites as heterogeneous catalysts during the Methanol-to-Hydrocarbons (MTH) process; hence in what follows we will discuss this chemical conversion process, introduce the basic characteristics of zeolites and the related deactivation pathways during the MTH process.

1.2. Zeolites, from Boiling Stones to Molecular Reactors

In 1756, a Swedish mineralogist, Baron Axel F. Cronstedt, observed that some specific crystalline materials found in nature seem to ‘boil’ upon heating. Furthermore, he observed that these minerals were hydrothermally robust, so he could apply various heating-cooling cycles. He named these minerals “zeolites” based on the old Greek words of *zeo* “to boil” and *lithos* “stone”.^[6] Decades later, for the first time in 1862 a mineralogist de St. Claire Deville reported a trial of a zeolite synthesis under laboratory conditions.^[7]

In the past 50 years, the search for new chemical processes to meet the energy and materials demand, led to extensive research in zeolite-based catalysis, especially focusing on the synthesis, characterization and testing of both existing and new zeolite materials. Zeolites are crystalline microporous aluminosilicates, which forms uniformly sized pores with molecular dimensions with the general formula of $M_{x/n}^{n+}Al_xSi_{1-x}O_2$ where M is the charge-balancing non-framework cation with charge $n+$. Examples include Na^+ , Ca^{2+} , and H^+ .^[8] In the latter case a solid acid material is obtained. The uniformly sized pore system, that is in the same size range as molecules, is one of the main characteristics that makes zeolites so unique.^[9] Due to this uniform framework structure, zeolites preferentially adsorb molecules, which can fit inside and exclude the bigger molecules, which cannot fit in. In other words, zeolites act as molecular sieves. Zeolites are generally constructed from TO_4 tetrahedra (T= tetrahedral atoms, such as Al or Si). Each oxygen atom inside the zeolite framework is shared with a nearby tetrahedral atom making the framework O/T ratio equal to 2. This is illustrated in Figure 1.2. However, as the Loewenstein’s rule dictates, the distribution of Al in the center of

tetrahedra is not completely random since the local electroneutrality of the ionic structure must be preserved i.e., Pauling electrostatic valence rule.^[10]

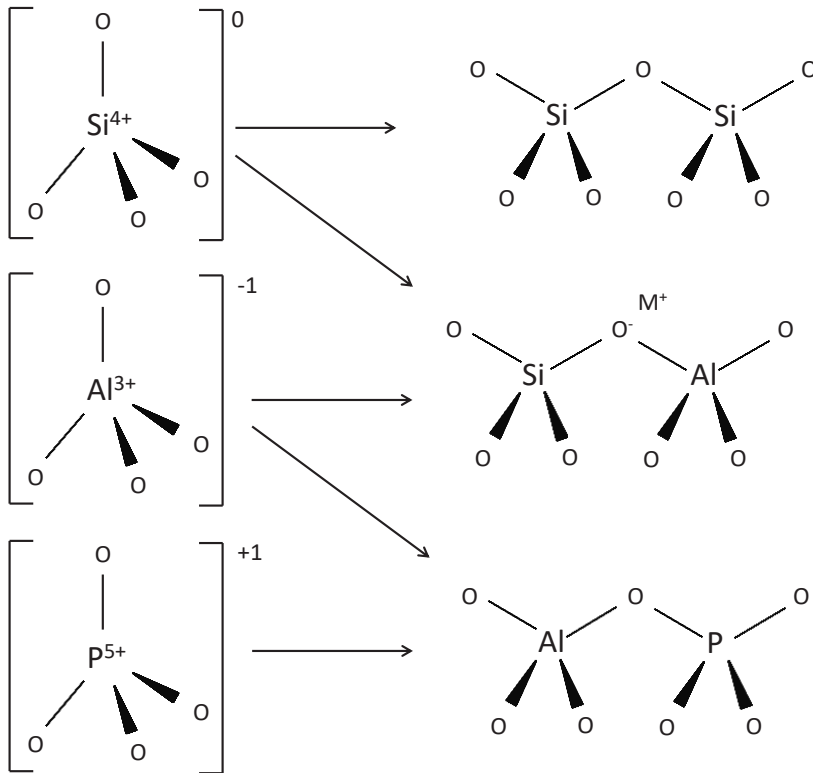


Figure 1.2. Schematics of the primary building blocks, TO₄ units, of zeolite and zeolite type materials, also known as the silicate, aluminosilicates and aluminophosphate framework structures. (Reproduced from Davis, 1991.^[9])

Therefore, Al-O-Al bonds are strictly forbidden in the zeolitic framework. The crystal chemistry of the zeolite framework contains a SiO₄ unit that is neutral instead of having a charge of -4 as each oxygen atom is sandwiched between two T atoms. When an Al atom replaces a Si atom, the net charge becomes -1 instead of 0 because of the +3 valency of Al. This can be seen in Figure 1.2. The replacement of Si⁴⁺ with Al³⁺ results in a negative charge in the zeolite framework, which is neutralized by replaceable cations (shown as M⁺ in Figure 1.2). As mentioned before, this charge balancing cation can be for example alkaline metals (e.g., Na⁺) and alkaline earth metals (e.g., Ca²⁺), as well as a proton (i.e., H⁺) that leads to the formation of *Brønsted acid sites* inside the zeolite framework.^[9,11,12]

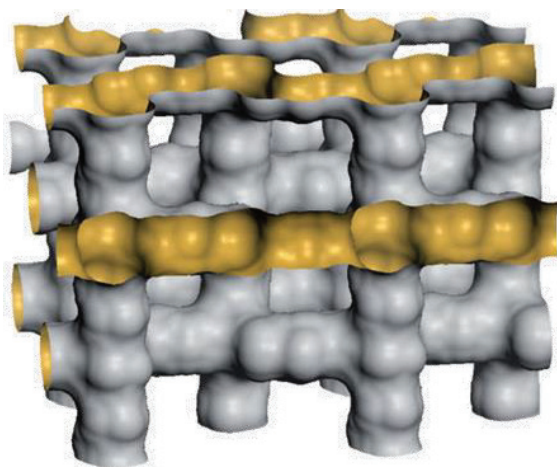


Figure 1.3. 3-D pore architecture of the MFI type zeolite framework structure, to which ZSM-5 belongs. Zeolite ZSM-5 has a 3-D channel structure and is a 10 ring zeo-type material (i.e., a medium pore zeolite). Reproduced from Olsbye et al. 2012.^[23]

Depending on their synthesis conditions and characteristics, different zeolite topologies can be modified to consist of four main pore groups: *Small pores*, 8-ring pores having 3-4.5 Å free diameter or smaller. *Medium pores*, 10-ring pores having 3.5-6 Å free diameter. *Large pores*, 12-ring pores having 6-8 Å free diameter and *Ultra large pores*, more than 12-ring. An example of a zeolite structure, namely ZSM-5, possessing the MFI framework structure, is shown in Figure 1.3. It is this material which will be investigated in detail in this PhD Thesis.

Zeolite ZSM-5 consists of two types of pore channels that are straight (5.6 x 5.3 Å) which are oriented along the [010] axis, and intersecting perpendicular sinusoidal pores (5.5 x 5.1 Å) that are in [100] orientation.^[13-16] These well-defined microporous systems offer unique molecular size and shape selectivity.^[17] A detailed description of all known zeolite framework topologies can be found in the International Zeolite Association (IZA) database.^[18]

Acid sites, molecular size, shape selectivity, thermal stability, and high surface area make zeolites and zeo-type materials very suitable for a variety of acid-catalyzed reactions in the chemical and petrochemical industries. Due to all these specifications, zeolites can be considered as molecular reactors, wherein small cages and channels of molecular dimensions, chemical reactions can be fine-tuned and their activity and selectivity steered towards a specific end product.^[19] Finally, it is important to realize that next to their application in energy industry, zeolites also find their application as laundry detergents, adsorbents, gas separation materials and as food additives for animals and plants.^[20] They are currently also explored in various catalytic processes involving natural gas, biomass and waste, thereby offering possibilities to make our society more sustainable.

1.3. Zeolite Catalysis and the Resource Shift for Chemicals Production

The chemical industry, which has been founded during the industrial revolution, currently relies heavily on fossil resources, including petroleum, coal and natural gas, which mainly consist of methane and some ethane as well as minor amounts of propane.^[21] As the global energy demand steadily increases simultaneously with the diminishing supplies of easily available fossil resources, especially petroleum, non-traditional carbon-based feedstocks are becoming more and more important to supply our world with the necessary transportation fuels, base and fine chemicals as well as advanced materials, such as plastics and coatings.^[22]

The goal in petroleum refining is the efficient conversion of a variety of crude oil fractions into valuable high-quality transportation fuel components, such as gasoline, jet fuel and diesel, next to some base chemicals, namely ethylene, propylene and butadiene.^[20] Gas-to-Liquid (GTL) technology is one of the prominent crude oil-alternative technologies to make the same transportation fuel components, and people are also trying to shift the product portfolio of GTL towards lower olefins. GTL technologies refer to the conversion of small gaseous hydrocarbons, in particular syngas (a mixture of CO and H₂), into bigger, long-chain hydrocarbons.^[23] Carbon-containing resources, such as biomass, municipal waste, and natural gas, are potential alternatives for crude oil and can be used in what is called XTL, i.e., any feed to liquid. It however always requires an initial step in which the synthesis gas is produced; a step which is often very expensive, and may lead to a wide range of chemical compositions (e.g., CO/H₂ ratios and different impurity levels). The syngas produced can be directly converted into long-chained hydrocarbons through the so-called Fischer-Tropsch Synthesis (FTS) process, and its first industrial use dates back to the pre-World War II era. The process is named after the inventors Franz Fischer and Hans Tropsch. The process served a purpose of both coal liquefaction and gas to liquids to produce high-quality gasoline for Germany where there was a lack of natural gas or petroleum reservoirs.^[19,24] FTS catalysts typically consist of Fe or Co, supported on or bound to an inorganic oxide, such as SiO₂, Al₂O₃ and TiO₂.

It took about half a century until a new major synfuel production process has been invented and finally developed. In the early 1970s, a group of researchers at Mobil discovered the formation of hydrocarbons from methanol over a synthetic ZSM-5 type zeolite, while working on unrelated projects.^[25,26] The inventors, Clarence D. Chang and Anthony J. Silvestri, explained the discovery of

this process that they named Methanol-to-Hydrocarbons (MTH) with their own words as “serendipity is universally acknowledged as a critical ingredient in technological innovation.”^[27] The strong acidic properties and regular pore structure of zeolites make them widely applicable for performing the MTH conversions and gave a clear boost to the further industrial development of this process.^[28–30] The MTH process can be tuned to make dominantly gasoline-rich products, and are then named Methanol-to-Gasoline (MTG), or to exclusively make olefin-rich products, Methanol-to-Olefins (MTO) process, or even propylene, Methanol-to-Propylene (MTP) process.^[23] Both the reaction conditions and framework type of zeolites determine the products of the MTH reaction. SAPO-34 and ZSM-5 are the generally used zeolites for the MTH process, and both can be tuned towards MTO and MTG.^[31,32]

1.4. Commercial Methanol-to-Hydrocarbons Plants

The oil crises in 1973 and 1979 lead the chemical industry to instigate a global re-evaluation on petroleum-alternatives.^[33] Methanol that could be made from any carbon source became an interesting alternative to crude oil. In 1985, the commercialization of the first MTG process took place in New Zealand. Using a fixed bed reactor, the production capacity of this MTG-produced gasoline from methanol was 14500 bpd^[23], costing 6.5 cents per liter less than the gasoline made via the earlier mentioned FTS process at that time. On the other hand, the first of its kind demonstration of a fluidized-bed reactor for the MTG process was performed in former West Germany with a production capacity of only 100 bpd.^[34] Unfortunately, due to changes in the oil prices in the following decades did not provide the economic conditions to run profitably MTG plants. While this instability in oil pricing impeded the commercial MTG processes, it also spurred the further interest in making synthetic fuels.

A new era of the production of chemicals from unconventional feedstocks emerges mainly due to the lack of cheap and generally available conventional feedstocks, more specifically crude oil. The start of this era was triggered by mainly China, that is poor in crude oil and natural gas reserves, but has the third biggest coal reserve.^[23] In order to decrease their dependence on imported crude oil, they focused on coal-based technologies to produce their chemicals. This search initiated a renewed interest in MTH processes as the coal can be utilized for methanol production. This interest in coal-based energy conversion processes has changed the global methanol industry. The increasing global importance of MTH process can be seen in Figure 1.4. China has emerged as the dominant country with respect to methanol demand and capacity. The dominance of North East Asia

in the regional methanol demand can be seen in Figure 1.5. In 2016, seven MTO units in operation existed in China. Therefore, the production of olefins became the sixth largest methanol derivative only in a few years.^[35]

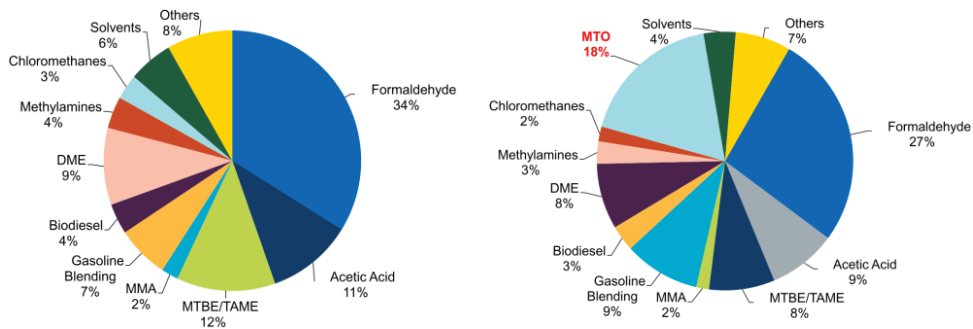


Figure 1.4. Global methanol demand by their end use in a) 2010 b) 2015. Reproduced from Alvarado, 2016.^[94]



Figure 1.5. Regional methanol demand since 2000 for various regions in the world. Reproduced from Alvarado, 2016.^[35]

1.5. Mechanistic Aspects of the Methanol-to-Hydrocarbons Process

In the past decades, extensive research has been performed to unravel the mechanisms of the related MTG, MTO and MTP processes. More than 20 mechanisms, such as oxonium ylides, carbocations, carbenes and free radicals formation, were proposed.^[23] For instance, the reaction has been described as

autocatalytic so that the presence of small amounts of chemicals, then called impurities in the methanol feed, would lead to an enhanced product formation rate until the equilibrium would be reached.^[36] Furthermore, linked to this finding, an induction period, which means the methanol conversion, increases with increasing reaction time during the initial stages of the hydrocarbon conversion reaction, was often observed.^[37] Using isotopic labeling experiments the complex reaction network of the MTO process could be evaluated. More specially, by using ^{13}C -labeled methanol as a reactant, and performing switch experiments from ^{12}C to ^{13}C methanol, Dahl and Kolboe^[22] showed that methanol had a much higher reactivity than propene and ethene on H-SAPO-34. From these findings, they proposed a mechanism called the **HydroCarbon-Pool (HCP)** mechanism and a schematic of this mechanism is given in Figure 1.6.

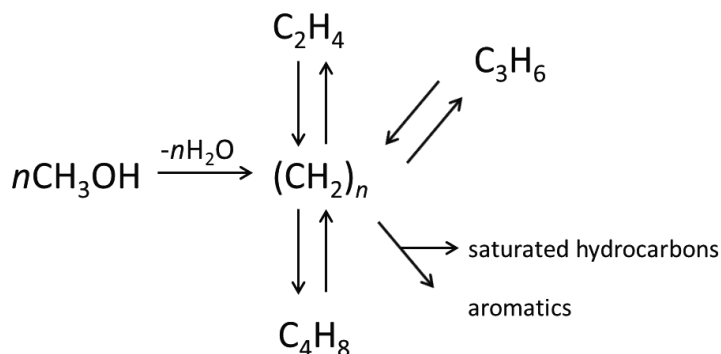


Figure 1.6. Hydrocarbon pool (HCP) mechanism taking place during the MTH process over acidic zeolites and molecular sieves, as initially proposed by Dahl and Kolboe.^[38]

However, the chemical structure of the different hydrocarbon pool species was not further specified. Further investigations by Arstad and Kolboe showed that the key components of the hydrocarbon pool species in the methanol conversion processes were methylbenzenes.^[39] In follow-up studies, Haw and co-workers used solid-state Nuclear Magnetic Resonance (NMR) to study the HCP mechanism and found that methylated cyclopentenyl cations could be alkene formation reaction centers.^[40] Bjørgen and coworkers identified that the heptamethylbenzenium cation is the key intermediate of the MTH reaction over zeolite H-beta.^[41] All these works explained that methylbenzenes in their protonated forms were the main reaction intermediates and centers from which olefins, such as propylene and ethylene, can be formed. However, it was not clarified how these olefins were exactly formed from these reaction intermediates. Further mechanistic studies focused exclusively on two hypotheses, namely the

paring mechanism and the side-chain methylation models, as illustrated in Figure 1.7.^[39,42,43]

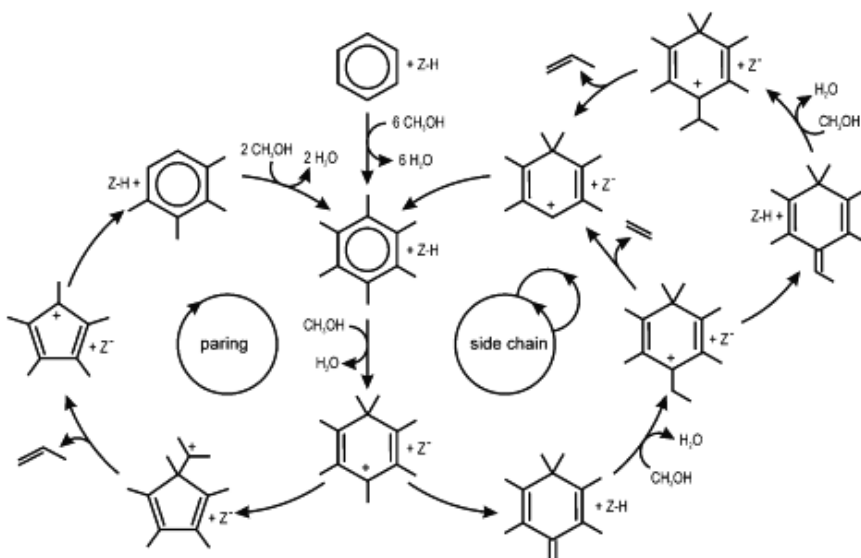


Figure 1.7. Paring and side-chain mechanisms for MTO conversion in the so-called dual cycle process for the formation of ethylene and propylene from methanol over zeolites. Reproduced from Lesthaeghe et al. 2009.^[43]

The mechanism, depicted in Figure 1.7, consists of the organic species which are trapped inside the channels and cages of the molecular sieve which are the reaction centers where methanol is continuously added in a closed catalytic cycle forming reaction (by-) products. The HCP mechanism has two cycles i.e., an “alkene cycle” where propene and higher alkenes are formed and an “aromatic cycle” where ethene and lower methylbenzenes are formed.

The HCP mechanism has been shown as a thermodynamically beneficial route for C-C bond formation. However, the initial C-C bond formation, which also affects the HCP intermediates, is still under investigation. As mentioned, impurities in the reaction feed or the catalyst contaminations once thought to be the source of the formation of the first C-C bond.^[44] However, later on instead of impurities as a trigger of the formation of first C-C bond, surface methoxy species (SMS) was considered to be an essential intermediate for the initial C-C bond formation.^[37,45–47] The interaction and further transformation of SMS and methanol (which forms methane and formaldehyde) were considered to generate the C-C bond in earlier studies.^[48,49] On the other hand, methoxymethyl carbocation (CH₃OCH₂⁺) that

forms by the interaction of SMS and DME was shown to be crucial intermediate for the initial C-C formation. [50,51]

According to some recent studies, the so-called Koch-type carbonylation mechanism is the preferred route for the first C-C bond formation in the MTH process. Lercher and coworkers have provided both theoretical and experimental evidence on the formation of the first C-C bond. They have proposed that the carbonylation of methanol and DME, which forms acetic acid and methyl acetates, are responsible for the initiation of the conversion of methanol to hydrocarbons. [52] In the same year, our group has provided the first spectroscopic evidence for the formation of (zeolite) surface bound acetate, methyl acetate as well as dimethoxymethane during the MTO process over zeolite SAPO-34 (Figure 1.8a). [53] Furthermore, a surface species-assisted “direct mechanism” was proposed as a potential candidate for the formation of the first C-C bond formation during the MTO process, as demonstrated in the most recent work from our group. [54] In this mechanism, SMS species is first formed upon the adsorption of methanol onto a Brønsted acid site (active site). Subsequently, SMS undergoes carbonylation through dehydrogenation of methanol and/or formaldehyde to form a direct C-C bond. Then surface-acetate species initiates the formation of methyl acetate which leads to the formation of HCP species and lower olefins. The schematics of these processes are shown in Figure 1.8b. [54]

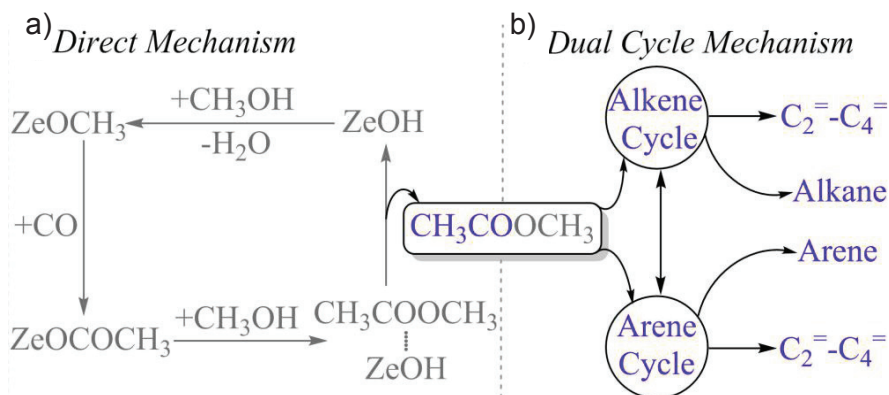


Figure 1.8. Simplified illustration of the zeolite catalyzed Methanol-to-Hydrocarbons (MTH) process mechanism. It constitutes of a) Koch carbonylation based direct mechanism b) hydrocarbon pool (HCP)/dual cycle mechanism. Zeolite is denoted as ZeOH. Blue denotation shows the selective isotope (^{13}C) labeled acetyl group of methylacetate. Reproduced from Dutta et al. 2018. [54]

As can be noticed from this short literature survey, MTH is a very complex process consisting of various networks of chemical reactions and many different hydrocarbon pool species. During the MTH process under steady-state reaction conditions, apart from the desired reaction products, there is inevitable formation and retention of heavy undesired side products forming inside the framework or on the surface of zeolites. These non-desorbent molecules are generally called 'coke' species, which are frequently considered to be the origin of catalyst deactivation. The deactivation by coke deposits is caused by pore blockage and/or poisoning of the active sites of the zeolite. Coke deposits vary from olefinic/paraffinic hydrocarbons to graphite-like material accumulation.

1.6. Zeolite ZSM-5 and its Deactivation in Methanol-to-Hydrocarbons Reactions

1.6.1. Zeolite ZSM-5 Powders

Guisnet and Magnoux correlated the coke formation with the pore structure of zeolites as well as the applied process conditions.^[55] They showed the formation of the aromatic compounds via oligomerization, alkylation, cyclization, and hydrogen transfer from the small blocked molecules inside zeolite cages. X-Ray Diffraction (XRD) and Fourier Transform IR spectroscopy (FTIR) studies have allowed researchers to relate zeolite deactivation to the formation of polycyclic aromatics.^[56] Furthermore, it was reported that the presence of sinusoidal and straight pore channels influences the adsorption of coke species with different sizes. The large aromatic species preferentially adsorb at the intersections of the sinusoidal and straight pores and orient along the straight channels to grow linearly. Due to the unfavorable tortuosity of the sinusoidal pores, larger polyaromatic compounds form within the straight channels of zeolite ZSM-5.^[57] Consistent with the aforementioned studies, Naccache and coworkers proposed that deactivation occurred when polyaromatics and pseudo-graphitic coke blocks the pores of the zeolite ZSM-5 during methylation of chlorobenzene.^[58]

Pore size plays an important role in the reaction products. Under MTH conditions, zeolites with small-pore frameworks (e.g., CHA, LEV and DDR) are selective towards the lower olefins as the larger organics cannot leave the zeolite cages. Even the small differences in the topology of zeolites with small-pore frameworks, change the product selectivity and the intermediate reaction species.^[59,60] A recent study by Goetze et al. shows the differences of the coke species formed in different small-pore zeolites under MTO conditions.^[61] When zeolites with CHA framework (zeolite SSZ-13, cage dimension: 6.7 x 10.9 Å) were

used naphthalene species filled the pores and the external coke species were formed. On the other hand, when a DDR framework (zeolite Sigma-1, cage dimension: 9.4 x 7.1 Å) was used for MTO process, 1-methylnaphthalene was found to be the main reaction species. The deactivation was caused by the complete pore filling of the zeolite, preventing the reactants and the products to reach the active sites. The deactivation of the zeolite with LEV framework (zeolite Nu-3, cage dimension: 6.5 x 7.5) was similar to zeolite Sigma-1. Complete pore filling limited the diffusion of reaction species. Coking pathways of these mentioned zeolites are shown in Figure 1.9.^[61]

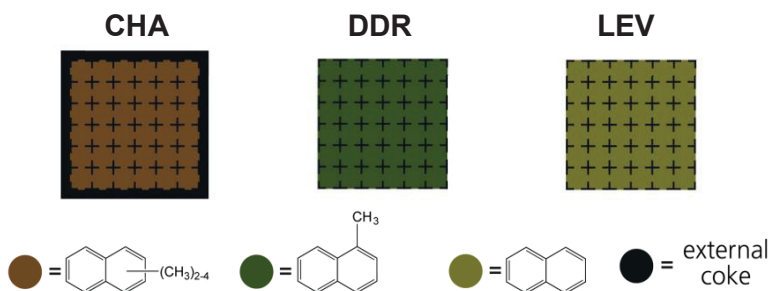


Figure 1.9. Schematic of the type of deactivation by coke species formed during MTO process at 400 °C throughout the different zeolite crystals. Reproduced from Goetze et al. 2017.^[61]

In a follow-up study, Goetze et al. investigated the pore expansion caused by the formation of the coke species using a combined UV-Vis spectroscopy and operando X-ray Diffraction (XRD) on the three zeolites with small-pore framework (i.e., CHA, DDR, LEV) mentioned above. All the zeolites used in this study have shown a lattice expansion up to 0.9% due to the formation of coke species. Methylated naphthalene and pyrene species were found to be the main cause for lattice expansion of the zeolite with CHA framework. For the DDR framework, 1-methylnaphthalene and phenalene were observed to be the main species, which caused expansion. And finally, for the LEV, the species caused lattice expansion were shown as methylated benzene and naphthalene.^[62]

Application of steaming post-treatment on the zeolites is known to alter their physicochemical properties. In fact, steaming is the most renowned method to create mesopores in zeolites. Steaming forms defect sites in the zeolite structure and enhances the aluminium and silicon mobility.^[63] Upon contact with steam, hydrolysis of Al-O-Si bonds takes place. The aluminium is expelled from the framework and creates a vacancy and partial amorphization of the framework occurs. This vacancy can be healed with amorphous and mobile silicon species and some of the vacancies grow into mesopores.^[64] The removal of aluminium

from the framework alters the Brønsted acidity of the zeolites which changes the dynamics of hydrocarbon conversion reactions. Meanwhile, the pores (especially the formed mesopores) get filled with this amorphous debris. This filling causes a decrease in the number of active sites in the zeolites. The degree of amorphization, mesopore formation and dealumination is directly dependent on the steaming temperature.^[65]

Apart from these characterization and catalytic studies, other bulk^[66–69] measurements have been performed in order to gain insights into the nature and dynamics of coke formation during zeolite catalyzed hydrocarbon conversion processes. However, none of these could provide spatially resolved information on the elemental composition of a whole zeolite crystal on the nanoscale. The correlation of zeolite framework and localized coking dynamics is still a puzzle. Understanding the mechanisms of coke formation would make the zeolite catalysts less susceptible to deactivate. The research on the coke formation and finding ways to prevent catalyst deactivation is important to improve the solid catalysts design. In order to maximize the catalytic performance of zeolitic materials, it is crucial to obtain fundamental knowledge on the correlation between the internal structure and reaction dynamics. The research on structure-property relationships in zeolites necessitates the use of zeolite model systems, e.g., the large zeolite crystals.

1.6.2. Large Zeolite ZSM-5 Crystals

Large zeolite ZSM-5 crystals are used to study the MTH process and in what follows, we summarize the main findings of the MTH studies involving the large zeolite ZSM-5 crystals that are shown in Figure 1.10a. But before, discussing the main findings, it is important to realize that these large zeolite ZSM-5 crystals possess an intergrowth structure, formed by six distinct 90° rotated neighboring pyramidal subunits that generate interfaces causing the pore arrangement to rotate. Figure 1.10b-c depicts these pyramidal sub-units.^[70–72] Such arrangement leads to internal diffusion barriers, changing the accessibility of the active sites in the zeolite crystals.^[73–77] The aforementioned pore system of zeolite ZSM-5 is shown in Figure 1.10d and can be regarded as simplified schematics of the channel system that was shown in Figure 1.3.

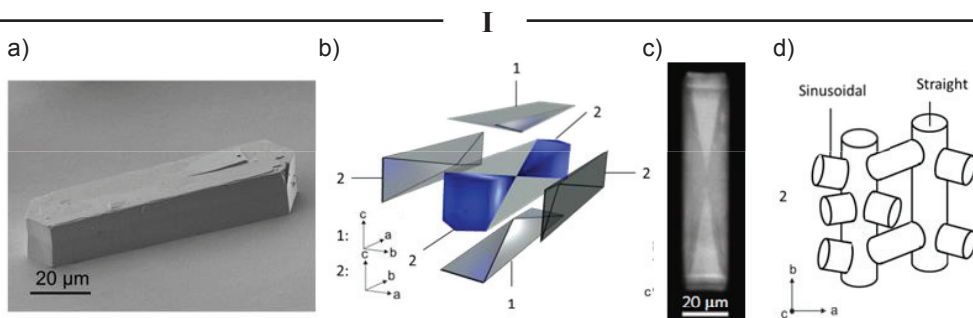


Figure 1.10. a) SEM microphotograph of the large zeolite ZSM-5 crystals with the following dimensions: $100 \times 20 \times 20 \mu\text{m}^3$. b) Large zeolite ZSM-5 crystal model that shows 6 subunits. c) Confocal fluorescence microscopy image of a large zeolite ZSM-5 crystal. The cross-section image was recorded halfway through the crystals' thickness (excitation 561 nm, detection at 575–635 nm; brighter color indicates higher intensity in greyscale). Reproduced from Karwacki et al. 2009.^[72] d) Internal pore structure of zeolite ZSM-5 with intersecting straight and sinusoidal pores.

Hofmann et al. have studied the bulk properties of these large zeolite ZSM-5 crystals in a fixed-bed reactor under MTH reaction conditions. They have compared the bulk properties of the partially deactivated zeolite ZSM-5 crystals by retained hydrocarbons analysis using hydrogen fluoride (HF) dissolution/dichloromethane extraction and a subsequent GC-MS analysis. Some compounds were observed as dominant species, which were reported as tetramethylbenzenes (TMB), pentamethylbenzene (PMB), and hexamethylbenzene (HMB) and some more heavy hydrocarbons. They compared the results of their bulk zeolite analysis with their single crystal zeolite ZSM-5 examination using Time-of-Flight Secondary Ion Mass Spectrometry (ToF-SIMS). HCP-related fragments were detected within the partially deactivated zeolite ZSM-5 crystals, very similar to the species formed with GC-MS. With this comparative approach, they concluded that large zeolite ZSM-5 crystals can be regarded as useful model catalysts to investigate the MTH reaction.^[78]

The same large zeolite ZSM-5 crystals have also been investigated with UV-Vis micro-spectroscopy and Confocal Fluorescence Microscopy (CFM). Mores et al. have shown that the hydrocarbon compounds formed in the micropore intersections of ZSM-5 contribute to both the olefin production and coke formation during the MTH reaction.^[73] Furthermore, they have reported the formation of two distinct coke types i.e., poly-methylated poly-aromatics and graphitic coke species, which form respectively within and at the outer surface of the zeolite ZSM-5 crystals during MTH processes. They observed the translucent zeolite ZSM-5 crystals have turned to yellow-brown upon exposure to the methanol. The color change of the zeolite ZSM-5 crystal can be seen in Figure 1.11a. The UV-Vis spectra taken during their study revealed the formation of two broad bands at ~415 nm and at ~550 nm, which were previously assigned to the π - π^* transitions in

methyl-substituted benzenium cations^[45,79–81] and extended conjugated aromatics^[41], respectively. The UV-Vis spectra are given in Figure 1.11b. In addition, the catalyst deactivation was attributed to the coke adsorption on Brønsted and Lewis acid sites and the blockage of pore openings at the external surface of the zeolite crystals.^[73] In a follow-up study, Mores et al. have studied the partially deactivated large ZSM-5 crystals with different excitation wavelength lasers to study the location of the different coke compounds formed during the MTH process. It was reported that as coke species grow, their light absorption at higher wavelengths become more prominent. The fluorescence appeared on zeolite ZSM-5 crystals after the MTH reaction is visible in Figure 1.11c. They have reported that the formation of fluorescent aromatic compounds that are large carbocations mainly takes place in the micropores of the large zeolite ZSM-5 crystals, while the light-absorbing, non-fluorescent graphite-like species form on the outer surface of the crystals.^[82] They reported that the coke build-up starts with the formation of the methyl-substituted benzene carbocations, which mainly forms in the intersections between the straight and the sinusoidal channels subsequently. These species evolve in size with the further addition of methanol. These polyaromatic coke species form within the straight channels of the zeolite ZSM-5 and grow in the direction of the crystal external surface where they become graphite-like structures. At that moment they cover the outer surface hindering the transport towards the inner parts of the crystal, but also avoid that, reaction products can leave the zeolite crystal. This mechanism is schematically shown in Figure 1.11d.^[83]

The influence of pore structure was also studied by using large SAPO-34 crystals and their behavior was compared with the earlier discussed large zeolite ZSM-5 crystals. Qian et al. observed that large aromatic and related coke species form within large SAPO-34 crystals during the MTH process; and these species mainly developed on the outer regions and on the external surface of the SAPO-34 crystal.^[84] On the other hand, Nordvang et al. have studied the spatiotemporal formation of the aromatic species that form during the MTH process within large ZSM-5 crystals. They have observed that the initial coke formation mainly took place in the center of the large zeolite ZSM-5 crystals and the related species diffuse towards the outer regions of the zeolite crystals.^[85]

The reaction temperature is also an important parameter that alters the reaction species. Hofmann and co-workers have reported that the local coke formation inside large zeolite ZSM-5 crystals during the MTH reaction was temperature dependent.^[78,86] Their combined approach of Time-of-Flight Secondary Ion Mass Spectrometry (ToF-SIMS) and UV-Vis micro-spectroscopy

showed that at low reaction temperatures (350 °C) coke species are formed mainly in the interior of the zeolite crystals, while at high reaction temperatures (500 °C) coke is more concentrated at the zeolite crystal outer surface.^[78]

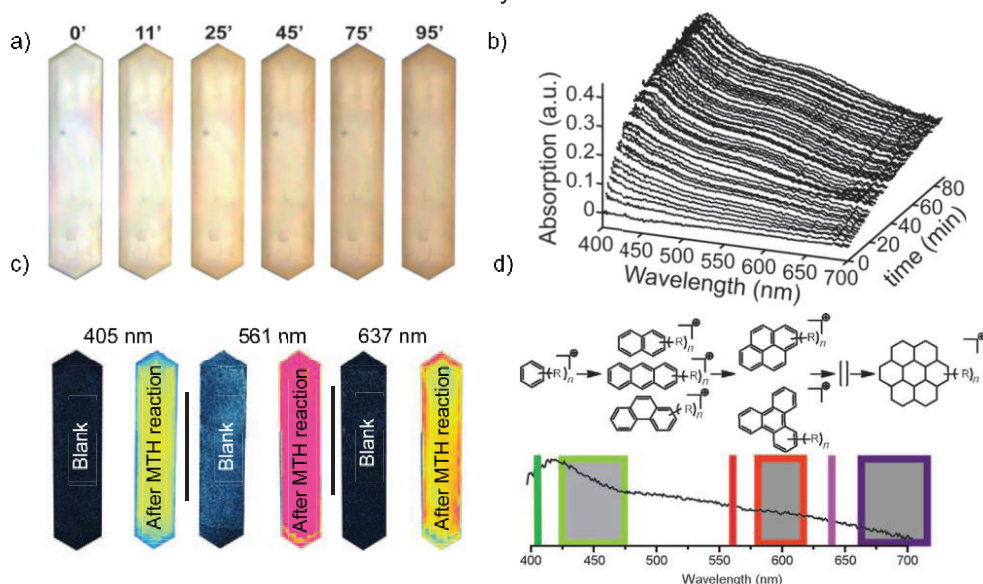


Figure 1.11. a) Selection of optical microphotographs taken during the MTO conversion for a zeolite ZSM-5 crystal at 257 °C. b) UV/Vis absorption spectra of the ZSM-5 crystal during the MTO reaction at 257 °C. Both figures (a) and (b) were reproduced from Mores et al. 2008.^[73] c) Confocal fluorescence intensity maps of the ZSM-5 crystal after 2 min of MTO conversion at 350 °C. The applied laser excitation wavelengths are 405 (425–475 nm detection region), 561 (570–620 nm detection region), and 637 nm (662–737 nm detection region). d) Proposed coke-formation process taking place during the MTO conversion over the zeolite ZSM-5 crystals. The displayed laser excitation lines 405, 561, and 637 nm indicate the distinctive UV-Vis detectable coke species revealed with each laser wavelength when applied in the confocal fluorescence experiments. Both figures (c) and (d) were reproduced from Mores et al. 2011.^[83]

Changing the physicochemical properties of the zeolites via steaming at different reaction temperatures has also been investigated in the past decade. Aramburo et al. applied a steaming post-treatment on the large zeolite ZSM-5 crystals. These authors have reported that upon steaming, the aluminium species leave the zeolite framework and that larger pores are formed. In other words, the expelled Al species cause both surface roughening and mesopore formation (5-50 nm in diameter).^[87] In their follow-up studies, Aramburo et al. have shown the large zeolite ZSM-5 crystal subunits that are acting as molecular diffusion barriers become accessible after steaming. Furthermore, they have also shown the pyramidal subunits of the large zeolite ZSM-5 crystals are less susceptible towards steaming compared to lateral subunits. The schematics of a zeolite ZSM-5 crystal

before and after steaming is shown in Figure 1.12.^[88] However, the aforementioned, amorphous debris created via steaming was reported to block the straight channels that are open in the zeolite ZSM-5 crystal tips.^[72,89] Follow-up studies were performed on large zeolite ZSM-5 crystals, which have shown that the sinusoidal channels were more susceptible towards dealumination than the straight channels.^[90] The reaction dynamics of the steamed large ZSM-5 crystals in the MTH process were also studied. Aramburo and co-workers have reported that the linear reaction products form at the expense of cyclic carbocations within steamed large zeolite ZSM-5 crystals.^[91] Furthermore, steaming was also shown to improve the MTH stability on zeolite ZSM-5 by causing a decreased poly-aromatic formation, which lowers the diffusion capabilities in the zeolites.^[92]

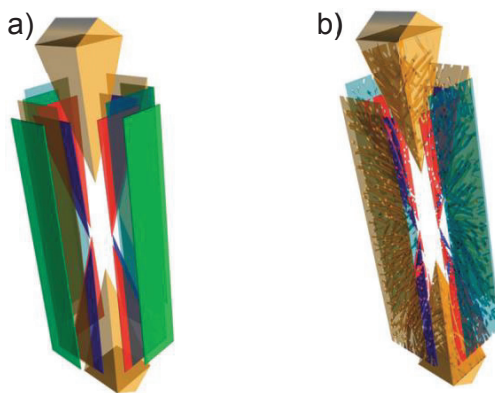


Figure 1.12. Schematic representation of the subunits and the diffusion barriers in a) non-steamed ZSM-5 and b) severely steamed ZSM-5 crystal. The crystal regions, shown in green and blue, are representing the external and internal diffusion barriers in large zeolite ZSM-5 crystals. Reproduced from Aramburo et al. 2013.^[88]

1.7. Scope and Outline of the PhD Thesis

The research work reported in this PhD Thesis involves the application of various micro- and nano-spectroscopic characterization techniques to study the chemical structure of micron-sized zeolite ZSM-5 crystals and to unravel the spatiotemporal formation of carbonaceous deposits i.e., coke or coke precursors, under operando conditions as well as under ex-situ conditions. The use of various combinations of multi-scale characterization methods allowed us to investigate these large zeolite ZSM-5 crystals as relevant model systems during and after the Methanol-to-Hydrocarbons (MTH) reaction conditions. In what follows, we outline the content of the different Chapters of this PhD Thesis.

In **Chapter 2**, confocal Raman micro-spectroscopy was used to investigate the internal structure of the large zeolite ZSM-5 crystals under investigation. More specifically, 3-D Raman spectral maps have been obtained, which provided further insights in the structural heterogeneities in the parent and in the hydrothermal treated (i.e., steamed) zeolite ZSM-5. The influence of steaming on the physicochemical properties of the zeolite ZSM-5 framework was studied. By using the different Raman spectroscopy fingerprints, Brønsted acid site distribution and the defect sites within these parent and differently steamed zeolite ZSM-5 crystals could be revealed.

In **Chapter 3** the performances of the steamed and non-steamed large zeolite ZSM-5 crystals under MTH conditions were compared. This has been done by using both operando UV-Vis micro-spectroscopy and confocal fluorescence microscopy. This complementary spectroscopic approach provided a detailed spatiotemporal evolution of the formation of coke (precursor) molecules in single zeolite ZSM-5 crystals under various reaction conditions. The fine balance between mass transport limitations inside a large zeolite crystal and the 3-D spatial distribution of both number and strength of the Brønsted acid sites and hydrocarbon pool species was investigated in depth.

Chapter 4 explores the 3-D distribution of both the framework elements constituting a zeolite ZSM-5 crystal and the carbon atoms, formed during the MTH process. This has been made possible by making use of a combination of Electron Probe Microanalysis (EPMA), Nano-Secondary Ion Mass Spectrometry (NanoSIMS) and Focused Ion Beam-Scanning Electron Microscopy (FIB-SEM). The elemental distribution inside a single zeolite ZSM-5 crystal, as well as the coke content with respect to different MTH conditions (via using ^{13}C labeled methanol), was chemically imaged. The relationship between the Brønsted acid sites (via the detection of Al) and the formation of coke species at the nanoscale are demonstrated.

Atom Probe Tomography (APT) has been used in **Chapter 5** to obtain for the first time nanoscale chemical information on both carbon and aluminum in zeolite ZSM-5 crystals, which were treated with ^{13}C labeled methanol. It was found that different zones within the zeolite ZSM-5 crystal had different Al and C distributions, but also that there exists a direct relationship between the presence of Al clusters and C clusters. We propose a set of potential molecular structures, which could be present near these Al clusters within a coked zeolite ZSM-5 crystal, which may represent the (deactivating) hydrocarbon pool species, as initially proposed by Dahl and Kolboe.

The PhD Thesis ends with **Chapter 6**, in which the main findings of the research work are summarized, including some proposals for possible future research in the field of zeolite chemistry.

References

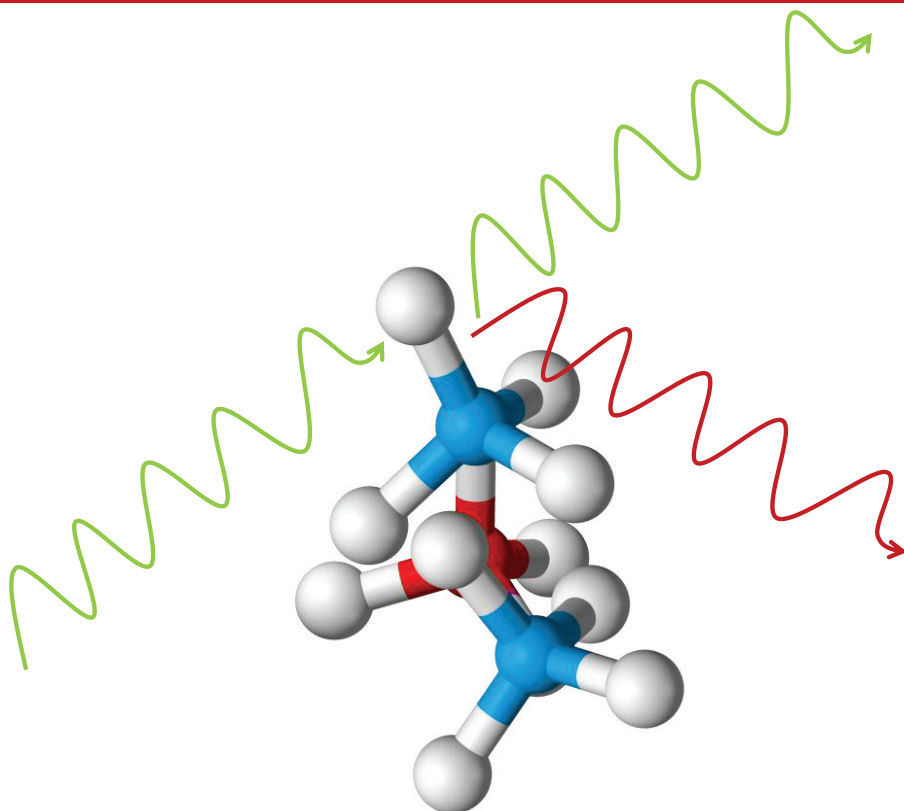
- [1] B. Lindström, L. J. Pettersson, *Cattech* **2003**, 7, 130–138.
- [2] J. Wisniak, *Chem. Educ.* **2000**, 4171, 343–350.
- [3] J. L. Marshall, *Hexag.* **2005**, 96, 72–78.
- [4] B. Yilmaz, U. Müller, *Top. Catal.* **2009**, 52, 888–895.
- [5] I. L. C. Buurmans, B. M. Weckhuysen, *Nat. Chem.* **2012**, 4, 873–886.
- [6] N. J. Turro, *Acc. Chem. Res.* **2000**, 33, 637–646.
- [7] H. de St. Claire-Deville, *Compt. Rend.* **1862**, 54, 880–889.
- [8] W. J. Mortier, *J. Catal.* **1978**, 55, 138–145.
- [9] M. E. Davis, *Ind. Eng. Chem. Res.* **1991**, 30, 1675–1683.
- [10] W. Loewenstein, *Am. Mineral.* **1954**, 39, 92–96.
- [11] C. B. Khouw, M. E. Davis, *Sel. Catal.* **1993**, 517, 206–221.
- [12] G. Busca, *Chem. Rev.* **2007**, 107, 5366–5410.
- [13] E. G. Derouane, J. G. Fripiat, *Zeolites* **1985**, 5, 165–172.
- [14] G. T. Kokotailo, S. L. Lawton, D. H. Olson, W. M. Meier, *Nature* **1978**, 272, 437–438.
- [15] C. Baerlocher, L. B. McCusker, D. H. Olson, *Sensors* **2007**, 12, 212–213.
- [16] C. Sprung, B. M. Weckhuysen, *J. Am. Chem. Soc.* **2015**, 137, 1916–1928.
- [17] J. A. Moulijn, P. W. N. M. van Leeuwen, R. A. van Santen, *Catalysis: An Integrated Approach*, Elsevier, Amsterdam, **1999**.
- [18] “<http://www.iza-structure.org/databases/>,” can be found under <http://www.iza-structure.org/databases/>, **n.d.**
- [19] A. Corma, *Chem. Rev.* **1995**, 95, 559–614.
- [20] J. D. Sherman, *Proc. Natl. Acad. Sci. U. S. A.* **1999**, 96, 3471–3478.
- [21] G. Rothenberg, *Catalysis-Concepts and Green Applications*, Wiley-VCH, Weinheim, **2008**.
- [22] I. M. Dahl, S. Kolboe, *Catal. Lett.* **1993**, 20, 329–336.
- [23] U. Olsbye, S. Svelle, M. Bjørgen, P. Beato, T. V. W. Janssens, F. Joensen, S. Bordiga, K. P. Lillerud, *Angew. Chem. Int. Ed.* **2012**, 51, 5810–5831.
- [24] M. E. Dry, *Appl. Catal. A Gen.* **2004**, 276, 1–3.
- [25] C. D. Chang, W. H. Lang, R. L. Smith, *J. Catal.* **1979**, 56, 169–173.
- [26] F. J. Keil, *Microporous Mesoporous Mater.* **1999**, 29, 49–66.
- [27] C. D. Chang, A. J. Silvestri, *This Week's Cit. Class.* **1987**, 14, 14.
- [28] T. Chmielniak, M. Sciazko, *Appl. Energy* **2003**, 74, 393–403.

- [29] B. Xu, S. Bordiga, R. Prins, J. A. van Bokhoven, *Appl. Catal. A Gen.* **2007**, *333*, 245–253.
- [30] J. Huang, Y. Jiang, V. R. R. Marthala, B. Thomas, E. Romanova, M. Hunger, *J. Phys. Chem. C* **2008**, *112*, 3811–3818.
- [31] B. M. Lok, C. A. Messina, R. L. Patton, R. T. Gajek, T. R. Cannan, E. M. Flanigen, US Patent 4440871A, **1984**.
- [32] P. G. Moses, *J. Catal.* **2015**, *328*, 19–25.
- [33] C. D. Chang, *Catal. Rev.* **1983**, *25*, 1–118.
- [34] T. F. Degnan, *J. Catal.* **2003**, *216*, 32–46.
- [35] M. Alvarado, *IHS Chem. Week* **2016**, 10–11.
- [36] Y. Ono, T. Mori, *J. Chem. Soc. Faraday Trans. 1* **1981**, *77*, 2209–2221.
- [37] W. Wang, A. Buchholz, M. Seiler, M. Hunger, *J. Am. Chem. Soc.* **2003**, *125*, 15260–15267.
- [38] I. M. Dahl, S. Kolboe, *J. Catal.* **1996**, *161*, 304–309.
- [39] B. Arstad, S. Kolboe, *Catal. Lett.* **2001**, *71*, 209–212.
- [40] J. F. Haw, *Phys. Chem. Chem. Phys.* **2002**, *4*, 5431–5441.
- [41] M. Bjørgen, U. Olsbye, S. Kolboe, *J. Catal.* **2003**, *215*, 30–44.
- [42] J. F. Haw, W. Song, D. M. Marcus, J. B. Nicholas, *Acc. Chem. Res.* **2003**, *36*, 317–326.
- [43] D. Lesthaeghe, A. Horré, M. Waroquier, G. B. Marin, V. Van Speybroeck, *Chem. Eur. J.* **2009**, *15*, 10803–10808.
- [44] W. Song, D. M. Marcus, H. Fu, J. O. Ehresmann, J. F. Haw, *J. Am. Chem. Soc.* **2002**, *124*, 3844–3845.
- [45] Y. Jiang, M. Hunger, W. Wang, *J. Am. Chem. Soc.* **2006**, *128*, 11679–11692.
- [46] Y. Jiang, W. Wang, V. R. R. Marthala, J. Huang, B. Sulikowski, M. Hunger, *J. Catal.* **2006**, *238*, 21–27.
- [47] W. Wang, M. Hunger, *Acc. Chem. Res.* **2008**, *41*, 895–904.
- [48] J. Nováková, L. Kubelková, Z. Dolejšek, *J. Mol. Catal.* **1988**, *45*, 365–372.
- [49] N. Tajima, T. Tsuneda, F. Toyama, K. Hirao, *J. Am. Chem. Soc.* **1998**, *120*, 8222–8229.
- [50] J. Li, Z. Wei, Y. Chen, B. Jing, Y. He, M. Dong, H. Jiao, X. Li, Z. Qin, J. Wang, W. Fan., *J. Catal.* **2014**, *317*, 277–283.
- [51] C. Peng, H. Wang, P. Hu, *Phys. Chem. Chem. Phys.* **2016**, *18*, 14495–14502.
- [52] Y. Liu, S. Müller, D. Berger, J. Jelic, K. Reuter, M. Tonigold, M. Sanchez-Sanchez, J. A. Lercher, *Angew. Chem. Int. Ed.* **2016**, *55*, 5723–5726.
- [53] A. D. Chowdhury, K. Houben, G. T. Whiting, M. Mokhtar, A. M. Asiri, S. A. Al-Thabaiti, S. N. Basahel, M. Baldus, B. M. Weckhuysen, *Angew. Chem. Int. Ed.* **2016**, *55*, 16072–16077.

- [54] A. Dutta Chowdhury, A. Alessandra Lucini Paioni, G. Whiting, K. Houben, M. Baldus, B. M. Weckhuysen, *Angew. Chem. Int. Ed.* **2018**, *57*, 8095–8099
- [55] P. Magnoux, M. Guisnet, S. Mignard, P. Cartraud, *J. Catal.* **1989**, *117*, 495–502.
- [56] F. Bleken, W. Skistad, K. Barbera, M. Kustova, S. Bordiga, P. Beato, K. P. Lillerud, S. Svelle, U. Olsbye, *Phys. Chem. Chem. Phys.* **2011**, *13*, 2539–2549.
- [57] R. Y. Brogaard, B. M. Weckhuysen, J. K. Nørskov, *J. Catal.* **2013**, *300*, 235–241.
- [58] C. F. Ren, G. Coudurier, C. Naccache, *Stud. Surf. Sci. Catal.* **1986**, *28*, 733–738.
- [59] M. A. Deimund, J. E. Schmidt, M. E. Davis, *Top. Catal.* **2015**, *58*, 416–423.
- [60] Y. Bhawe, M. Moliner-Marin, J. D. Lunn, Y. Liu, A. Malek, M. Davis, *ACS Catal.* **2012**, *2*, 2490–2495.
- [61] J. Goetze, F. Meirer, I. Yarulina, J. Gascon, F. Kapteijn, J. Ruiz-Martínez, B. M. Weckhuysen, *ACS Catal.* **2017**, *7*, 4033–4046.
- [62] J. Goetze, I. Yarulina, J. Gascon, F. Kapteijn, B. M. Weckhuysen, *ACS Catal.* **2018**, *8*, 2060–2070.
- [63] S. van Donk, A. H. Janssen, J. H. Bitter, K. P. de Jong, *Catal. Rev.* **2003**, *45*, 297–319.
- [64] E. G. Derouane, *Catalysts for Fine Chemical Synthesis*, John Wiley & Sons, Chichester, **2006**.
- [65] N. Salman, C. H. Rüscher, J. C. Buhl, W. Lutz, H. Toufar, M. Stöcker, *Microporous Mesoporous Mater.* **2006**, *90*, 339–346.
- [66] D. M. Bibby, N. B. Milestone, J. E. Patterson, L. P. Aldridge, *J. Catal.* **1986**, *97*, 493–502.
- [67] B. A. Sexton, A. E. Hughes, D. M. Bibby, *J. Catal.* **1988**, *109*, 126–131.
- [68] F. L. Bleken, K. Barbera, F. Bonino, U. Olsbye, K. P. Lillerud, S. Bordiga, P. Beato, T. V. W. Janssens, S. Svelle, *J. Catal.* **2013**, *307*, 62–73.
- [69] W. Song, H. Fu, J. F. Haw, *J. Phys. Chem. B* **2001**, *105*, 12839–12843.
- [70] G. D. Price, J. J. Pluth, J. V. Smith, J. M. Bennett, R. L. Patton, *J. Am. Chem. Soc.* **1982**, *104*, 5971–5977.
- [71] E. Stavitski, M. R. Drury, D. A. M. de Winter, M. H. F. Kox, B. M. Weckhuysen, *Angew. Chem. Int. Ed.* **2008**, *47*, 5637–5640.
- [72] L. Karwacki, M. H. F. Kox, D. A. M. de Winter, M. R. Drury, J. D. Meeldijk, E. Stavitski, W. Schmidt, M. Mertens, P. Cubillas, N. John, A. Chan, N. Kahn, S. R. Bare, M. Anderson, J. Kornatowski, B.M. Weckhuysen, *Nat. Mater.* **2009**, *8*, 959–965.

- [73] D. Mores, E. Stavitski, M. H. F. Kox, J. Kornatowski, U. Olsbye, B. M. Weckhuysen, *Chem. Eur. J.* **2008**, *14*, 11320–11327.
- [74] M. H. F. Kox, E. Stavitski, J. C. Groen, J. Pérez-Ramírez, F. Kapteijn, B. M. Weckhuysen, *Chem. Eur. J.* **2008**, *14*, 1718–1725.
- [75] J. Caro, M. Noack, J. Richter-Mendau, F. Marlow, D. Peterson, M. Griepentrog, J. Kornatowski, *J. Phys. Chem.* **1993**, *97*, 13685–13690.
- [76] C. Weidenthaler, R. X. Fischer, R. D. Shannon, O. Medenbach, *J. Phys. Chem.* **1994**, *98*, 12687–12694.
- [77] O. Geier, S. Vasenkov, E. Lehmann, J. Kärger, U. Schemmert, R. A. Rakoczy, J. Weitkamp, *J. Phys. Chem. B* **2001**, *105*, 10217–10222.
- [78] J. P. Hofmann, D. Mores, L. R. Aramburo, S. Teketel, M. Rohnke, J. Janek, U. Olsbye, B. M. Weckhuysen, *Chem. Eur. J.* **2013**, *19*, 8533–8542.
- [79] M. Bjørgen, S. Svelle, F. Joensen, J. Nerlov, S. Kolboe, F. Bonino, L. Palumbo, S. Bordiga, U. Olsbye, *J. Catal.* **2007**, *249*, 195–207.
- [80] W. Wang, Y. Jiang, M. Hunger, *Catal. Today* **2006**, *113*, 102–114.
- [81] M. Bjørgen, F. Bonino, S. Kolboe, K. P. Lillerud, A. Zecchina, S. Bordiga, *J. Am. Chem. Soc.* **2003**, *125*, 15863–15868.
- [82] E. Stavitski, M. H. F. Kox, B. M. Weckhuysen, *Chem. Eur. J.* **2007**, *13*, 7057–7065.
- [83] D. Mores, J. Kornatowski, U. Olsbye, B. M. Weckhuysen, *Chem. Eur. J.* **2011**, *17*, 2874–2884.
- [84] Q. Qian, J. Ruiz-Martínez, M. Mokhtar, A. M. Asiri, S. A. Al-Thabaiti, S. N. Basahel, B. M. Weckhuysen, *ChemCatChem* **2014**, *6*, 772–783.
- [85] E. C. Nordvang, E. Borodina, J. Ruiz-Martínez, R. Fehrmann, B. M. Weckhuysen, *Chem. Eur. J.* **2015**, *21*, 17324–17335.
- [86] J. P. Hofmann, M. Rohnke, B. M. Weckhuysen, *Phys. Chem. Chem. Phys.* **2014**, *16*, 5465–74.
- [87] L. R. Aramburo, L. Karwacki, P. Cubillas, S. Asahina, D. A. M. De Winter, M. R. Drury, I. L. C. Buurmans, E. Stavitski, D. Mores, M. Daturi, P. Bazin, P. Dumas, F. Thibault-Starzyk, J. A. Poost, M. W. Anderson, O. Terasaki, B. M. Weckhuysen, *Chem. Eur. J.* **2011**, *17*, 13773–13781.
- [88] L. R. Aramburo, J. Ruiz-Martínez, J. P. Hofmann, B. M. Weckhuysen, *Catal. Sci. Technol.* **2013**, *3*, 1208–1214.
- [89] Z. Ristanovic, J. P. Hofmann, M. I. Richard, T. Jiang, G. A. Chahine, T. U. Schüllli, F. Meirer, B. M. Weckhuysen, *Angew. Chem. Int. Ed.* **2016**, *55*, 7496–7500.
- [90] L. Karwacki, D. A. M. De Winter, L. R. Aramburo, M. N. Lebbink, J. A. Post, M. R. Drury, B. M. Weckhuysen, *Angew. Chem. Int. Ed.* **2011**, *50*, 1294–1298.

- [91] L. R. Aramburo, S. Wirick, P. S. Miedema, I. L. C. Buurmans, F. M. F. de Groot, B. M. Weckhuysen, *Phys. Chem. Chem. Phys.* **2012**, *14*, 6967–6973.
- [92] L. R. Aramburo, S. Teketel, S. Svelle, S. R. Bare, B. Arstad, H. W. Zandbergen, U. Olsbye, F. M. F. De Groot, B. M. Weckhuysen, *J. Catal.* **2013**, *307*, 185–193.
- [93] R. Winderlich, *J. Chem. Educ.* **1948**, *25*, 500–505.
- [94] M. Alvarado, *ASHA Lead.* **2016**, *21*, 1–34.



CHAPTER

II

3-D Raman Spectroscopy of Large Zeolite ZSM-5 Crystals

Hydrothermal treatment is a common method used to modify the physico-chemical properties of zeolites. It alters the number and type of Brønsted acid sites via dealumination and increases molecular diffusion via mesopore formation. Steaming also reduces the structural integrity of zeolite frameworks. In this Chapter, we have used Raman spectroscopy to map large zeolite ZSM-5 crystals before and after steaming. 3-D elemental maps of T-O (T= Al or Si) sites of the zeolites were obtained. We have determined the Raman active bands, which are indicative of (non-) framework Al as well as of structural integrity. Zeolite steaming caused the introduction of additional heterogeneities within the zeolite framework. Al migration and the formation of extra-framework aluminium species were detected. The experiments in this Chapter demonstrate the capability of 3-D Raman spectroscopy as a valuable tool to obtain information on the spatial distributions of elements and defects within a hierarchical material.

2.1. Introduction

In the previous Chapter, we have summarized our current understanding of how acidic zeotype materials catalyze the Methanol-to-Hydrocarbons (MTH) process. The catalytic properties of zeolites are strongly determined by their Brønsted acidity, which is determined by e.g. the Si/Al ratio of the zeolite framework. Additionally, the spatial distribution of framework and extra-framework Al atoms affects the overall reactivity of the zeolite material. Hydrothermal treatment (i.e., steaming) causes pore enlargement by modifying the zeolite microporosity, which enhances the diffusion properties of the framework. Hydrothermal treatment also leads to dealumination, which may decrease the catalytic *activity* of zeolites, depending on the steaming temperature. Indeed, elevated steaming temperature improves the accessibility of the reactants to reach the Brønsted acid sites. However, it also accelerates dealumination, which decreases the overall number of Brønsted acid sites.^[1-11] Therefore, it is required to obtain a fine balance between the number of Brønsted acid sites (i.e., the amount of active sites) and the mesopore volume formed (i.e., improving the accessibility towards the active sites) by choosing the right steaming temperature. This fine balance is clearly depending on the zeolite framework structure and its chemical composition.

It is fair to state that vibrational spectroscopies are the major characterization tools utilized in zeolite science and technology.^[12,13] In particular, infrared (IR) spectroscopy has been one of the most common spectroscopic methods used to characterize the structure and reactivity of the zeotype materials, often in combination with probe molecules, such as pyridine, ammonia, CO and NO. In comparison to IR, Raman spectroscopy is rather under-utilized in zeolite science, mainly because of the difficulty of obtaining Raman spectra with reasonable signal-to-noise (S/N) ratio. The difficulty of measuring Raman spectra of zeolites can be attributed to the often encountered broad fluorescence, which is an intrinsic property of zeotype materials.^[14] Moreover, the presence of small amounts of organic molecules can also overshadow the characteristic Raman bands of the zeotype frameworks because the Raman signal of such molecules is massively enhanced when the laser frequency matches with the frequency of their electronic transitions; a process which is better known as resonance Raman spectroscopy.^[15]

The problem of broad fluorescence could be (partially) solved by using lasers of appropriate wavelength with respect to the type of materials researched.^[13] Especially, UV lasers have helped to overcome the fluorescence problem in Raman spectroscopy of zeolites. Some active groups in this field of research include those of Can Li^[15], Prabir Dutta^[16], and Peter Stair^[17], as well as of Carlo Lamberti, Adriano Zecchina and Silvia Bordiga^[18] and we refer here to some of their research papers

for further details. For example, it has been possible to probe the dealumination extent within the MFI framework using UV-Raman spectroscopy.^[19] Similarly, temperature-dependent coke formation under hydrocarbon conversion process conditions in zeolite ZSM-5 and USY was also studied with Raman spectroscopy using a UV laser.^[15] On the other hand, high-temperature treatments under oxidative atmosphere are reported to resolve the issue of organic impurities, as it is considered that these conditions are able to remove the hydrocarbon species responsible for fluorescence.^[20]

The first assignments of vibrational bands of zeolitic frameworks were proposed by Flanigen and co-workers.^[21] They based their assignments on systematic IR investigations of silica as well as non-zeolitic minerals.^[22] Over time, researchers categorized the variety of zeolite framework topologies and composition of bulk zeolite materials.^[12,15,18,19,21,23–26] The most intense Raman bands of zeolite materials to be located between 300-600 cm^{-1} .^[12] The bands in this spectral region turned to be structure-sensitive. The most intense band in this spectral region is assigned to the vibration of an oxygen atom in a plane perpendicular to the T-O-T (T= Al, Si, P...) bonds.^[12] It was shown that the zeolites containing only even-membered rings (MR) (i.e. 4MR, 6MR, 8MR,...) have this band at $\sim 500 \text{ cm}^{-1}$. Examples include CHA and FAU. On the other hand, the presence of a 5MR lowers the main frequency of the band to 390-460 cm^{-1} . For instance, FER has an intense Raman band at $\sim 430 \text{ cm}^{-1}$, while MFI has this Raman band at $\sim 380 \text{ cm}^{-1}$.^[16]

Similarly, vibrational bands at 500–650 cm^{-1} and 300–420 cm^{-1} are due to external linkage vibrations, namely vibrations of double four-membered rings (D4R), double five-membered rings (D5R), or double six-membered rings (D6R), and pore opening vibrations, respectively.^[27] The other dominant zeolite bands are reported to occur in the ranges 650-790 cm^{-1} and 950-1250 cm^{-1} , which are assigned tentatively to the asymmetrical stretching mode of (O-T-O) and to the symmetrical stretching mode (O-T-O) of the TO_4 tetrahedra, respectively. Further band assignments for zeolite ZSM-5, as reported in various literature studies, are listed in Table 2.1. However, some of the Raman vibrational modes of zeolites are not clearly assigned due to the very similar physicochemical properties of Al and Si atoms, which are difficult to discern by vibrational spectroscopies. Therefore, some of the vibrations in the literature are stated as T-O where T refers to either Al or Si atoms.

Table 2.1 Literature survey of the different Raman band assignments of zeolite ZSM-5.

Band position (cm ⁻¹)	Vibrational mode assignments ^a	Band position (cm ⁻¹)	Vibrational mode assignments ^a
294	δ (T-O-T) of 6MR ^[27]	617	D4R ^[28]
360	δ (D6R) ^[12]	673	δ (Si-O-Al) ^[29]
380	ν_s (T-O-T) ^[16]	723	ν_s (T-O) ^[30]
408	δ (O-T-O) ^[31]	745	ν (Si-O-Al) ^[19]
438	ν (Si-O-Si) ^[32]	800	ν_s (Si-O-Si) ^[33]
454	δ (O-Si-O(Al)) ^[34]	814	$\nu_{t,as}$ (Al-O) ^[31]
470	δ (Si-O) ^[35]	832	Non-framework (Al ⁶ -O) ^[36]
548	D5R ^[37]	890	δ (O-Si-H) ^[33]
590	ν_s (Al-O-Si) ^[25]	901	ν_m (D6R) ^[31]
598	ν (Al-O-Si) ^[16]	967	δ_m, ν_m (T-O) ^[38]

^a Notation for the various motions of atoms within the normal modes is defined as follows: ν , stretching; δ , bending; s, symmetric; as, asymmetric. #MR stands for the # membered ring vibration and D#R stands for the # membered double ring vibration.

In this Chapter, we have studied large zeolite ZSM-5 crystals before and after steaming with Raman spectroscopy and microscopy. It is known from our previous characterization studies that the large zeolite ZSM-5 crystals used in this study (and that are synthesized using a TPA⁺ template) have Al enrichment on the crystal edges and the outer surface.^[39–43] In this work, parent (non-steamed) zeolite ZSM-5 crystals (denoted as P-ZSM-5) are compared with two sets of steamed ZSM-5 crystals that are either mildly treated at 500 °C (denoted as MT-ZSM-5) or severely treated crystals at 700 °C (denoted as ST-ZSM-5). By using the confocality of Raman microscopy it becomes possible to map in 3-D the spatial heterogeneities within the ZSM-5 crystals introduced by steaming. Furthermore, by a detailed comparison of the Raman spectra collected, a set of fingerprint spectra and related spectral assignments for framework and non-framework Al can be obtained.

2.2. Experimental Section

2.2.1. Materials

Large zeolite ZSM-5 crystals with a size of $\sim 100 \times 20 \times 20 \mu\text{m}^3$ (bulk Si/Al = 17) were provided by ExxonMobil (Machelen, Belgium) in their Na^+ form. The starting chemicals for the synthesis of these zeolite ZSM-5 crystals were: Ludox AS40 (40 wt% in H_2O , Sigma-Aldrich), tetrapropylammonium bromide (TPABr, Fluka, $\geq 98\%$), $\text{Al}_2(\text{SO}_4)_3 \cdot 18\text{H}_2\text{O}$ (Baker, 98%), and NH_4OH (VWR, 29%). The molar composition of the synthesis gel was 6.65 $(\text{NH}_4)_2\text{O}/0.67 \text{TPA}_2\text{O}/0.025 \text{Al}_2\text{O}_3/10 \text{SiO}_2/121 \text{H}_2\text{O}$. Their synthesis has been reported in detail elsewhere.^[8] The as-synthesized samples were first calcined at 500 °C with ramp rate of 1 °C/min for 12 h in air to remove the template in a flow oven. Subsequently, a triple ion exchange with a 10 wt% ammonium nitrate (Acros Organics, $>99\%$) solution was performed at 60 °C. After the repetition of the calcination step, the zeolite P-ZSM-5 crystals were obtained. Hydrothermal treatment (i.e., steaming) was performed in a quartz tubular oven (i.e., a Thermoline 79300 instrument) that was preheated to 120 °C. The zeolite P-ZSM-5 crystals were placed in the oven and water vapor (at 100 °C) was introduced into the tubular oven for 5 h at 500 °C to obtain mildly treated (MT-ZSM-5) and at 700 °C to obtain severely treated (ST-ZSM-5) zeolites. N_2 with a flow rate of 180 ml min^{-1} was used as the carrier gas. A follow-up calcination was performed in a static oven at 500 °C for 8 h. After the large zeolite crystals were obtained in the desired forms, they were embedded in indium filled Scanning Electron Microscope (SEM) specimen stubs for Raman spectroscopy measurements.

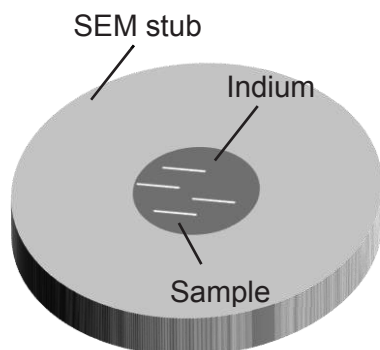


Figure 2.1 Schematic representation of a sample stage used for Raman spectroscopy measurements.

First, SEM specimen stubs (JEOL, $\text{Ø}25 \times 10 \text{ mm}$) were drilled a $\text{Ø}2 \times 1 \text{ mm}$ hole. The holes were filled up with indium beads (Sigma-Aldrich, $\geq 99.9\%$). Subsequently, the stubs filled with indium were heated to 160 °C that is the melting point of indium. After that, using a press the surface of the indium layer was flattened. Finally, the zeolite ZSM-5 crystals were sprinkled on the surface of the indium stage, as schematically shown in Figure 2.1. This approach provided surface enhancement of the Raman measurements thereby allowing to collect high-quality spectra.

2.2.2. Methods

2.2.2.1. Raman Spectroscopy

Three dimensional (3-D) Raman spectroscopy measurements were recorded making use of a high-resolution WITec alpha 300R Raman microscope using a 532 nm Nd:YAG laser with 14 mW power. Figure 2.2 outlines the measurement approach for collecting Raman spectra of zeolite ZSM-5 crystals. The Raman spectra were measured in the range of 250-1000 cm^{-1} . The spatial and axial resolution of the Raman microspectroscopy measurements were calculated from the equations given below.^[44]

$$r = 0.61 * \frac{n * \lambda}{N.A.} \quad (2.1)$$

$$\Delta = 1.5 * \frac{n * \lambda}{(N.A.)^2} \quad (2.2)$$

where,

r = spatial resolution;

Δ = axial resolution;

n = index of refraction of the medium=1 (for air);

λ = Laser wavelength; and

$N.A.$ = Numerical Aperture of the lens

The spatial resolution of the Raman microscopy measurements was $\sim 0.4 \mu\text{m}$, while the penetration depth was estimated as $\sim 1 \mu\text{m}$ with a 100x objective lens ($N.A.=0.9$). The 3-D Raman spectroscopy datasets for each zeolite ZSM-5 crystal under study consists of ten two dimensional (2-D) maps measured in $50 \times 20 \mu\text{m}^2$ areas. To limit the penetration of the laser beam into the sample, while maintaining a large enough peak intensity to overcome background noise, a hole size of $300 \mu\text{m}$ was used. A Si wafer, which has a Raman band located at 520.7 cm^{-1} , was used to calibrate the spectrometer. After scattering from the sample, the Raman light was collected in a 180° backscattering geometry, passed through a $100 \mu\text{m}$ entrance slit and diffracted using an 1800 grooves/mm grating before reaching the Charge Coupled Device (CCD) detector.

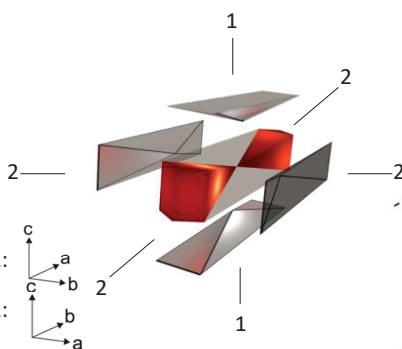
2.2.2.2. Data Processing and Analysis

For each zeolite crystal under study a 2-D Raman mapping was performed on the crystal surface (Figure 2.2d). Each subsequent Raman map was measured a micron below the previous one. Therefore half of the crystal depth ($\sim 10 \mu\text{m}$), corresponding to a quarter of a zeolite crystal could be probed. The measured zeolite layers were indicated in green in Figure 2.1e. Each 2-D Raman map was measured in the area of $50 \times 22 \text{ pixel}^2$. The collected 3-D datasets were analyzed using two different methods. A z-stack analysis was performed where we aim to elucidate the modifications caused by steaming at $500 \text{ }^\circ\text{C}$ and at $700 \text{ }^\circ\text{C}$ with respect to the measurement depth. For this reason, we have averaged the spectra from a $5 \times 5 \mu\text{m}^2$ area in the mid-region of each 2-D Raman map. The graphical representation of the analyzed zeolite volume is indicated by the red cuboid in Figure 2.2e. This analysis was performed for each measurement. The second analysis on the 3-D Raman maps of the zeolite ZSM-5 crystals was performed using Principal Component Analysis (PCA) which provides an overview of complicated multivariate data. It reduces the data dimensionality whose matrix may be too complex to study accurately. PCA analysis represents the dataset without using any *a priori* knowledge about the data characteristics.^[45–47] By choosing the number of the first N principal components covered in the variance, the data dimensionality can be reduced. In this way, no significant information would be lost but the noise could be reduced. Subsequent, k-means clustering represents the new dataset in the N -dimensional data space. K-means clustering divides M points in N dimensions into K clusters so that within-cluster sum of squares is minimized.^[48] The pixels in the new dataset are separated with respect to their Euclidian distances from the clusters centers using the centroid linkage method.^[49] With this approach, the pixels having similar Raman spectra can be separated. The original dimensions that are non-normalized contain redundant information in terms of spectral similarities i.e., peak location, peak heights and Full Width Half Maximum (FWHM). After the reduction of the original data into Principal Components (PCs), pixels having similar spectral features would be close proximity in the new data space. This process also accelerates the clustering process as the data amount would be lowered.^[46,50] The PCA and Clustering analysis was performed using an in-house-developed software package known as TXM-Wizard.^[51] Raman spectra obtained from the z-stack analysis, and PCA and Clustering, lead to Raman active bands, which were fitted with Fityk using Voigt functions. Voigt functions used were chosen for fitting as they have characteristics of both Gaussian and Lorentzian profile.^[52]

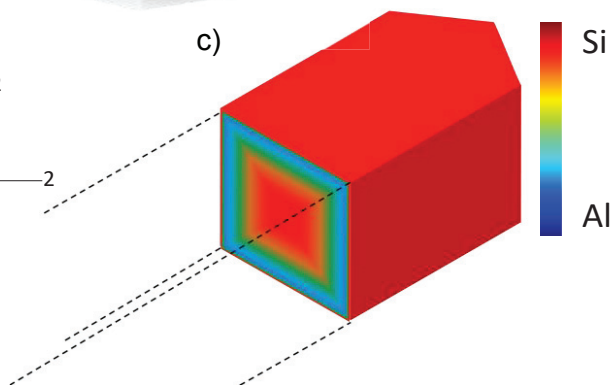
a)



b)



c)



d)



e)

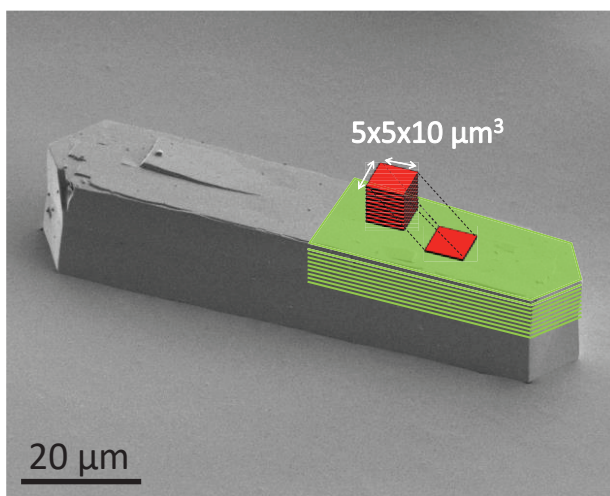


Figure 2.2. a) A photograph of the confocal Raman spectroscopy set-up used. b) Schematic diagram of the 6 sub-units of a large zeolite ZSM-5 crystal with the following dimensions: $100 \times 20 \times 20 \mu\text{m}^3$. c) Reported Si and Al distribution inside the large zeolite ZSM-5 crystals.^[39,56] d) Measurement location of the zeolite P-ZSM-5 crystal. e) Green layers indicate the location of the Raman maps of the zeolite ZSM-5 crystals, while the analyzed volume is shown by the indicated red cuboid.

2.3. Results and Discussion

Figure 2.3 shows the averaged 3-D Raman spectra of the zeolite P-ZSM-5, MT-ZSM-5 and ST-ZSM-5 crystals in the region of 250-1000 cm^{-1} . The averaged Raman spectra for each zeolite crystal measurement were fitted with Voigt functions and the resulting Raman bands were assigned based on the reported literature values (Table 2.1).

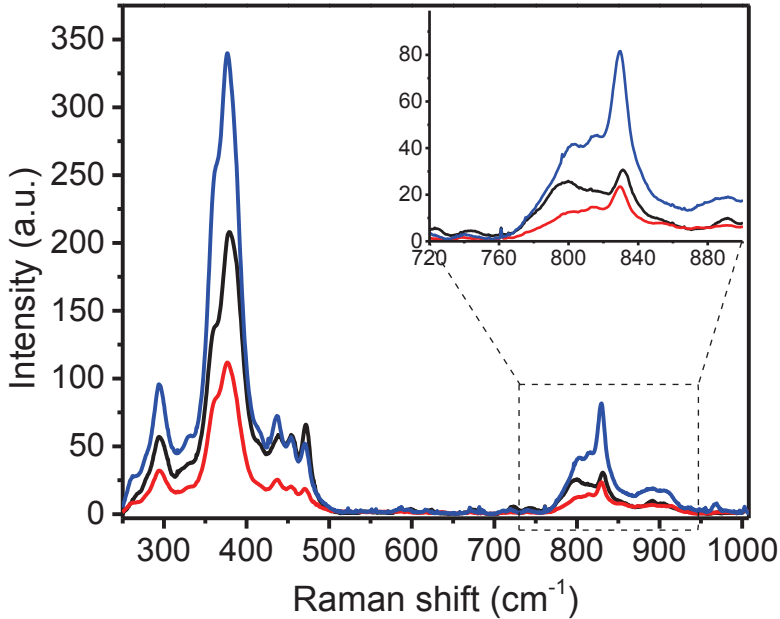


Figure 2.3. Averaged Raman spectra of the zeolite P-ZSM-5 (black), MT-ZSM-5 (red), and ST-ZSM-5 (blue) crystals. Over ten thousand spectra were averaged for each zeolite ZSM-5 crystal starting from the measured 3-D Raman map of these crystals. The spectral integration time was 7 s.

The first striking difference in the Raman spectra of the three distinct zeolite ZSM-5 crystals is the variety of spectral intensity of the clusters. The intensity of the Raman scattered radiation, I , for an isotropic sample can be expressed as, ^[53]

$$I \propto \nu^4 \cdot I_0 N \cdot \left(\frac{\partial \alpha}{\partial Q} \right)^2 \quad (2.3)$$

where

ν = Frequency of the exciting laser;

I_o = Incident laser intensity;

N = Number of scattering molecules;

α = Polarizability of the molecules; and

Q = Vibrational amplitude.

The term $(\frac{\partial\alpha}{\partial Q})^2$ describes the change in polarizability caused by molecular vibrations, so it is greater than zero. Considering a constant laser intensity and a fixed measurement geometry, the Raman band intensities are directly related to the number of scattering molecules, N . The number N is depending on the analyte concentration and the illuminated volume. Nano- and micro-scale irregularities and physical defects are known to be present in zeolite crystals. So, at a given point, the focal volume may vary due to such defect sites. Furthermore, the Raman signals generated from a specific volume is expected to be different than the signal read by the spectrometer due to scattering effects, which is also dependent on the sample geometry and physical defects in the analyte volume. In order to obtain accurate and quantitative spectral intensity, a normalization procedure was necessary to correct for overall intensity variations. Amongst many normalization methods possible, we have used the method of “normalization with respect to maximum intensity”.^[54]

Since we only used zeolite ZSM-5 crystals for this study we have selected a Raman band in the structure-sensitive region, i.e., 300-600 cm^{-1} , for normalization of the measured Raman spectra. The most prominent band detected in the spectra of both the parent and steamed zeolite ZSM-5 crystals was located at $\sim 380 \text{ cm}^{-1}$. As explained above, this band can be ascribed to the motion of oxygen atom in a plane perpendicular to T-O-T bond.^[12,24,55] This normalization method enabled an accurate comparison of the spectral intensity differences of the zeolite ZSM-5 crystals studied and the result is shown in Figure 2.4. The main spectral differences for these three zeolite crystals were observed in the region of $\sim 400\text{-}500 \text{ cm}^{-1}$ (indicated in yellow in Figure 2.4) related to different Si-O motions and in the region of $\sim 700\text{-}850 \text{ cm}^{-1}$ (indicated in orange in Figure 2.4) related different Al-O motions. These regions were chosen as the main interest for further analysis.

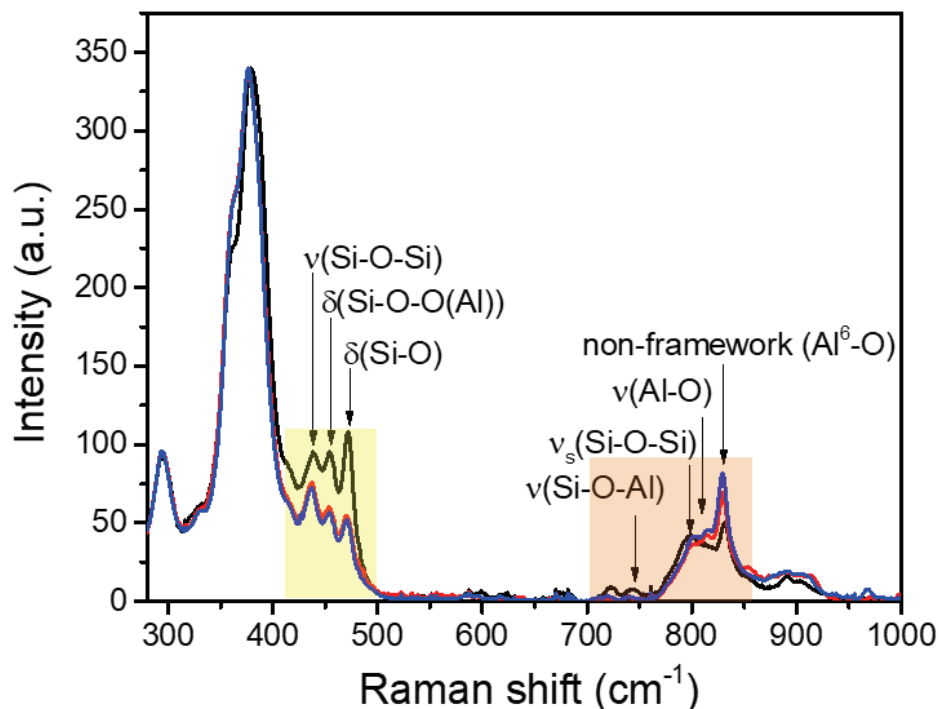


Figure 2.4. Normalized and averaged Raman spectra of zeolite P-ZSM-5 (black), MT-ZSM-5 (red) and ST-ZSM-5 (blue) crystals with indicated Raman band assignments, as summarized in Table 2.1.

2.3.1. Z-Stack Analysis

In the first part of our study, we have performed a z-stack analysis for which $5 \times 5 \mu\text{m}^2$ areas were chosen in the middle of the Raman measurement layers (Figure 2.1e). The spectra were averaged in these Raman maps measured for each zeolite ZSM-5 crystal under study. A cuboid volume taken from each zeolite ZSM-5 crystal was evaluated. The first map was measured from the crystal surface, while the last map was measured from the mid-region ($10 \mu\text{m}$ towards the crystal core starting from the outer surface). The Z stack analysis of the normalized Raman spectra of a zeolite P-ZSM-5 crystal is shown in Figure 2.5a. In addition, the zoomed-in spectral regions of interest are shown in Figure 2.5b-c. The spectra measured from the first 4 layers (the first $4 \mu\text{m}$ starting from the zeolite outer surface) were too noisy possibly due to some laser focusing issue. Therefore, these spectra (spectra number 1-4) are shown in transparent colors so that they do not obscure the rest of the Raman spectra (spectra number 5-10). The Raman band located at $\sim 440 \text{ cm}^{-1}$, ascribed to the stretching mode of the Si-O-Si bond, was observed to increase in intensity when moving towards the inner regions of the zeolite P-ZSM-5 crystal. The Raman bands at $\sim 454 \text{ cm}^{-1}$ and $\sim 470 \text{ cm}^{-1}$ (which are ascribed to bending modes of (O-Si-O(Al))^[34]

and bending mode of (Si-O)^[35] vibrations, respectively) had an opposite behavior with respect to the measurement depth. On the other hand, the spectral intensity of the Raman band located at $\sim 745\text{ cm}^{-1}$, ascribed to the Si-O-Al bridge stretching mode, has been proposed in the literature to be a direct indicator of the Brønsted moiety (i.e., the amount of Brønsted acid sites).^[19] This Raman band decreased in intensity when moving towards the deeper regions of the zeolite crystal, as illustrated in Figure 2.5c. We have fitted the Voigt functions of this Raman band and calculated the area under each function, which was taken as a direct measure for the amount of Brønsted acid sites. We have used a least-squares polynomial fit to show the relationship between the amount of Brønsted sites (by taking the spectral intensity of the Raman band at $\sim 745\text{ cm}^{-1}$) and the measurement depth in the zeolite ZSM-5 crystal and the results are summarized in Figure 2.6a. It is clear that amount of Brønsted sites (and therefore indirectly the concentration of Al atoms) is

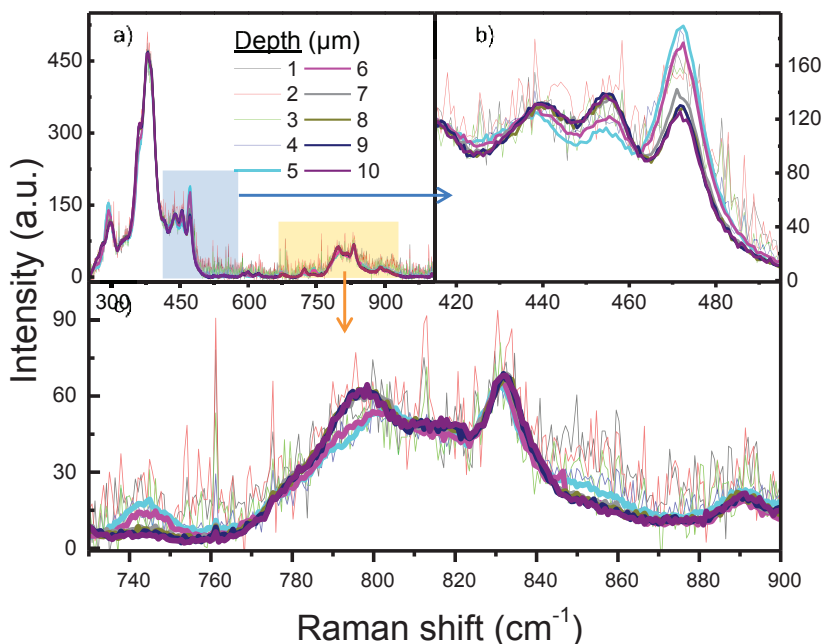


Figure 2.5. a) Normalized and averaged Raman spectra of each 2-D Raman map of a large zeolite P-ZSM-5 crystal from the chosen area for z-stack analysis. Each map is numbered according to the depth they were measured from. b) The zoomed-in spectral region of the zeolite P-ZSM-5 crystal z-stack for the b) 400-500 cm^{-1} and c) 720-900 cm^{-1} spectral regions. The zoomed-in regions in panel (b) and (c) were highlighted in blue and orange, respectively. Over ten thousand spectra were averaged for the 3-D Raman map for the zeolite P-ZSM-5 crystal. The spectral integration time was 7 s.

characterized by an exponentially decaying trend when moving from the outer zeolite crystal surface towards the inner core of the zeolite crystal. A graphical representation of this trend in zoning of Brønsted sites (and therefore Al atoms) in the large zeolite P-ZSM-5 crystals is illustrated in Figure 2.2. The Raman bands in the higher spectral energy region did not show much variation when moving from the outer surface towards the zeolite core. This observation, however, holds not for the Raman band at 800 cm^{-1} , which is known to be related to the symmetric vibrations of Si-O-Si bonds. On the other hand, the intensities of the Raman bands at $\sim 814\text{ cm}^{-1}$ and $\sim 832\text{ cm}^{-1}$ did not show any dependency with respect to the measurement depth, as shown in Figure 2.6b.

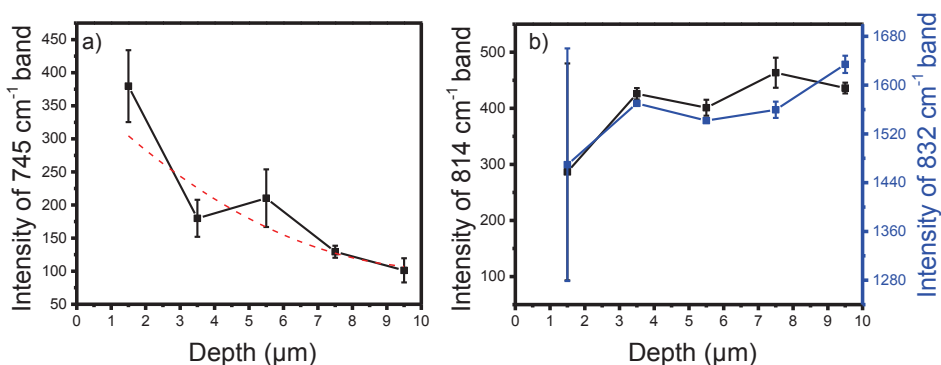


Figure 2.6. a) The relative amount of Brønsted acid sites (by determining the area under the fitted Voigt function of the 745 cm^{-1} Raman band) with respect to the zeolite P-ZSM-5 crystal depth. The red dashed curve shows the fitted polynomial function. b) The relative amount of Al-O bond (by determining the area under the fitted Voigt function of the 814 cm^{-1} and 832 cm^{-1} Raman bands) with respect to the zeolite P-ZSM-5 crystal depth.

We have applied the same z-stack analysis to a zeolite MT-ZSM-5 crystal (Figure 2.7) as well as a zeolite ST-ZSM-5 crystal (Figure 2.9). For the zeolite MT-ZSM-5 crystal measurement, the last 2-D Raman map from the depth of $10\text{ }\mu\text{m}$ did not produce any meaningful results due to an instrumental error and has therefore been excluded from our analysis. Unlike the Raman bands of the zeolite P-ZSM-5 crystal, the spectral intensity differences for the zeolite MT-ZSM-5 crystal did not show too much variation when moving from the outer crystal surface towards the inner core of the crystal. The relative spectral intensity differences for the Raman bands at $\sim 454\text{ cm}^{-1}$ and $\sim 470\text{ cm}^{-1}$ were quite different for zeolite MT-ZSM-5 as compared to zeolite P-ZSM-5. Both Raman bands were clearly more intense for P-ZSM-5 than for MT-ZSM-5. These differences can be related to the steaming procedure which decreases the zeolite structural integrity. It was also observed that

no clear depth relation of the Raman band at $\sim 440\text{ cm}^{-1}$ was detected. The presence of water at elevated temperatures, in addition to thermal effects, causes the hydrolytic splitting of the Si-O-Al-bonds.^[9] The Raman bands at $\sim 454\text{ cm}^{-1}$ and $\sim 470\text{ cm}^{-1}$ may therefore be measures for the structural integrity of zeolite ZSM-5 crystals. On the other hand, the Raman band at $\sim 745\text{ cm}^{-1}$, which indicates the presence of Brønsted acid sites, was as expectedly less intense for all the measured layers of the zeolite MT-ZSM-5 crystal as compared to the zeolite P-ZSM-5 crystal. A least-squares polynomial function was also fitted to show the relationship between the amount of Brønsted acid sites (by taking the intensity of the Raman band at $\sim 745\text{ cm}^{-1}$) and the measurement depth for the MT-ZSM-5 measurement. This is illustrated in Figure 2.8a. The decay trend of Brønsted acidity concentration was more linearized. This means that the Al concentration near the crystal surface was decreased compared to a parent zeolite ZSM-5 crystal.

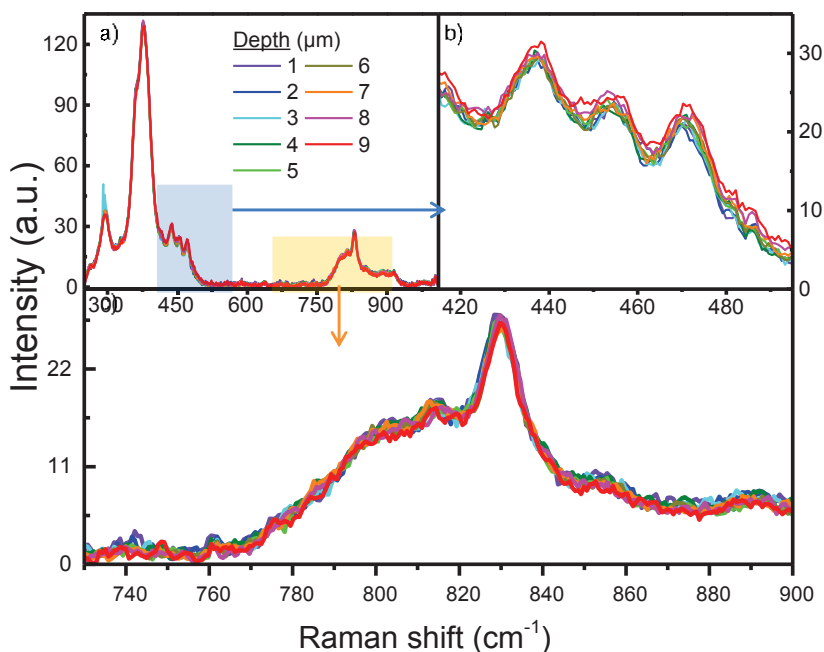


Figure 2.7. a) Normalized and averaged Raman spectra of each 2-D Raman map of a large zeolite MT-ZSM-5 crystal from the chosen area for z-stack analysis. Each map is numbered according to the depth they were collected at. b) The zoomed-in spectral region of the zeolite MT-ZSM-5 crystal Z-Stack for the b) 400-500 cm^{-1} and c) 720-900 cm^{-1} spectral regions. The zoomed-in regions in panel (b) and (c) were highlighted in blue and orange, respectively. Over ten thousand spectra were averaged for the 3-D Raman map for the zeolite MT-ZSM-5 crystal. The spectral integration time was 7 s.

The other Raman bands, which are indicative for the Al distribution at $\sim 814\text{ cm}^{-1}$ and at $\sim 832\text{ cm}^{-1}$ had different trends with respect to the crystal depth for the

zeolite MT-ZSM-5 crystal. The amount of the Al species was indeed higher below the near surface region (2-5 μm depth), where the Al-enriched region is located.^[39] This is illustrated in Figure 2.8b. The accumulation of migrated Al species due to steaming causes an increase of the Raman intensity in this spectral region.

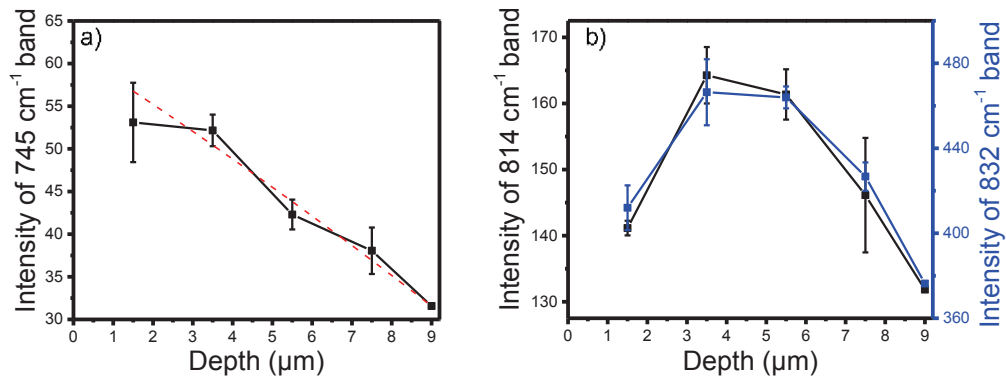


Figure 2.8. The relative amount of Brønsted acid sites (by determining the area under the fitted Voigt function of the 745 cm^{-1} Raman band) with respect to the zeolite MT-ZSM-5 crystal depth. The red dashed curve shows the fitted polynomial function. b) The relative amount of Al-O bond (by determining the area under the fitted Voigt function of the 814 cm^{-1} and 832 cm^{-1}).

The z-stack analysis was also performed on the zeolite ST-ZSM-5 crystal (Figure 2.9). All the Raman bands detected in the zeolite ST-ZSM-5 crystal had similar spectral intensities compared to the other steamed zeolite MT-ZSM-5 crystal. The relative difference between the bands at ~ 454 and $\sim 470 \text{ cm}^{-1}$ were not too pronounced for the ST-ZSM-5 crystal, as shown in Figure 2.9b. In addition, the Raman band observed at $\sim 440 \text{ cm}^{-1}$ did not show any depth variation. Considering the depth variation of the $\sim 440 \text{ cm}^{-1}$ band (that was ascribed to the stretching mode of the Si-O-Si bond^[32]) was only observed at the P-ZSM-5 crystal. Possibly, the extracted Al atoms from T sites as a result of steaming were replaced by Si atoms (and therefore healed a T-site). This process resulted in a more uniform distribution of the Si-O-Si bonds.

Raman band at $\sim 745 \text{ cm}^{-1}$, which represents the Brønsted moiety with a Voigt function, as shown in Figure 2.10a. The decay trend indicated that the Brønsted acidity dependency with depth was less pronounced. In addition, the intensity of the Raman bands at $\sim 814 \text{ cm}^{-1}$ and $\sim 832 \text{ cm}^{-1}$ further increased for the zeolite ST-ZSM-5 crystal in the regions closer to the crystal surface. The accumulation of migrated Al species in the regions close to zeolite ST-ZSM-5 crystal surface was more pronounced. Possibly, contact of water vapor under the harsh

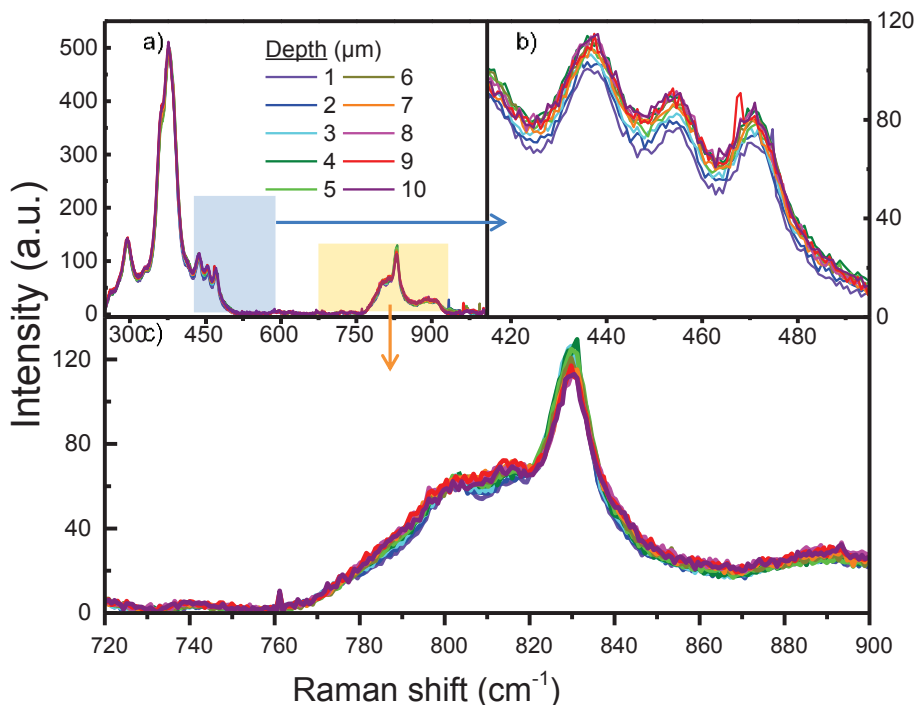


Figure 2.9. a) The normalized, averaged Raman spectra of each 2-D Raman map of a zeolite ST-ZSM-5 crystal from the chosen area for z-stack analysis. Each map is numbered according to the depth they were collected at. b) The zoomed spectral region of the zeolite ST-ZSM-5 crystal z-stack at b) 400-500 cm^{-1} c) 720-900 cm^{-1} . The zoomed regions in panel (b) and (c) were highlighted in blue and orange, respectively. Over ten thousand spectra were averaged for the zeolite ST-ZSM-5 crystal 3-D Raman map. Spectra integration time was 7 s.

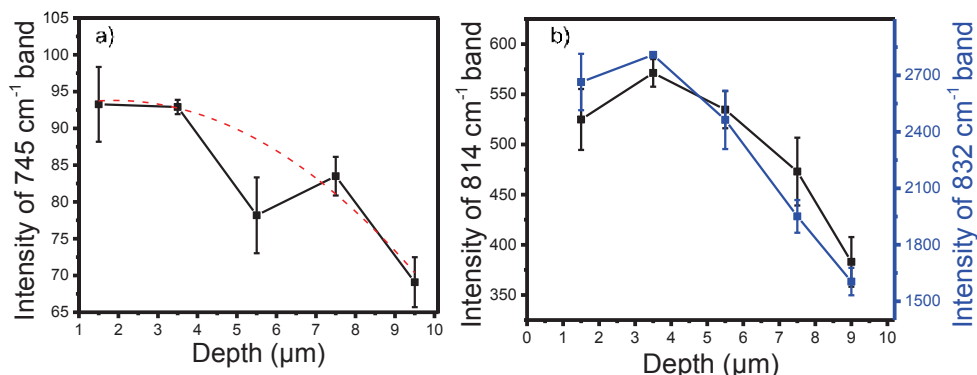


Figure 2.10. a) The relative amount of Brønsted acid sites (by determining the area under the fitted Voigt function of the 745 cm^{-1} Raman band) with respect to the zeolite ST-ZSM-5 crystal depth. The red dashed curve shows the fitted polynomial function. b) The relative amount of Al-O bond (by determining the area under the fitted Voigt function of the 814 cm^{-1} and 832 cm^{-1})

steaming conditions caused a rapid dealumination and a subsequent Al accumulation at the beginning of the Al-rich region inside the zeolite ZSM-5 crystal.

The analysis of the parent and steamed zeolite ZSM-5 crystals showed that the Raman band at $\sim 814\text{ cm}^{-1}$ (which is ascribed to symmetric Al-O vibration^[31]) had a very similar intensity behavior to the band at $\sim 832\text{ cm}^{-1}$ (which was ascribed to non-framework octahedral Al⁶-O distribution^[36]) The z-stack analysis showed this similarity was present for all the measured zeolite ZSM-5 crystals. Possibly, the band at $\sim 814\text{ cm}^{-1}$ is also indicative for the non-framework Al species.

2.3.2. Principal Component Analysis and Clustering Analysis

Principal Component Analysis (PCA) and subsequent Clustering Analysis (CA) were performed to detect the spectral variation of the recorded datasets for the zeolite P-ZSM-5, MT-ZSM-5 and ST-ZSM-5 crystals. In order to simplify the 3-D dataset that contains thousands of individual Raman spectra, the map was clustered into six regions that have distinct spectral features. The location of each respective 2-D Raman map was already shown in Figure 2.1e. The PCA and CA results for each crystal are shown in Figure 2.11. CA distinguished the background of the Raman measurements. Cluster number 2 (the blue cluster) for all the zeolites measured were identified as the background. The background cluster for each zeolite crystal disappears in the maps taken from the deeper regions of the crystal. This can be either due to increased scattering effects in the Raman spectroscopy measurements from the deeper locations or the zeolite crystal might have shifted during the measurements. Therefore, these clusters were not further analyzed.

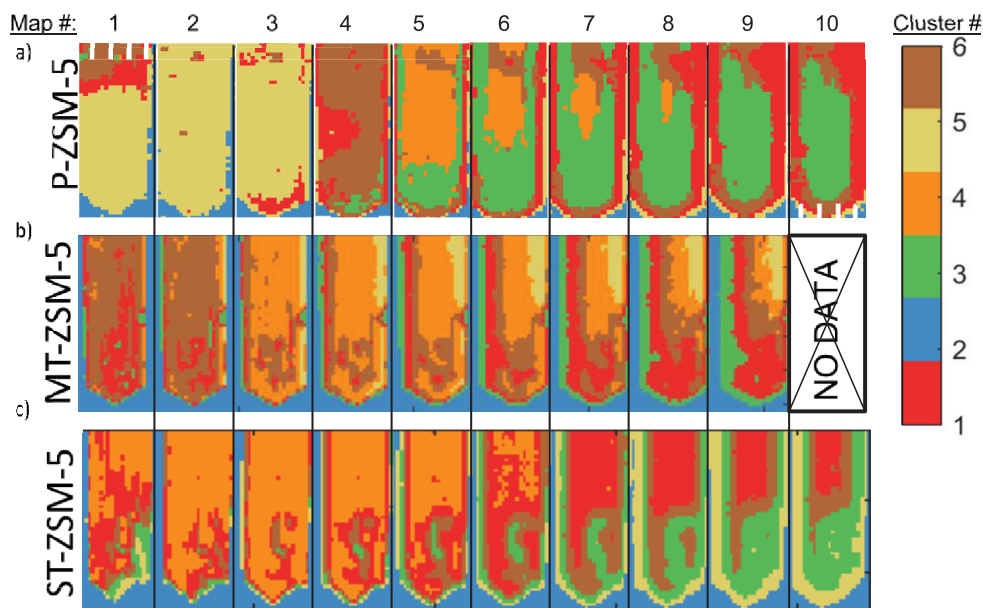


Figure 2.11. Clustering results of each individual 2-D Raman map of a zeolite a) P-ZSM-5, b) MT-ZSM-5 and c) ST-ZSM-5 crystal. Images are numbered from the zeolite surface towards the zeolite core. On the right hand side, numbering of the color-coded clusters are given.

The increasing variety of clustered regions indicate an increase in heterogeneity in the zeolite ZSM-5 crystals, specifically near the crystal surface regions, as illustrated in Figure 2.11. The spectral differences between the clusters were not as clear as the spectral differences were shown in the z-stack analysis. PCA and subsequent CA were performed on the 3-D dataset, while the z-stack analysis was performed on the measurement layers. Thus, the cluster spectra within the specific zeolite ZSM-5 crystal are very similar. The averaged Raman spectra of the clusters are shown in Figure 2.12. Similar to the z-stack analysis, the relative intensity difference of the Raman bands at $\sim 454\text{ cm}^{-1}$ and $\sim 470\text{ cm}^{-1}$ are clear in the cluster Raman spectra of the measured zeolite ZSM-5 crystals, as illustrated in Figure 2.13a-c. The intensities of both Raman bands were lower in the steamed zeolite ZSM-5 crystals compared to the P-ZSM-5 crystal. As these bands can be related to the zeolite structural integrity, the influence of the hydrothermal treatment can also be observed in the PCA and CA. In addition, PCA and CA also showed the increase of the Raman bands, which are indicative for the presence of non-framework Al species (i.e., the Raman bands at $\sim 814\text{ cm}^{-1}$ and $\sim 832\text{ cm}^{-1}$) for the steamed zeolite ZSM-5 crystals. Cluster number 3 for the zeolite MT-ZSM-5 crystal and cluster number 6 for the zeolite ST-ZSM-5 crystal had relatively higher intensity

for both Raman bands. PCA and CA also indicate that at the near edge regions in the steamed zeolite ZSM-5 crystals extra-framework aluminium is more abundant.

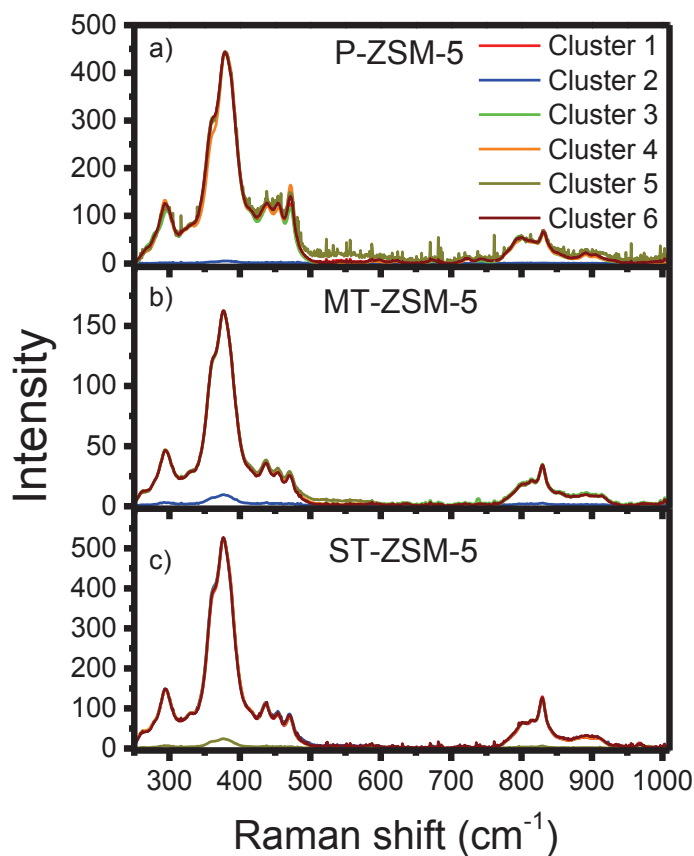


Figure 2.12. The normalized and averaged Raman spectra of the respective clusters of the zeolite a) P-ZSM-5 b) MT-ZSM-5 c) ST-ZSM-5 crystal. Over ten thousand spectra was averaged for the P-ZSM-5 crystal 3-D Raman map. Spectra integration time was 7 s.

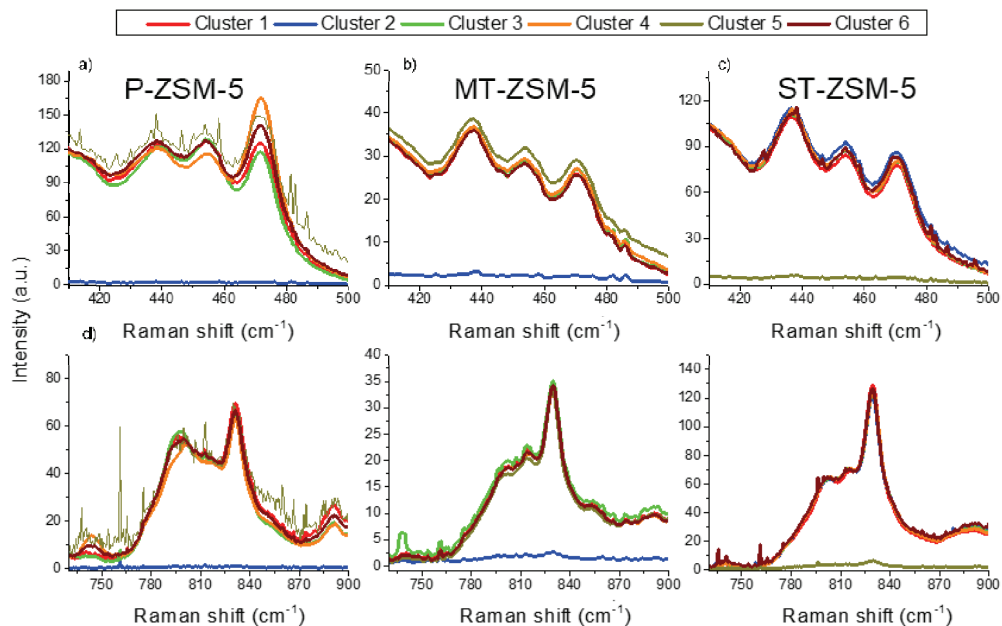


Figure 2.13. The zoomed-in normalized, mean cluster Raman spectra of the zeolite ZSM-5 crystal analyzed. 410-500 cm^{-1} spectral region of the zeolite a) P-ZSM-5, b) MT-ZSM-5 and c) ST-ZSM-5 crystal and 720-900 cm^{-1} , region of the zeolite d) P-ZSM-5, e) MT-ZSM-5 and f) ST-ZSM-5 crystal.

2.4. Conclusions

Large zeolite ZSM-5 crystals were mapped with 3-D Raman spectroscopy to identify the chemical structure of the zeolite framework. Furthermore, the structural and chemical changes occurring during a steam treatment (at 500 °C and 700 °C) on the zeolites were investigated. The Raman active vibrational modes of zeolite ZSM-5 that are related to Brønsted acid sites, defect sites, as well as structural integrity were identified. Typical Raman bands, which are linked to zeolite structure integrity, are located at $\sim 454 \text{ cm}^{-1}$, and $\sim 470 \text{ cm}^{-1}$. The intensity of these two Raman bands decreases with increasing steaming severity. In addition, another structure-related Raman band was identified at $\sim 440 \text{ cm}^{-1}$, which was found to be an indicator for the replacement of migrated Al species by Si species. Extra-framework Al species were characterized by Raman bands at $\sim 814 \text{ cm}^{-1}$ and $\sim 832 \text{ cm}^{-1}$. The amount of Brønsted acid sites, directly associated with framework Al distribution was correlated with a Raman band at $\sim 745 \text{ cm}^{-1}$.

3-D Raman spectroscopy confirmed the presence of a gradually decreasing Al distribution from outer crystal surface towards the crystal core in the large zeolite ZSM-5 crystals. The increasing heterogeneity upon steaming the zeolite

ZSM-5 crystals was observed to be more prominent in the near-surface regions than in the crystal center. This heterogeneity was followed by accessing the migration of framework Al species as well as the formation of extra-framework Al species. Upon steaming, the Al sites that are enriched in the near surface region of the zeolite crystal move towards the center of the crystal, meanwhile, the remaining framework are filled with Si atoms. Defect sites are also formed in this steaming process, mainly in the near-surface regions of the zeolite ZSM-5 crystals. This relocated extra-framework Al species accumulate inside the Al-rich region, thereby forming another Al-zoning.

2.5. Acknowledgments

Machteld Martens (ExxonMobil, Belgium) is acknowledged for providing the large zeolite ZSM-5 crystals, while Florian Meirer (Utrecht University, UU) is thanked for productive discussions and his help with the use of the TXM Wizard software. Helen King (UU) is thanked for the 3-D Raman measurements.

2.6. Contributions

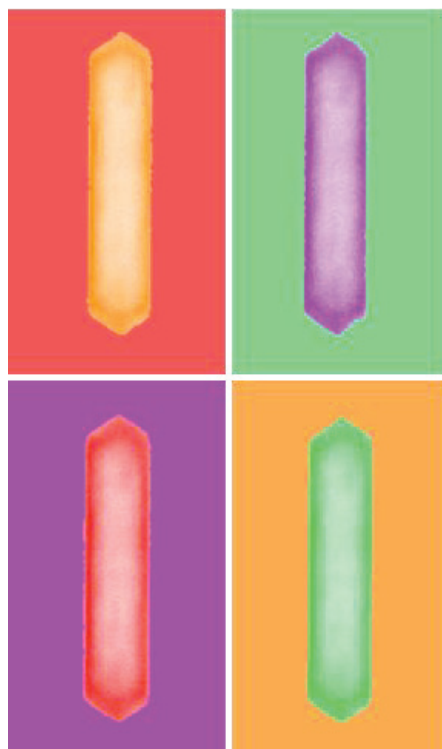
Özgün Attila conceived the idea for the experimental plan and prepared the zeolite samples. Helen King (Utrecht University, UU) has performed the 3-D Raman measurements with the guidance of Özgün Attila. The data analysis and the data interpretation were done by Özgün Attila with contributions from Florian Meirer (UU) and Bert Weckhuysen (UU). Bert Weckhuysen has made revisions and corrections to the chapter.

References

- [1] C. B. Khouw, M. E. Davis, *Sel. Catal.* **1993**, 517, 206–221.
- [2] P. Sazama, J. Dědeček, V. Gábová, B. Wichterlová, G. Spoto, S. Bordiga, *J. Catal.* **2008**, 254, 180–189.
- [3] I. M. Dahl, S. Kolboe, *Catal. Lett.* **1993**, 20, 329–336.
- [4] M. Stöcker, *Microporous Mesoporous Mater.* **1999**, 29, 3–48.
- [5] D. Lesthaeghe, A. Horré, M. Waroquier, G. B. Marin, V. van Speybroeck, *Chem. Eur. J.* **2009**, 15, 10803–10808.
- [6] M. Bjørgen, F. Joensen, K. P. Lillerud, U. Olsbye, S. Svelle, *Catal. Today* **2009**, 142, 90–97.
- [7] H. van Bekkum, E. M. Flanigen, P. A. Jacobs, J. C. Jansen, *Introduction to Zeolite Science and Practice*, Elsevier, Amsterdam, **2001**.
- [8] L. R. Aramburo, L. Karwacki, P. Cubillas, S. Asahina, D. A. M. De Winter, M. R. Drury, I. L. C. Buurmans, E. Stavitski, D. Mores, M. Daturi, P. Bazin, P. Dumas, F. Thibault-Starzyk, J. A. Poost, M. W. Anderson, O. Terasaki, B. M. Weckhuysen, *Chem. Eur. J.* **2011**, 17, 13773–13781.
- [9] Z. Ristanović, J. P. Hofmann, M. I. Richard, T. Jiang, G. A. Chahine, T. U. Schüllli, F. Meirer, B. M. Weckhuysen, *Angew. Chem. Int. Ed.* **2016**, 7496–7500.
- [10] L. Karwacki, D. A. M. De Winter, L. R. Aramburo, M. N. Lebbink, J. A. Post, M. R. Drury, B. M. Weckhuysen, *Angew. Chem. Int. Ed.* **2011**, 50, 1294–1298.
- [11] L. R. Aramburo, S. Wirick, P. S. Miedema, I. L. C. Buurmans, F. M. F. de Groot, B. M. Weckhuysen, *Phys. Chem. Chem. Phys.* **2012**, 14, 6967–6973.
- [12] P. P. Knops-Gerrits, D. E. de Vos, E. J. P. Feijen, P. A. Jacobs, *Microporous Mater.* **1997**, 8, 3–17.
- [13] S. Bordiga, C. Lamberti, F. Bonino, A. Travert, F. Thibault-Starzyk, *Chem. Soc. Rev.* **2015**, 44, 7262–7341.
- [14] Y. Yu, G. Xiong, C. Li, F. S. Xiao, *Microporous Mesoporous Mater.* **2001**, 46, 23–34.
- [15] C. Li, P. C. Stair, *Catal. Today* **1997**, 33, 353–360.
- [16] P. K. Dutta, D. C. Shieh, M. Puri, *J. Phys. Chem.* **1987**, 91, 2332–2336.
- [17] Y. T. Chua, P. C. Stair, *J. Catal.* **2003**, 213, 39–46.
- [18] M. Signorile, F. Bonino, A. Damin, S. Bordiga, *J. Phys. Chem. C* **2015**, 119, 11694–11698.
- [19] M. Signorile, F. Bonino, A. Damin, S. Bordiga, *J. Phys. Chem. C* **2016**, 120, 18088–18092.
- [20] S. Jin, Z. Feng, F. Fan, C. Li, *Catal. Lett.* **2015**, 145, 468–481.
- [21] E. M. Flanigen, H. Khatami, H. A. Szymanski, *Adv. Chem.* **1974**, 101, 201–

- 229.
- [22] R. Roy, W. B. White, *Am. Mineral.* **1964**, *49*, 1670–1687.
- [23] P. K. Dutta, J. Twu, *J. Phys. Chem.* **1991**, *95*, 2498–2501.
- [24] P. K. Dutta, B. Del Barco, *J. Phys. Chem.* **1988**, *92*, 354–357.
- [25] P. K. Dutta, M. Puri, *J. Phys. Chem.* **1987**, *91*, 4329–4333.
- [26] H. G. Karge, E. Geidel, *Vib. Spectrosc.* **2004**, *4*, 1–200.
- [27] S. Auerbach, K. Carrado, P. Dutta, *Handbook of Zeolite Science and Technology*, CRC Press, New York, **2003**.
- [28] Y. Huang, Z. Jiang, *Microporous Mater.* **1997**, *12*, 341–345.
- [29] S. Bohra, D. Kundu, M. K. Naskar, *Ceram. Int.* **2014**, *40*, 1229–1234.
- [30] K. K. Gorshunova, O. S. Travkina, M. L. Pavlov, B. I. Kutepov, R. Z. Kuvatova, N. A. Amineva, *Russ. J. Appl. Chem.* **2013**, *86*, 1805–1810.
- [31] E. Geidel, H. Böhlig, C. Peuker, W. Pilz, *Stud. Surf. Sci. Catal.* **1991**, *65*, 511–519.
- [32] R. Szostak, *Molecular Sieves Principles of Synthesis and Identification*, Springer, New York, **1989**.
- [33] M. Bärtsch, P. Bornhauser, G. Calzaferri, R. Imhof, *J. Phys. Chem.* **1994**, *98*, 2817–2831.
- [34] P. Bornhauser, G. Calzaferri, *J. Phys. Chem.* **1996**, *100*, 2035–2044.
- [35] S. R. Stojkovic, B. Adnadjevic, *Zeolites* **1988**, *8*, 523–525.
- [36] S. P. Zhdanov, T. I. Titova, L. S. Kosheleva, W. Lutz, *Pure App. Chem* **1989**, *61*, 1977–1980.
- [37] G. Wengui, L. Juan, L. Hongyuan, Y. Muliang, H. Jiehan, *IR Study of Framework Vibrations and Surface Properties of High Silica Zeolites*, Elsevier, Amsterdam, **1985**.
- [38] R. Belaabed, S. Elabed, A. Addaou, A. Laajab, M. A. Rodríguez, A. Lahsini, *Bol. la Soc. Esp. Ceram. y Vidr.* **2016**, *55*, 152–158.
- [39] R. von Ballmoos, W. M. Meier, *Nature* **1981**, *289*, 782–783.
- [40] E. G. Derouane, S. Determmerie, Z. Gabelica, N. Blom, *Appl. Catal.* **1981**, *1*, 201–224.
- [41] R. Althoff, B. Schulz-Dobrick, F. Schüth, K. Unger, *Microporous Mater.* **1993**, *1*, 207–218.
- [42] J. B. Nagy, P. Bodart, H. Collette, J. El Hage-Al Asswad, Z. Gabelica, R. Aiello, A. Nastro, C. Pellegrino, *Zeolites* **1988**, *8*, 209–220.
- [43] G. Debras, A. Gourgue, J. B. Nagy, G. De Clippeleir, *Zeolites* **1985**, *5*, 369–376.
- [44] R. H. Webb, *Reports Prog. Phys.* **1999**, *59*, 427–471.
- [45] Jolliffe, *Principal Component Analysis*, Springer, New York, **2002**.
- [46] R. Bro, A. K. Smilde, *Anal. Methods* **2014**, *6*, 2812–2831.
- [47] R. A. Johnson, D. W. Wichern, *Applied Multivariate Statistical Analysis*,

- Prentice-Hall, Inc., Upper Saddle River, **2008**.
- [48] J. A. Hartigan, M. A. Wong, *Appl. Stat.* **1979**, *28*, 100–108.
- [49] S. L. Bieber, D. V Smith, *Chem. Senses* **1986**, *11*, 19–47.
- [50] S. Wold, K. Esbensen, P. Geladi, *Chemom. Intell. Lab. Syst.* **1987**, *2*, 37–52.
- [51] Y. Liu, F. Meirer, P. A. Williams, J. Wang, J. C. Andrews, P. Pianetta, *J. Synchrotron Radiat.* **2012**, *19*, 281–287.
- [52] T. Vácz, *Appl. Spectrosc.* **2014**, *68*, 1274–1278.
- [53] P. Larkin, *IR and Raman Spectroscopy: Principles and Spectral Interpretation*, Elsevier, Oxford, **2011**.
- [54] A. Zoubir, *Raman Imaging*, Springer, Berlin, **2012**.
- [55] P. K. Dutta, K. M. Rao, J. Y. Park, *J. Phys. Chem.* **1991**, *95*, 6654–6656.
- [56] L. Karwacki, M. H. F. Kox, D. A. M. de Winter, M. R. Drury, J. D. Meeldijk, E. Stavitski, W. Schmidt, M. Mertens, P. Cubillas, N. John, A. Chan, N. Kahn, S. R. Bare, M. Anderson, J. Kornatowski, B. M. Weckhuysen, *Nat. Mater.* **2009**, *8*, 959–965.



CHAPTER III

Coke Formation in Large Zeolite ZSM-5 Crystals during the Methanol-to-Hydrocarbons Process as Studied with Operando UV-Vis and Fluorescence Micro-Spectroscopy

The effect of steaming on the formation of coke (precursor) species within large zeolite ZSM-5 zeolite crystals during the Methanol-to-Hydrocarbons (MTH) reaction was studied with a combination of operando UV-Vis micro-spectroscopy and confocal fluorescence microscopy. Formation of optically active hydrocarbon species was influenced by the zeolite porosity and Brønsted acidity, which can be altered by changing the steaming pre-treatment. Polarization-dependent fluorescence microscopy measurements with multiple excitation wavelength lasers revealed the locations where the different hydrocarbon species are formed within a single zeolite crystal. The spatiotemporal formation of coke (precursor) species was estimated by using the measured fluorescence intensity, leading to further insights in the effect of steaming on the deactivation process of zeolite ZSM-5 crystals during the MTH process.

3.1. Introduction

Large zeolite ZSM-5 crystals can be regarded as suitable model systems for studying the Methanol-to-Hydrocarbons (MTH) process due to their high crystallinity and well-defined confined spaces that allow shape selectivity. Furthermore, these crystals allow to use a wide variety of spectroscopy and microscopy tools, which can assess both the organic and inorganic part of a catalytic process within a solid catalyst. It is generally accepted that the MTH process depends on the strength and local structure of Brønsted acid sites, which are affected by the zeolite structure as well as the local Si/Al ratio.^[1-7] In addition, the existence of defect sites in zeolite frameworks has an influence on their MTH performance.^[8,9]

In this Chapter, we have investigated both parent large zeolite ZSM-5 crystals (denoted as P-ZSM-5) and steamed zeolite ZSM-5 large crystals, which have been treated at 500 °C (denoted as MT-ZSM-5) and at 700 °C (denoted as ST-ZSM-5). This set of three distinct materials have been evaluated under MTH reaction conditions using operando UV-Vis micro-spectroscopy coupled with Mass Spectrometry (MS) (Figure 3.1a-b) as well as confocal fluorescence microscopy (CFM) (Figure 3.1c-d). The goal was to visualize the formation of coke (precursor) species within these zeolite ZSM-5 crystals during the MTH process and assess the effect of steaming on the evolution of the amount of these hydrocarbon species as a function of reaction time.

3.2. Experimental Section

3.2.1. Materials and Reaction

Large zeolite ZSM-5 crystals with an average size of 100 x 20 x 20 μm^3 (bulk Si/Al = 17) were provided by Exxon-Mobil (Machelen, Belgium) in their sodium form. The starting chemicals for the synthesis of these zeolite ZSM-5 crystals were: Ludox AS40 (Sigma-Aldrich, 40 wt% in H_2O), tetrapropylammonium bromide (TPABr, Fluka, $\geq 98\%$), $\text{Al}_2(\text{SO}_4)_3 \cdot 18\text{H}_2\text{O}$ (Baker, 98%), and NH_4OH (VWR, 29%). The molar composition of the synthesis gel was 6.65 $(\text{NH}_4)_2\text{O}/0.67 \text{TPA}_2\text{O}/0.025 \text{Al}_2\text{O}_3/10 \text{SiO}_2/121 \text{H}_2\text{O}$. Their synthesis procedure has been reported elsewhere.^[10] The as-synthesized samples were first calcined at 500 °C for 12 h in air to remove the template in a flow oven. Subsequently, a triple ion exchange with a 10 wt% ammonium nitrate (Acros Organics, 99+%) solution at 60 °C was performed. After the repetition of the calcination step, the parent zeolite ZSM-5 (further denoted as P-ZSM-5) crystals were obtained. Hydrothermal treatment (steaming) was performed

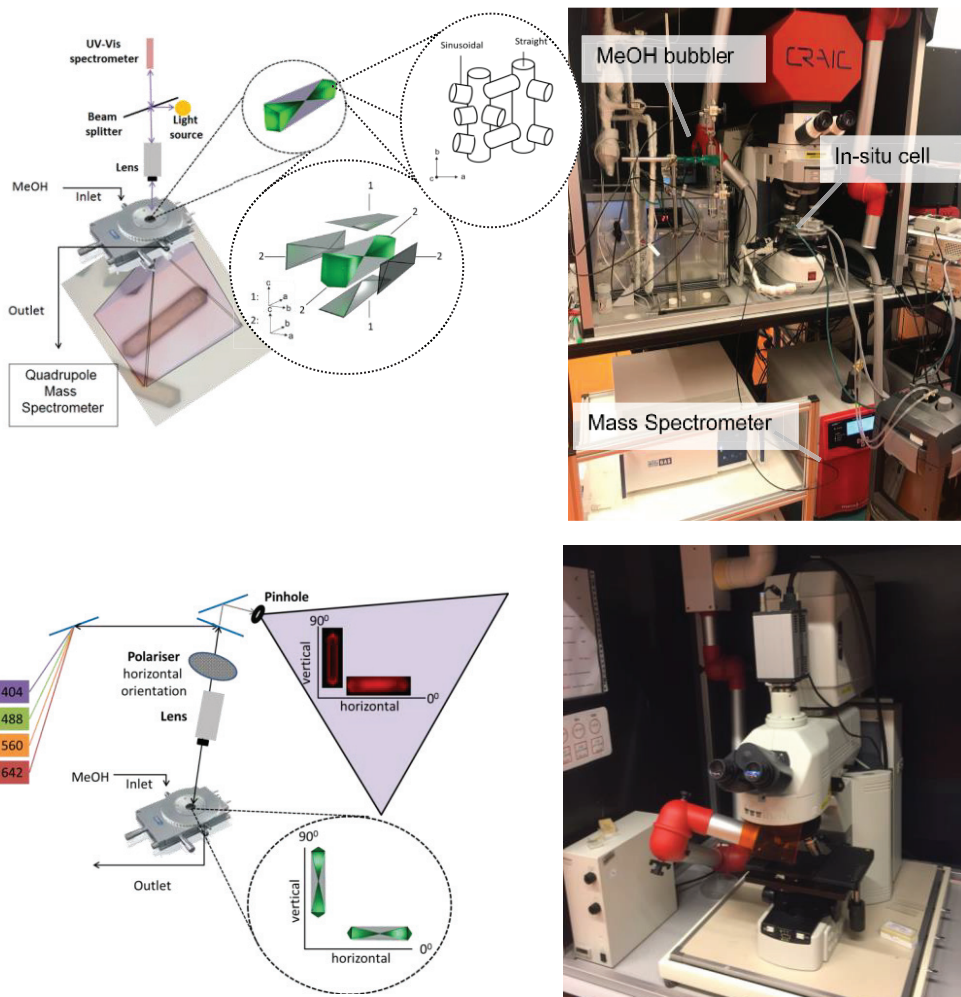


Figure 3.1. a) Schematic representation of the operando UV-Vis micro-spectroscopy set-up. Inset: exploded view of the large zeolite ZSM-5 crystal. b) Photograph of the operando UV-Vis micro-spectroscopy set-up. The in-situ reaction cell sitting on the table of the UV-Vis microscope. Light passes through the transparent window of the cell and allows studying the specimen under reaction conditions. c) Schematics of the in-situ confocal fluorescence microscopy set-up. Roof positions of the crystals at 0° and 90° orientation investigated for their fluorescence upon laser excitation of 405, 488, 560 and 642 nm. d) Photograph of the confocal fluorescence microscopy set-up. The microscope is placed on the anti-vibration table in order to avoid interferences during imaging.

in a quartz tubular oven (Thermoline 79300) that was preheated to 120 °C. The zeolite P-ZSM-5 crystals were placed in the oven and water vapor (at 100 °C) was introduced into the tubular oven for 5 h at 500 °C to obtain mildly treated (further denoted as MT-ZSM-5) and at 700 °C to obtain severely treated (further denoted as ST-ZSM-5) crystals. A nitrogen flow (180 ml.min⁻¹) was used as carrier gas. A follow-up calcination at 500 °C for 8 h in a static oven was performed. After the calcination procedure, no traces of aromatics were observed before MTH reactions.

Methanol-to-Hydrocarbons (MTH) conversion was performed in an in-situ reaction cell equipped with a quartz window for light microscopy (THMS 600, Linkam Scientific Instruments) with a temperature controller (Linkam TMS94). The large zeolite ZSM-5 crystals were placed on a quartz plate in the in-situ reaction cell and subsequently heated to 120 °C (5 °C.min⁻¹ for 30 min) under O₂ flow of 20 ml.min⁻¹ as the initial heating step before reaction. Then, the temperature was increased to 550 °C (5 °C.min⁻¹) for 60 min. This method removed all possible organics from the zeolite crystals. Upon the completion of the calcination process, the temperature was decreased to the reaction temperature of 350 °C under 20 ml.min⁻¹ N₂ flow and methanol was introduced into the cell. The maximum reaction duration was chosen as 90 min to ensure the zeolite crystals had sufficient occluded coke deposits for analysis but were not yet deactivated, as demonstrated in previous work from our group using this material.^[11]

3.2.2. Methods

The UV-Vis diffuse reflectance micro-spectroscopy measurements were performed with a CRAIC 20/30 PV™ UV-Vis micro-spectrophotometer using a 36x objective. A 75 W Xenon lamp was used for illumination. The large zeolite ZSM-5 crystals were placed in an in-situ reaction cell. Spectral UV-Vis diffuse reflectance measurements were done in the mid-crystal region of the top surface (roof position) of the zeolite ZSM-5 crystal under MTH conditions. The spectra were fitted with Gaussian functions in order to detect the formation of the reaction species. The on-line gas phase product analyses were performed by a Pfeiffer OmniStar GSD 320 O3 (1-300 amu) mass spectrometer (MS), which was directly connected to the outlet of the Linkam cell (Figure 3.1a). Effluent gases from Linkam cells were measured in the range of 1-150 amu during time on stream. The mass spectrometry database from the National Institute of Standards and Technology (NIST) was consulted for referencing purposes. Confocal fluorescence microscopy studies were performed with a Nikon Eclipse LV150 upright microscope with a 50x0.55 NA dry objective lens. The confocal fluorescence microscopy images were collected with the use of a Nikon-Eclipse C1 head connected to the four laser light sources of 405 nm, 488 nm,

561 nm and 642 nm. The zeolite ZSM-5 crystals were loaded into a Linkam FTIR 600 in-situ cell equipped with a temperature controller (Linkam TMS94). The top plane of the zeolite crystals was excited using the respective laser lines under MTH conditions, as illustrated in Figure 3.1c-d.

3.3. Results and Discussion

3.3.1. Operando UV-Vis Micro-Spectroscopy

In a first set of experiments, UV-Vis diffuse reflectance (DR) micro-spectroscopy was used to study the catalytic performance of the parent (P-ZSM-5) crystal as well as of the two steamed ZSM-5 crystals, i.e., MT-ZSM-5 (steamed at 500 °C) and ST-ZSM-5 (steamed at 700 °C). A large variety of coke (precursor) species are formed during the MTH reaction. This is evident when inspecting Figure 3.2, which shows the gradual formation of a set of broad and overlapping absorption bands. The main absorption bands observed are located between 350 and 450 nm and between 500 and 600 nm, which steadily grow in intensity with increasing time-on-stream. This is especially the case for the P-ZSM-5 and MT-ZSM-5 samples, whereas the UV-Vis DR spectra of ST-ZSM-5 are less pronounced at higher wavenumbers. Four representative Gaussian functions were chosen to deconvolute the UV-Vis DR spectra to characterize the formation of different hydrocarbon and coke (precursor) species. The locations of the Gaussian functions used to deconvolute the spectra are summarized in Figure 3.3. Next to absorption band intensity changes, one can also notice the red shifts and appearance of new absorption bands during the MTH process.

The first UV-Vis DR absorption band formed is located at ~350 nm and could be observed for all zeolite ZSM-5 crystals under study. Previously, the band at ~ 350 nm was assigned to ~ 3 methyl groups substituted methylbenzenium ions that constitute of catalytic scaffold of MTH reaction, i.e., the hydrocarbon pool (HCP) species.^[12] The second absorption band that formed was located at ~ 400-420 nm, which was only observed in P-ZSM-5 and MT-ZSM-5. The absorption band at ~ 400 nm was previously assigned to π - π^* transitions originated from methyl substituted benzenium cations.^[13,14] Literature data indicate that the formation of hexamethylbenzene at 387 nm was reported to shift to 414 nm with further methylation to heptamethylbenzene with increasing time on stream.^[15]

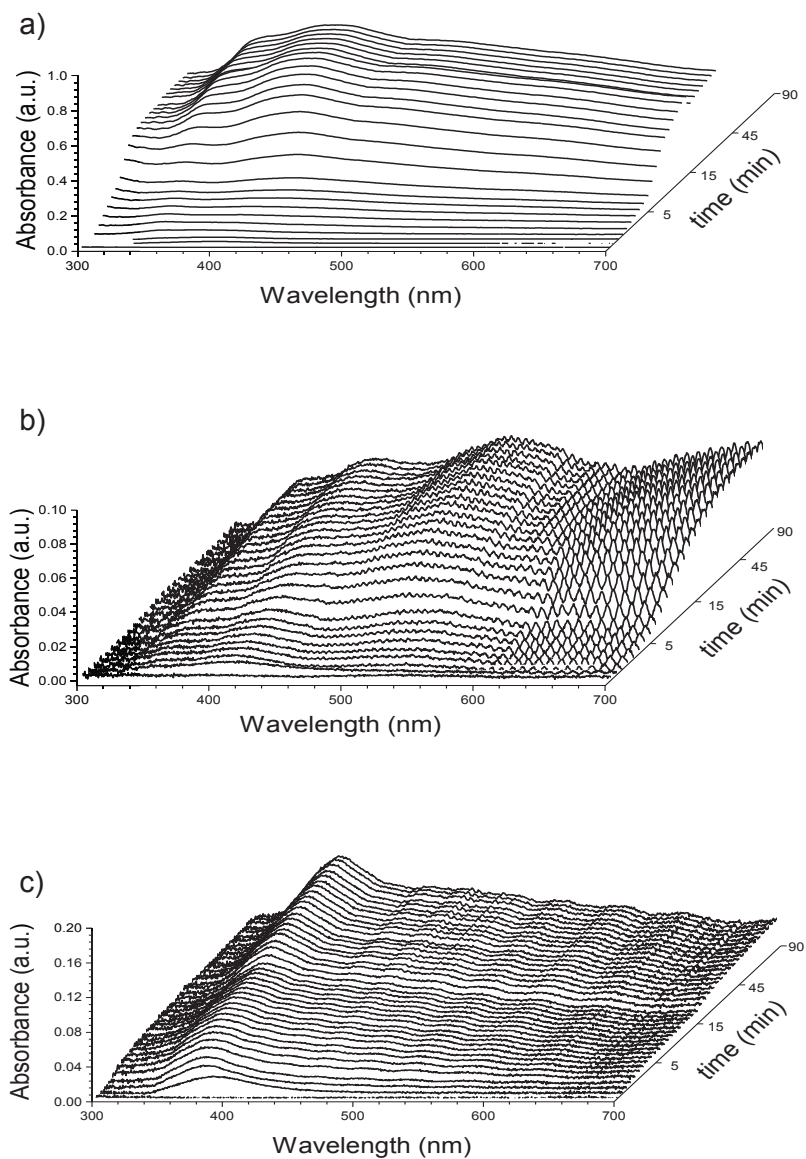
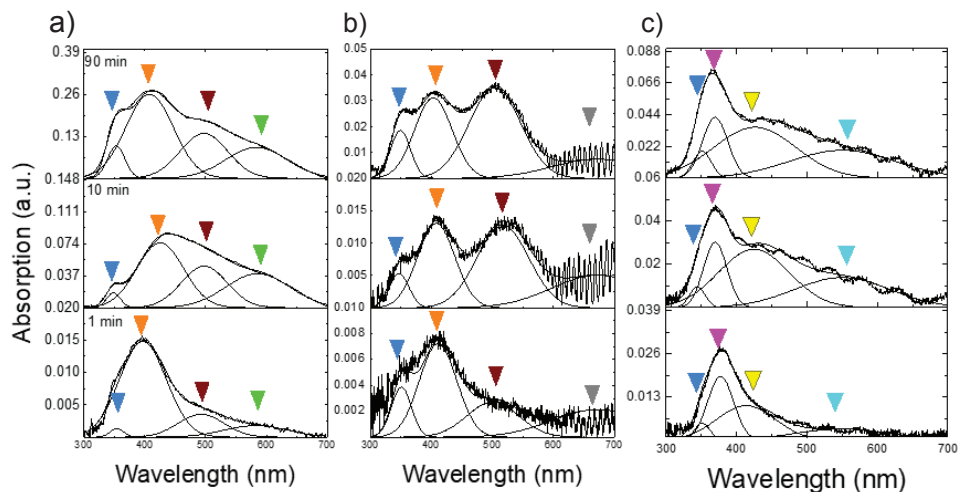


Figure 3.2. UV-Vis diffuse reflectance (DR) spectra of a) P-ZSM-5, b) MT-ZSM-5 and c) ST-ZSM-5 crystal reacted for 90 min under MTH conditions. The spectra were taken from the middle region of the top view (roof) of zeolite ZSM-5 crystals.



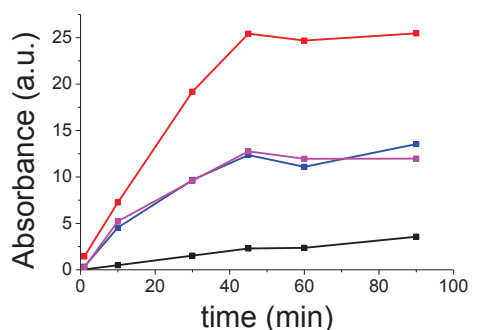
d)

Laser Wavelength (nm)	Species	Band # (nm)	Assignment of Hydrocarbon species
405	a	353	~3 methyl substituted methylbenzenium ^[38]
	b	375	Dienylic cations ^[44]
	c	400-420	Methyl-substituted benzenium cations ^[20]
	d	430	Trienylic carbenium ^[32]
488	e	500	Cationic methylated aromatics ^[32]
	f	550	Further conjugated benzenium ^[19]
561	g	580	Carbocationic large species ^[39]
642	h	>675	Polycondensed aromatics ^[32]

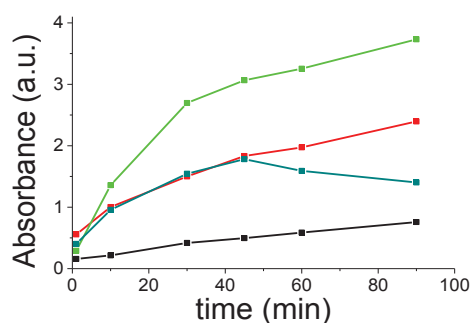
Figure 3.3. The deconvolution procedure applied to the UV-Vis diffuse reflectance (DR) spectra of a) P-ZSM-5 b) MT-ZSM-5 c) ST-ZSM-5 crystal reacted for 90 min under MTH conditions. Lasers with their respective wavelength used for the CFM study are indicated in the spectra. d) Assignment of the hydrocarbon species.

However, for the ST-ZSM-5 zeolite sample another UV-Vis absorption band was formed at ~380 nm, which is ascribed to dienylic cations.^[12] On the other hand, for the P-ZSM-5 and MT-ZSM-5 samples an absorption band at ~500 nm was formed with increasing time-on-stream. This UV-Vis absorption band was previously ascribed to cationic methylated aromatics.^[16] Separately, another absorption band was observed only on the ST-ZSM-5 crystal at ~430 nm. Previously, researchers assigned this absorption band to trienylic cations on various zeolites.^[12,17,18] This band is located clearly further in the spectra than the band of methyl substituted benzenium cations (~400-420 nm) which formed for the zeolite P-ZSM-5 and MT-ZSM-5 crystals. Possibly the formation of dienylic cations which is at ~380 nm, prevented the observation of the band of methyl substituted benzenium cations. Another possibility is that due to the decreased amount of Brønsted acid sites caused by severe steaming conditions, the formation of the (poly-)methylated benzenium cations did not take place.

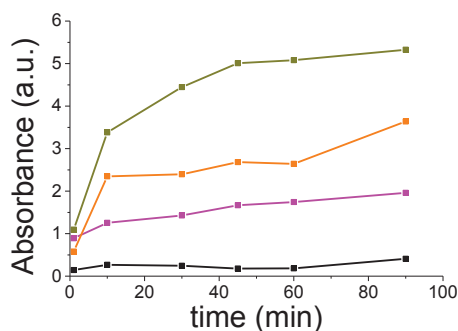
When the MTH reaction further progresses an absorption band at ~ 580 nm was observed for the P-ZSM-5 crystal, which was ascribed previously to large carbocationic species.^[19] Although this band was not observed for the MT-ZSM-5 crystal, possibly due to mesopores formation via steaming, a growth of even larger hydrocarbon species with an absorption band at ~ 672 nm was observed. This band was previously ascribed to polyaromatic hydrocarbons (PAHs).^[20] On the other hand, the ST-ZSM-5 crystals gave rise to an absorption band at ~ 550 nm, which was lower in intensity than the absorption bands of large hydrocarbon species detected within P-ZSM-5 (~ 580 nm) and MT-ZSM-5 (~ 672 nm). This absorption band was also ascribed to π - π^* transitions from extended coke molecules.^[16] It is known that polymethylated benzenes form within zeolite channels and participate in the catalytic scaffold to form reaction products, while the polycondensed aromatic species form only on the external zeolite surface due to lower steric hindrance on the catalyst surface.^[14,19,21] The hydrocarbon species that are spectroscopically visible and are characterized by absorption bands above 600 nm are too large to form inside the microporous network of the large zeolite ZSM-5 crystals. Instead, these hydrocarbon species form on the zeolite outer surface and cause surface blocking.^[16] Due to the formation of mesoporosity via steaming, the bigger reaction products could form within the steamed crystals. The largest reaction product, characterized by an absorption band located at ~ 675 nm, was formed within the MT-ZSM-5 crystal. Although the ST-ZSM-5 crystal had more mesopores/defect formation, larger reaction species did not form due to the presence of a low number of relatively weak Brønsted acid sites, which prevented further conjugation of the formed hydrocarbon species.



Bands (nm)
 —■— 350 —●— 400-420 —▲— 500 —■— 582



Bands (nm)
 —■— 350 —●— 400-420 —■— 500 —▲— 672



Bands (nm)
 —■— 350 —■— 360-380 —■— 425 —■— 550

Figure 3.4. The temporal evolution of the intensities of the UV-Vis absorption bands during MTH process in zeolite a) P-ZSM-5 b) MT-ZSM-5 c) ST-ZSM-5 crystals.

Table 1. Time-on-stream development of the Gaussian bands used for deconvolution of the UV-Vis DR spectra for the MTH reaction over zeolite ZSM-5 crystals.

Crystal	time	Position of the Gaussian curves (nm)			
P-ZSM-5	1 min	354 ^a	397 ^c	493 ^e	582 ^g
	10 min	349 ^a	425 ^c	497 ^e	585 ^g
	30 min	349 ^a	417 ^c	501 ^e	587 ^g
	45 min	351 ^a	412 ^c	499 ^e	585 ^g
	60 min	351 ^a	410 ^c	498 ^e	580 ^g
	90 min	353 ^a	408 ^c	497 ^e	583 ^g
MT-ZSM-5	1 min	350 ^a	410 ^c	500 ^e	672 ^h
	10 min	347 ^a	408 ^c	517 ^e	672 ^h
	30 min	350 ^a	410 ^c	500 ^e	672 ^h
	45 min	350 ^a	410 ^c	504 ^e	672 ^h
	60 min	350 ^a	406 ^c	501 ^e	672 ^h
	90 min	349 ^a	403 ^c	504 ^e	672 ^h
ST-ZSM-5	1 min	351 ^a	377 ^b	413 ^d	550 ^f
	10 min	344 ^a	370 ^b	425 ^d	550 ^f
	30 min	350 ^a	368 ^b	425 ^d	550 ^f
	45 min	354 ^a	367 ^b	425 ^d	550 ^f
	60 min	353 ^a	367 ^b	425 ^d	550 ^f
	90 min	350 ^a	368 ^b	424 ^d	550 ^f

Figure 3.4 summarizes the intensity changes of the different absorption bands taking place during the MTH reaction over P-ZSM-5, MT-ZSM-5 and ST-ZSM-5 as a function of time. The general trend in the intensity changes of the UV-Vis absorption bands was an initial strong increase that with increasing time-on-stream. However, there are some exceptions, such as the formation of the largest (by-) products detected in the UV-Vis DR region for P-ZSM-5 (~ 580 nm) and MT-ZSM-5 (~ 672 nm), as shown in Figure 3.4g-h, which indicates that the mesopores formed within MT-ZSM-5 allows to give rise to the

formation of larger hydrocarbon species for MT-ZSM-5 than for P-ZSM-5. These larger hydrocarbon species become however less dominant after 45 min-on-stream, suggesting that they are either cracked further to smaller hydrocarbon fragments or turned into graphitic coke.^[37,38] These observations clearly implied that catalyst deactivation via the formation of different coke (precursor) species can be altered via post-synthesis treatments, such as steaming. The effluent gas analysis was done simultaneously with measuring UV-Vis DR measurements of the three distinct zeolite ZSM-5 crystals under study and the results are summarized in Figure 3.5. Unfortunately, due to the large dead volume inside the reaction-spectroscopy cell it was difficult to quantify the amounts of the different reaction products formed, and we have to limit our discussions to qualitative observations. Conversion of methanol to dimethyl ether (DME) rapidly started for each zeolite crystal when it was exposed to methanol.

A subsequent decrease of the amount of DME in the effluent gas stream started less than ten minutes after starting the MTH reaction. Apart from the synthesis of DME, the formation of the main MTH products, namely of ethene and propene, was detected for P-ZSM-5, MT-ZSM-5 and ST-ZSM-5. In each case, ethene was observed to be favored over propene. It was previously reported that the HCP mechanism in zeolite ZSM-5 predominantly yields ethene over propene.^[22]

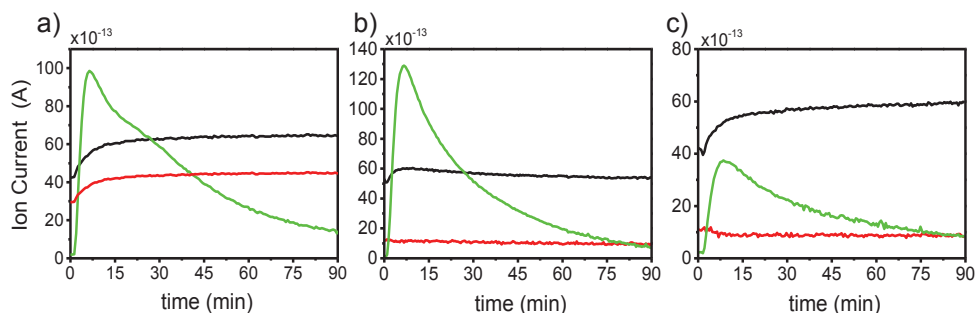


Figure 3.5. Evolution of the effluent gas composition of ethene (—), DME (—) and propene (—) from the reaction cells with increasing time-on-stream during the MTH process over a) P-ZSM-5, b) MT-ZSM-5 and c) ST-ZSM-5.

3.3.2. Operando Confocal Fluorescence Microscopy

UV-Vis DR spectroscopy provided detailed information on the nature of the hydrocarbon and coke (precursor) species. However, no spatial information could be obtained by this method. In order to locate the different hydrocarbon species within a large ZSM-5 crystal we have used in-situ confocal fluorescence microscopy. As the catalytic scaffold during the MTH process consists of various hydrocarbon

species we have irradiated the three sets of zeolite ZSM-5 crystals with four different linearly polarized lasers with wavelengths at 404, 488, 561, and 640 nm and performed these micro-spectroscopy experiments under MTH reaction conditions. The results are shown in Figures 3.6-8 for P-ZSM-5, MT-ZSM-5 and ST-ZSM-5.

The fluorescence that is observed within the zeolites upon methanol exposure under MTH reaction conditions can be ascribed to the formation of large and conjugated fluorescent molecules, which can be excited by the different laser frequencies. Due to their conjugated nature, one can postulate that they can be considered as coke (precursor) species occluded within the zeolite framework pore network, which constitutes of intersecting sinusoidal and straight pores. Furthermore, light absorption at higher wavelengths indicates the presence of more conjugated and extended coke (precursor) species.^[4,13,16,23] Figure 3.3 indicates the respective laser used, and their connection to the absorption bands in the UV-Vis region, which are associated with the formation of specific coke (precursor) species. On the other hand, by inspecting the fluorescence microscopy images in Figures 3.6-8 one can notice a decreasing fluorescence with increasing time on stream during the MTH process, which is related to the formation of further conjugated and more complex coke species.^[13] Researchers also have reported that these conjugated molecules might be too big to fit inside the pore channels of ZSM-5, and are therefore preferentially located at defect sites, near the intersection of pore channels and/or at the external surface of the zeolite crystal. For example, the 561 nm laser was reported to excite larger cationic aromatics characterized by polymethylation and consisting of two or three fused benzene rings. It was also proposed that the 640 nm laser excited even bigger coke-type molecules, such as anthracenes and naphthalenes.^[13,16,24,25] In addition, with linearly polarized lasers it becomes even possible to distinguish between specifically oriented reaction products and/or coke (precursor) species with respect to the pore architecture of the zeolite ZSM-5 crystals. Fluorescent molecules formed within the sinusoidal pores of the ZSM-5 crystals become visible when the crystals are oriented in the vertical direction with respect to the polarized laser, whereas fluorescent molecules located within the straight pores become visible when the zeolite ZSM-5 crystal is placed horizontally with respect to the laser direction.^[26-28]

None of the zeolite ZSM-5 crystals under study showed any significant fluorescence beforehand the methanol exposure; and fluorescence was immediately formed when the crystals were exposed to methanol under MTH reaction conditions. The time-dependent formation of fluorescent molecules during the MTH process showed different trends for the parent and steamed ZSM-5 crystals. Figure 3.6a shows the formation of fluorescent molecules within the P-ZSM-5 crystal upon 405,

488, 561, and 640 nm laser excitation. In order to obtain spatial information, the overall fluorescence emitted from the ZSM-5 crystals was separated into three regions of interests (ROI) at the crystal edge, the mid-crystal region and at the crystal tip (each ROI was chosen as $3 \times 3 \mu\text{m}^2$, Figure 3.6c). The fluorescence intensities were counted for each ROI throughout the MTH reaction. The averaged normalized fluorescence intensities on a P-ZSM-5 crystal as a function of time-on-stream are shown in Figure 3.6b. The normalization procedure is done with respect to maximum fluorescence light intensity. The zeolite P-ZSM-5 crystal oriented horizontally with respect to the linear light direction showed a rapidly increasing fluorescence that faded after its plateau was reached. This trend was observed for all the excitation wavelengths used for measuring the zeolite P-ZSM-5 crystal. It is clear that the straight pores allowed the formation of more conjugated carbonaceous species. The use of longer laser wavelength allowed to observe larger fluorescent molecules which took longer to reach a fluorescence plateau. Moreover, due to the relative zeolite crystal orientation with the polarized light, the fluorescence intensity for both the crystal mid-region and the edge region were very similar, while the crystal tip had the lowest the fluorescence intensity. When the zeolite crystal was rotated by 90° (i.e., the vertical orientation), a fluorescent rim became apparent at the crystal tips and edges, which visualizes the distribution of fluorescent molecules within the sinusoidal pore system. In this orientation, neither a plateau formation nor a decrease in fluorescence was observed. This observance indicates that the formation of non-fluorescent and large hydrocarbon species did not take place due to the more tortuous sinusoidal pore channels.

In an analogous manner, we have investigated the MT-ZSM-5 crystal and the results are shown in Figure 3.7. The fluorescence formed within the zeolite crystal during the MTH reaction did not fade away with the exception when the 561 nm excitation laser was used (Figure 3.7b). The formation of fluorescence had an overall increasing and stabilizing trend for the parallel oriented MT-ZSM-5 crystal. The trends in spatiotemporal formation of fluorescence within the MT-ZSM-5 crystal had some similarities with the P-ZSM-5 crystal. Due to the crystal orientation, the fluorescence on the MT-ZSM-5 crystal tip was again the lowest. However, unlike the P-ZSM-5, the mid-region of the MT-ZSM-5 crystal had the highest coke concentration most probably due to the presence of mesopores that facilitated a better mass transfer of the fluorescent molecules, which could diffuse deeper in the zeolite crystal. A vertically oriented zeolite ZSM-5 crystal had a very different spatiotemporal trend in fluorescence. The formation of fluorescent molecules reached very rapidly onto a maximum fluorescence plateau and then decreased in intensity. This decrease in fluorescence intensity can also be explained by the further conjugation of the formed fluorescent species as the UV-Vis diffuse reflectance

micro-spectroscopy measurements showed. The conjugation of formed species within the sinusoidal pores could be possible since the spatial constraints in the zeolite MT-ZSM-5 crystals were lowered due to the formation of mesopores and defects. Dealumination also lead to a lower number of Brønsted acid sites, which prevented the formation of more fluorescent hydrocarbons as there was no decay in fluorescence with increasing time-on-stream observed. Steaming lowered both the mass transfer limitations and the amount of Brønsted acid sites of the crystal. However, the crystal was still active enough to catalyze the formation of conjugated species. Furthermore, as for the P-ZSM-5 crystal, the observed fluorescence in the vertically oriented MT-ZSM-5 crystal indicates the formation of fluorescent molecules within the sinusoidal pores. As steaming was reported to alter the sinusoidal pores more than the straight pores, one can expect to observe more fluorescence intensity for the MT-ZSM-5 crystal, which is indeed the case, especially for short reaction times and when long wavelength laser excitations are used.^[29,30]

In a final step of our study, we have investigated the ST-ZSM-5 crystal in detail and the results are shown in Figure 3.8. Upon exposure of methanol to the ST-ZSM-5 crystal under MTH conditions, no significant decrease in fluorescence was observed at any moment in the MTH process when the reaction time increases. This was the case for each of the zeolite crystal orientations investigated. The severe dealumination procedure applied decreased the overall Brønsted acid density, which prevented the formation of more conjugated fluorescent molecules. On the other hand, the formation of a lot of mesopores facilitated the diffusion properties of the ZSM-5 crystal. The vertically oriented ST-ZSM-5 crystal had therefore a more homogeneous distribution of fluorescent molecules, as compared to P-ZSM-5 and MT-ZSM-5. Therefore, the homogeneous distribution of fluorescent molecules within the vertically oriented ST-ZSM-5 crystal shows the extent of improved diffusion capabilities of this crystal.

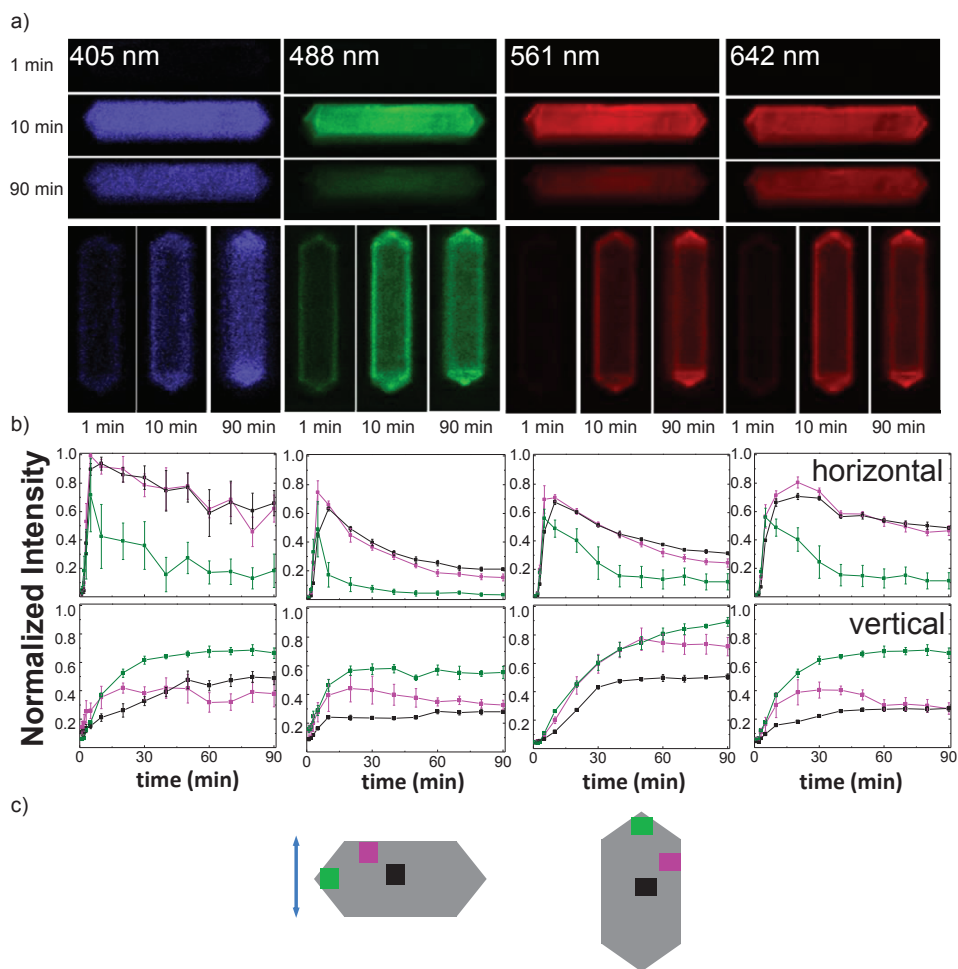


Figure 3.6. a) Fluorescence intensity distribution from a single P-ZSM-5 crystal. The fluorescence microscopy images at the top describe the zeolite crystal placed with its long axis parallel to the analyzer and the images at the bottom describe the zeolite crystal placed with its short axis parallel to the analyzer after 1, 10 and 90 min time-on-stream during MTH conditions. The crystal was irradiated with four laser sources at 405, 488, 561 and 640 nm, respectively. b) The intensity profile of the fluorescence microscopy measurements shown in (a). c) Locations of the selected regions of interests on the parallel and vertical oriented crystals. The blue arrows show the direction of the polarized light used to collect the fluorescence microscopy images.

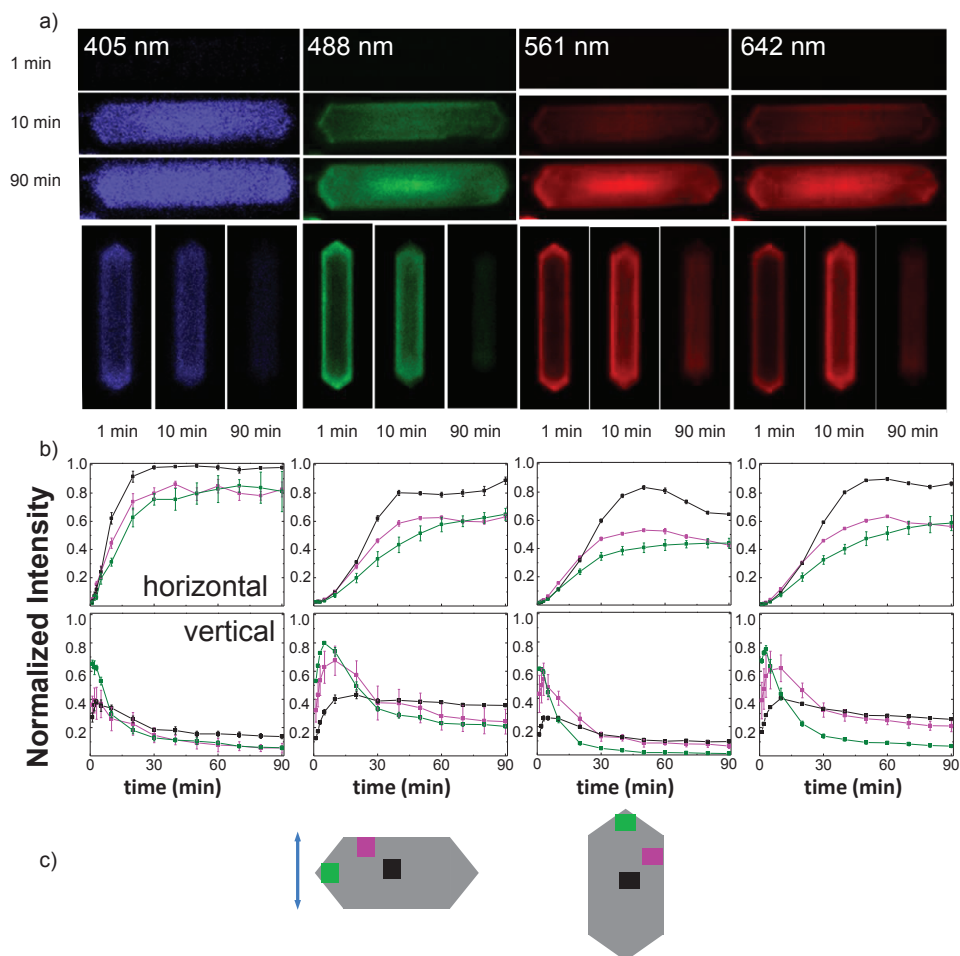


Figure 3.7. a) Fluorescence intensity distribution from a single MT-ZSM-5 crystal. The fluorescence microscopy images at the top describe the zeolite crystal placed with its long axis parallel to the analyzer and the images at the bottom describe the zeolite crystal placed with its short axis parallel to the analyzer after 1, 10 and 90 min time-on-stream during MTH conditions. The crystal was irradiated with four laser sources at 405, 488, 561 and 640 nm, respectively. b) The intensity profile of the fluorescence microscopy measurements shown in (a). c) Locations of the selected regions of interests on the parallel and vertical oriented crystals. The blue arrows show the direction of the polarized light used to collect the fluorescence microscopy images.

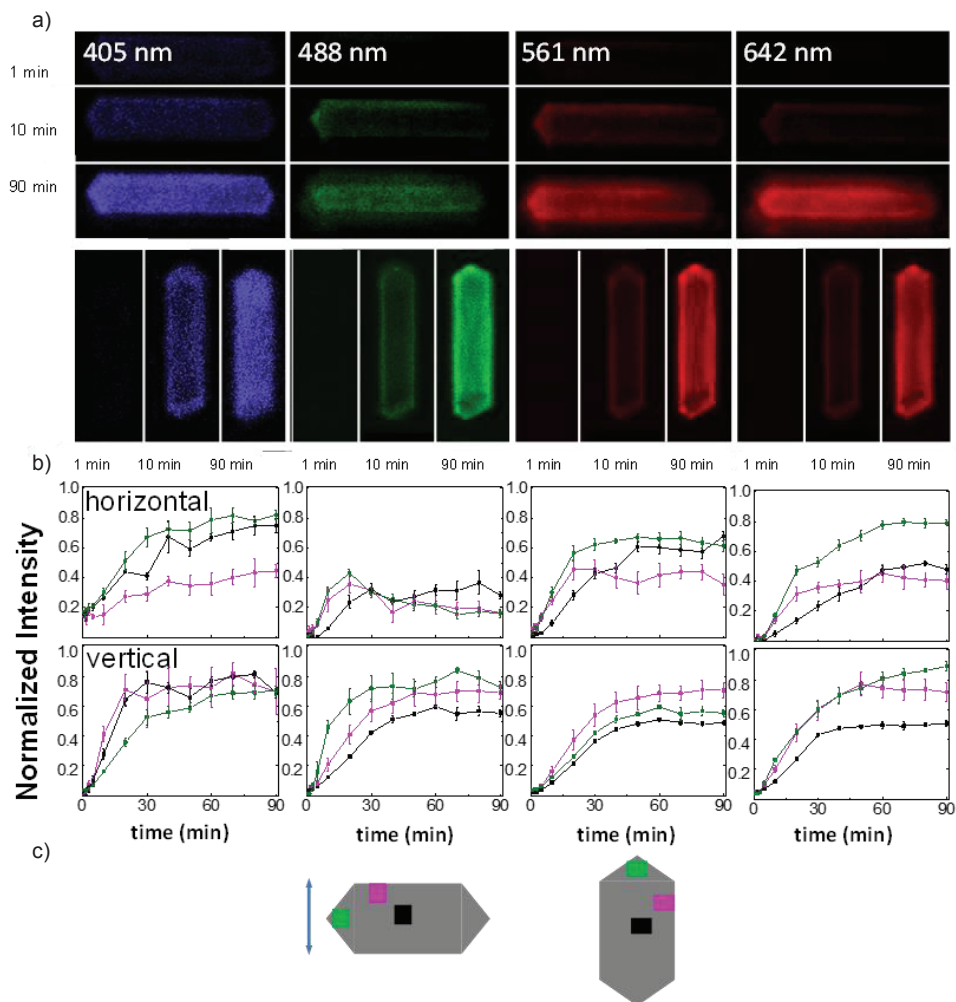


Figure 3.8. a) Fluorescence intensity distribution from a single ST-ZSM-5 crystal. The fluorescence microscopy images at the top describe the zeolite crystal placed with its long axis parallel to the analyzer and the images at the bottom describe the zeolite crystal placed with its short axis parallel to the analyzer. The images were taken after 1, 10 and 90 min time-on-stream during MTH conditions. The crystal was irradiated with four laser sources at 405, 488, 561 and 642 nm, respectively. b) The intensity profile of the fluorescence microscopy measurements shown in (a) c) Locations of the selected regions of interest on the parallel and vertical oriented crystals. The blue arrows show the direction of the polarized light used to collect the fluorescence microscopy images.

3.4. Conclusions

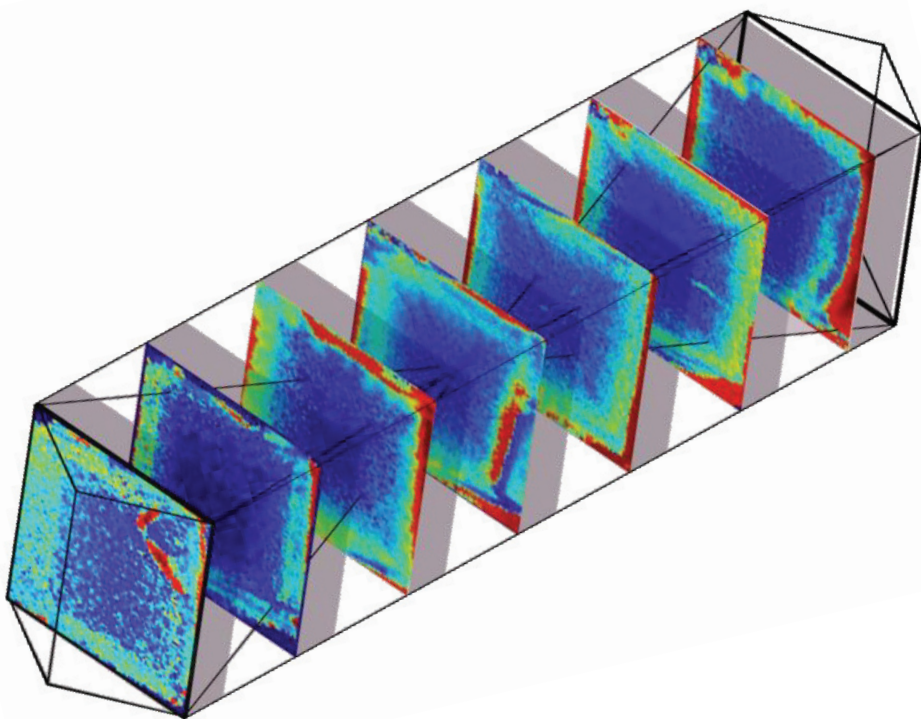
In this Chapter, the catalytic activities of parent and steamed large zeolite ZSM-5 crystals during the Methanol-to-Hydrocarbons (MTH) process have been studied and compared with operando micro-spectroscopy. It was found that the initial coke (precursor) formation starts very rapidly after exposing the zeolite ZSM-5 crystals to methanol under reaction conditions. The coke (precursor) species enlarge in molecular sizes within the zones rich in Brønsted acid sites and their formation gradually decrease the diffusion capabilities of other molecules within the zeolite crystal. Coke formation in the parent and steamed zeolite ZSM-5 crystals showed distinct differences due to the presence of mesopores/defects and the lowered Brønsted acid sites in the steamed zeolite ZSM-5 crystals. The only common coke intermediate formed in each studied zeolite crystal, regardless of their Brønsted acid site density, was the trimethylbenzenium ions. The highest amount of coke was observed in parent zeolite ZSM-5 crystals that also contained the highest Brønsted acid site density and the lowest amount of mesopores and defect sites. Mild steam treatment of ZSM-5 crystals formed mesopores/defect formations that facilitated the production of more bulky reaction products due to lowered spatial constraints. In contrast, severe steaming of zeolite ZSM-5 crystals did not indicate the formation of any larger hydrocarbons species due to the lower number of Brønsted acid sites. Confocal fluorescence microscopy, by using different laser frequencies, allowed to spatially mapping the coke accumulation within the zeolite ZSM-5 crystals. The gradual formation of more conjugated coke (precursor) species under MTH reaction conditions was observed by monitoring the decreasing fluorescence signal intensity. The first conjugated coke (precursor) species were found to be present in the straight pores of parent zeolite ZSM-5 crystals, especially in the edge regions. Interestingly, due to a larger accessibility the same species could be found in the straight pores of the core region of the mildly steamed zeolite ZSM-5 crystals. However, for these crystals one could also observe hydrocarbon species in the sinusoidal channels where rapid coke formation and further conjugation took place. Possibly, the enlarging coke species formed within the sinusoidal channels were transported through the straight channels through the formed mesopores. On the other hand, the severely steamed zeolite ZSM-5 crystal did not show any substantial accumulation of large conjugated hydrocarbon species. Due to its highest pore structure accessibility and lowest Brønsted acidity such large hydrocarbon species are not formed in a severely steamed ZSM-5 crystal. A schematic summarizing the main findings of this Chapter is given in Figure 3.9.

Attila and Florian Meirer (UU). Data interpretation was done by Özgün Attila, Florian Meirer and Bert Weckhuysen (UU). Bert Weckhuysen has made revisions and corrections to the chapter.

References

- [1] E. T. C. Vogt, G. T. Whiting, A. Dutta Chowdhury, B. M. Weckhuysen, *Adv. Catal.* **2015**, *58*, 143–314.
- [2] K. Tanabe, *Appl. Catal. A Gen.* **1999**, *181*, 399–434.
- [3] T. Chmielniak, M. Sciazko, *Appl. Energy* **2003**, *74*, 393–403.
- [4] Q. Qian, J. Ruiz-Martínez, M. Mokhtar, A. M. Asiri, S. A. Al-Thabaiti, S. N. Basahel, H. E. van der Bij, J. Kornatowski, B. M. Weckhuysen, *Chem. Eur. J.* **2013**, *19*, 11204–11215.
- [5] B. Xu, S. Bordiga, R. Prins, J. A. van Bokhoven, *Appl. Catal. A Gen.* **2007**, *333*, 245–253.
- [6] J. Huang, Y. Jiang, V. R. R. Marthala, B. Thomas, E. Romanova, M. Hunger, *J. Phys. Chem. C* **2008**, *112*, 3811–3818.
- [7] B. Xu, C. Sievers, S. B. Hong, R. Prins, J. A. van Bokhoven, *J. Catal.* **2006**, *244*, 163–168.
- [8] C. Seebacher, J. Rau, F. W. Deeg, C. Bräuchle, S. Altmaier, R. Jäger, P. Behrens, *Adv. Mater.* **2001**, *13*, 1374–1377.
- [9] Y. Wei, T. E. Parmentier, K. P. de Jong, J. Zečević, *Chem. Soc. Rev.* **2015**, *44*, 7234–7261.
- [10] L. R. Aramburo, L. Karwacki, P. Cubillas, S. Asahina, D. A. M. De Winter, M. R. Drury, I. L. C. Buurmans, E. Stavitski, D. Mores, M. Daturi, P. Bazin, P. Dumas, F. Thibault-Starzyk, J. A. Poost, M. W. Anderson, O. Terasaki, B. M. Weckhuysen, *Chem. Eur. J.* **2011**, *17*, 13773–13781.
- [11] J. P. Hofmann, D. Mores, L. R. Aramburo, S. Teketel, M. Rohnke, J. Janek, U. Olsbye, B. M. Weckhuysen, *Chem. Eur. J.* **2013**, *19*, 8533–8542.
- [12] M. J. Wulfers, F. C. Jentoft, *ACS Catal.* **2014**, *4*, 3521–3532.
- [13] E. C. Nordvang, E. Borodina, J. Ruiz-Martinez, R. Fehrmann, B. M. Weckhuysen, *Chem. Eur. J.* **2015**, *21*, 17324–17335.
- [14] D. Mores, E. Stavitski, M. H. F. Kox, J. Kornatowski, U. Olsbye, B. M. Weckhuysen, *Chem. Eur. J.* **2008**, *14*, 11320–11327.
- [15] A. D. Chowdhury, K. Houben, G. T. Whiting, M. Mokhtar, A. M. Asiri, S. A. Al-Thabaiti, S. N. Basahel, M. Baldus, B. M. Weckhuysen, *Angew. Chem. Int. Ed.* **2016**, 16072–16077.
- [16] D. Mores, J. Kornatowski, U. Olsbye, B. M. Weckhuysen, *Chem. Eur. J.* **2011**, *17*, 2874–2884.

- [17] Y. Jiang, J. Huang, V. R. Reddy Marthala, Y. S. Ooi, J. Weitkamp, M. Hunger, *Microporous Mesoporous Mater.* **2007**, *105*, 132–139.
- [18] I. Kiricsi, H. Förster, G. Tasi, J. B. Nagy, *Chem. Rev.* **1999**, *99*, 2085–2114.
- [19] L. Palumbo, F. Bonino, P. Beato, M. Bjørgen, A. Zecchina, S. Bordiga, *J. Phys. Chem. C* **2008**, *112*, 9710–9716.
- [20] M. Ibáñez, M. Gamero, J. Ruiz-Martínez, B. M. Weckhuysen, A. T. Aguayo, J. Bilbao, P. Castaño, *Catal. Sci. Technol.* **2016**, *6*, 296–306.
- [21] U. Olsbye, M. Bjørgen, S. Svelle, K. P. Lillerud, S. Kolboe, *Catal. Today* **2005**, *106*, 108–111.
- [22] S. Svelle, U. Olsbye, F. Joensen, M. Bjørgen, *J. Phys. Chem. C* **2007**, *111*, 17981–17984.
- [23] E. Stavitski, M. H. F. Kox, B. M. Weckhuysen, *Chem. Eur. J.* **2007**, *13*, 7057–7065.
- [24] R. Y. Brogaard, B. M. Weckhuysen, J. K. Nørskov, *J. Catal.* **2013**, *300*, 235–241.
- [25] V. van Speybroeck, K. Hemelsoet, K. De Wispelaere, Q. Qian, J. van der Mynsbrugge, B. de Sterck, B. M. Weckhuysen, M. Waroquier, *ChemCatChem* **2013**, *5*, 173–184.
- [26] A. V. Kubarev, E. Breynaert, J. van Loon, A. Layek, G. Fleury, S. Radhakrishnan, J. A. Martens, M. B. J. Roeffaers, *ACS Catal.* **2017**, 4248–4252.
- [27] C. Sprung, B. M. Weckhuysen, *J. Am. Chem. Soc.* **2015**, *137*, 1916–1928.
- [28] F. C. Hendriks, J. E. Schmidt, J. A. Rombouts, K. Lammertsma, P. C. A. Bruijninx, B. M. Weckhuysen, *Chem. Eur. J.* **2017**, *23*, 6305–6314.
- [29] L. R. Aramburo, J. Ruiz-Martínez, J. P. Hofmann, B. M. Weckhuysen, *Catal. Sci. Technol.* **2013**, *3*, 1208–1214.
- [30] L. Karwacki, D. A. M. De Winter, L. R. Aramburo, M. N. Lebbink, J. A. Post, M. R. Drury, B. M. Weckhuysen, *Angew. Chem. Int. Ed.* **2011**, *50*, 1294–1298.



CHAPTER IV

Coke Formation in Large Zeolite ZSM-5 Crystals during the Methanol-to-Hydrocarbons Process as Studied with Nano-Secondary Ion Mass Spectrometry

A combined approach of advanced ion probe techniques i.e., Nano-Secondary Ion Mass Spectrometry (NanoSIMS) and Electron microProbe (EPMA), and operando UV-Vis micro-spectroscopy were used to spatially resolve the elemental composition of the zeolite ZSM-5 framework and to follow the formation of coke (precursor) species during the Methanol-to-Hydrocarbons (MTH) process within a zeolite ZSM-5 crystal. In the near surface regions of a zeolite ZSM-5 crystal, we have observed a gradually decreasing Al-rich zone where the MTH process predominantly takes place. We furthermore detected the diffusion barriers that are formed by connecting the zeolite crystal subunits. Based on the experimental data we propose a model for the dynamics of coke formation that starts in the silicalite-rich zeolite outer surface. The coke (precursor) species formed, desorb on the catalyst surface and form a thickening surface coverage, which gradually lowers the pore accessibility, in turn causing catalyst deactivation.

4.1. Introduction

A significant fraction of the growing global demand for energy is currently met by the exploitation of fossil resources, including coal, natural gas and crude oil. The increasing demand for fossil-derived fuels, chemicals and materials comes with significant climate-change risks, which should be mitigated.^[1,2] As a consequence, renewables must be developed to continue supplying the world with the necessary chemicals, materials and fuels in a more sustainable manner. Here, methanol has been proposed as a promising crude oil substitute as it can be directly obtained from either fossil (e.g., natural gas and coal) or renewable feedstocks (e.g. biomass and waste). The methanol produced can then be converted via zeolite-based catalysts into gasoline-range hydrocarbons or light, polymer-grade olefins via the so-called Methanol-to-Hydrocarbons (MTH) process.^[3-5] Zeolite ZSM-5 possessing the MFI framework topology^[6] is one of the two commercially important zeolites for conducting the MTH process.^[7] Methanol-based conversion processes provide a new and feasible “methanol economy” as an alternative to diminishing crude oil resources, as well as provide a path towards a more sustainable society, which is less dependent on fossil resources.^[8,9]

In this study, we have made use of large zeolite ZSM-5 crystals (100 x 20 x 20 μm^3), which have been studied in detail by our group. Zeolite ZSM-5 crystals are reported to have a two-component intergrowth structure model. This intergrowth structure indicates that the zeolite ZSM-5 crystals are formed by six distinct 90° rotated neighboring pyramidal subunits that generate interfaces (grain boundaries) with rotated pore arrangement.^[10-12] Such arrangements act as internal diffusion barriers, and change the accessibility of the active sites (i.e, the Brønsted acid sites) in the zeolite ZSM-5 crystals.^[13,14] Their large size and well-defined internal structures, composed of distinct intergrowth subunits, are ideal for the application of various micro- and nano-spectroscopic analyses, and in the past years our group has investigated these crystals with a wide variety of characterization techniques, including, Confocal Fluorescence Microscopy (CFM)^[15], Atomic Force Microscopy (AFM)^[16], X-ray Photoelectron Spectroscopy (XPS)^[12], Electron Backscattering Diffraction (EBSD)/ Scanning Electron Microscopy (SEM)^[11], Synchrotron-Based Micro X-Ray Diffraction Imaging.^[17] Based on these studies it was, for example, found that the zeolite ZSM-5 crystals have a non-homogeneous elemental distribution, including the amount of Al.^[12] Al enrichment in the outer shell of the TPA⁺-templated zeolite ZSM-5 crystals of various sizes is a known phenomenon.^[18-22] Van Bokhoven and co-workers related this Al enrichment either to the continuous migration of Al to the surface during crystal growth or to Al deposition on the zeolite

surface during cooling of the synthesis mixture.^[23] Apart from Al zoning, the characterization studies showed a silicalite layer formed on the zeolite crystal surface. Karwacki and coworkers reported the presence of a thin silicalite layer (< 200 nm) on the outermost surface of various large zeolite ZSM-5 crystals determined by XPS sputter-depth-profiling experiments. They related the silicalite layer formation to the synthesis procedure.^[12]

In the previous Chapter, the formation of coke (precursor) species within zeolite ZSM-5 crystals during the MTH process was studied. The formation and evolution of the coke (precursor) species from smaller polymethylated benzenium carbocations to polymethylated poly-aromatic carbocations were reported. In this Chapter, we present a study on the influence of the elemental framework composition of the zeolite ZSM-5 crystal on the spatial distribution of coke (precursor) species as a function of process conditions. Large zeolite ZSM-5 crystals, partially deactivated via the MTH conversion process, have been investigated using a combination of Nano Secondary Ion Mass Spectrometry (NanoSIMS) and Electron Probe Microanalysis (EPMA). NanoSIMS can differentiate between labeled isotopes.^[24] Therefore we have used ¹³C-labeled MeOH in order to separate the carbon signal from contaminations, such as carbon tape fragments from the NanoSIMS sample stage, the protective Pt/C layer used for FIB-cutting, and carbonaceous deposits from reaction (by-)products. NanoSIMS and EPMA were complemented with operando UV-Vis diffuse reflectance micro-spectroscopy measurements, which allowed visualizing the spatial distribution of aluminium atoms and relating them to the coke (precursor) species trapped within the zeolite framework structure. Based on these findings we have developed a model that describes the formation of coke (precursor) species during the MTH process within a single zeolite ZSM-5 crystal.

4.2. Experimental Section

4.2.1 Materials and Methods

Large zeolite ZSM-5 crystals with an average size of 100 x 20 x 20 μm^3 (bulk Si/Al = 17) were provided by Exxon-Mobil (Machelen, Belgium) in their sodium form. The starting chemicals for the synthesis of these zeolite ZSM-5 crystals were: Ludox AS40 (Sigma-Aldrich, 40 wt% in H₂O), tetrapropylammonium bromide (TPABr, Fluka, $\geq 98\%$), Al₂(SO₄)₃ · 18H₂O (Baker, 98%), and NH₄OH (VWR, 29%). The molar composition of the synthesis gel was 6.65 (NH₄)₂O/0.67 TPA₂O/0.025 Al₂O₃/10 SiO₂/121 H₂O. Their synthesis procedure has been reported elsewhere.^[16] The as-synthesized samples were first calcined at 500 °C with ramp rate of 1 °C.min⁻¹ for 12 h in air template in a flow oven to remove the. Subsequently, a triple ion exchange was performed with a 10 wt% ammonium nitrate (Acros Organics, 99+%) solution at

60 °C. After the repetition of the calcination step, the parent zeolite ZSM-5 crystals were obtained.

Methanol-to-Hydrocarbons (MTH) conversion reactions were performed in an in-situ reaction cell equipped with a quartz window for light microscopy (THMS 600, Linkam Scientific Instruments) with a temperature controller (Linkam TMS94). The large single zeolite ZSM-5 crystals were placed on a quartz plate in the in-situ reaction cell and subsequently heated to 120 °C (5 °C.min⁻¹ for 30 min) under an O₂ flow of 20 ml.min⁻¹ as the initial heating step before reaction. Then, the temperature was increased to 550 °C (5 °C.min⁻¹) for 60 min. This method removed all possible adsorbents from the zeolite crystals. Upon the completion of the calcination process, the temperature was decreased to the reaction temperature of 350 °C under 20 ml.min⁻¹ N₂ flow and methanol were introduced into the cell. The maximum reaction duration was chosen as 90 min to ensure the zeolite ZSM-5 crystals had sufficient occluded coke deposits for proper analysis but were not yet fully deactivated, as demonstrated in our previous work using this catalyst material.^[25] The MTH processes were performed using ¹³C labeled methanol (Sigma Aldrich, 99 at. %).

4.2.2 UV-Vis Diffuse Reflectance Micro-Spectroscopy

The operando UV-Vis Diffuse Reflectance Spectroscopy (DRS) measurements were performed with a CRAIC 20/30 PV™ UV-Vis micro-spectrophotometer using a 36X objective. A 75 W Xenon lamp was used for illumination. The large zeolite ZSM-5 crystals were loaded into a Linkam FTIR 600 cell equipped with a temperature controller (Linkam TMS94). The measurements were performed in the mid-crystal region with a 10x10 μm² spot size. The MTH reaction was performed using the aforementioned reaction conditions.

4.2.3 Focused-Ion-Beam Milling and Scanning Electron Microscopy

The non-conductive zeolite ZSM-5 crystals under study were too thick for performing the microprobe analyses. Therefore, thin cross-sections (~2-3 μm) were cut from the large zeolite crystals. Cross sections of the zeolite crystals for NanoSIMS and microprobe measurements were prepared using Focused Ion Beam (FIB) milling and subsequently analyzed by Scanning Electron Microscopy (SEM). Strips of protective Pt/C coating were deposited at pre-determined areas of interest across the zeolite ZSM-5 crystal. The non-coated parts of the zeolite crystal were removed with FIB. The remaining sections were transferred to an Omniprobe TEM copper grid (Cu-mount) using an in-situ micromanipulator. This process is demonstrated in Figure 4.1a-b. Before the sections were transferred to the

NanoSIMS and microprobe, one side was polished with FIB. Further preparation details are described elsewhere.^[12] Furthermore, the FIB-SEM technique was also used to measure the NanoSIMS sampling depth, as illustrated in Figure 4.1c.

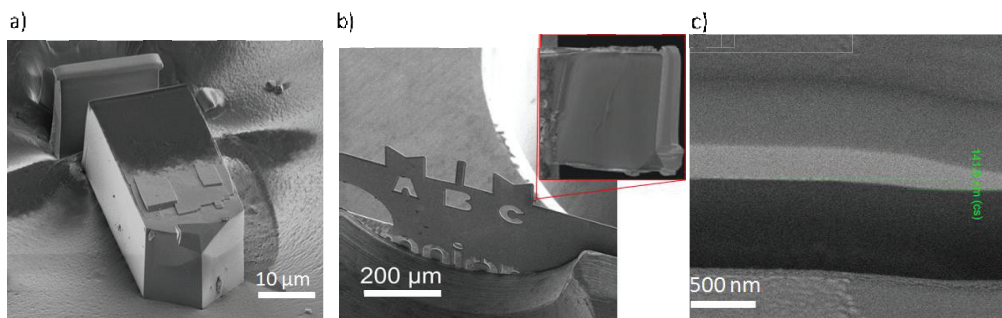


Figure 4.1. a) A cross-section separated from the zeolite crystal. b) The cross-section (red square) attached to an Omniprobe Cu TEM grid. c) Depth profile measured by the FIB-SEM software.

4.2.4 Atomic Force Microscopy

An upright Atomic Force Microscope (AFM) NTEGRA Spectra instrument of NT-MDT was employed to measure the depth of the probed volumes of the large zeolite ZSM-5 crystals with NanoSIMS. The results are given in Figure 4.2. Olympus AC160TD silicon tips coated with Al were used as a tip.

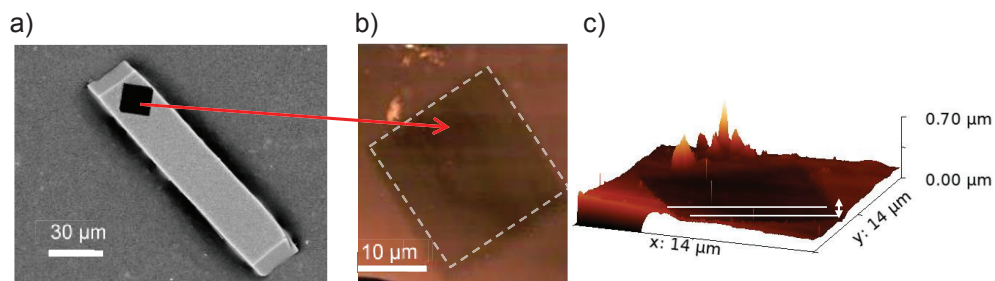


Figure 4.2. a) SEM image of a zeolite ZSM-5 crystal analyzed with NanoSIMS. b) AFM output of the crater formed by NanoSIMS on a zeolite ZSM-5 crystal (Top view, the crater is indicated by the dashed square). c) Perspective view of the crater shown in (b) The depth of the crater was measured as 220 nm (the depth indicated by the white lines).

4.2.5 Electron Probe Microanalyser

The distributions of C, Si, and Al atoms in the zeolite ZSM-5 crystals were measured using a JEOL JXA-8530F Field Emission Electron Probe Microanalyser (FE-EPMA). This instrument is equipped with an EDS detector for rapid material identification and a BSE detector was used for orientation and identification of the

various materials. The EPMA instrument has several wavelength dispersive spectrometers (WDS) installed. The beam conditions were set to 15 kV gun potential for point analyses and 10 kV for area analysis and a current of 20 nA. It is important to note that unlike NanoSIMS, EPMA cannot differentiate between isotopes of carbon. EPMA analyses were performed on the zeolite ZSM-5 cross-sections from MTH processes with reaction duration of 10 min and 90 min.

4.2.6 Nano-Secondary Ion Mass Spectrometry

Nano-Secondary Ion Mass Spectrometry (NanoSIMS) is an advanced ion probes commonly used in the field of cosmology, geosciences and cell research.^[26–28] Here, we have used this characterization tool for zeolite research. The Al, Si, O, ^{12}C and ^{13}C signals of a zeolite ZSM-5 crystal, reacting with ^{13}C labeled methanol during MTH, were measured in raster imaging mode NanoSIMS. Cs^+ was used as a source (~ 30000 pA) to scan over the sample surface areas under Ultra-High Vacuum (UHV) conditions with various sizes of 10×10 to $40 \times 40 \mu\text{m}^2$ depending on the location of the zeolite crystal being analyzed. Prior to each measurement, the analysis area was sputtered in raster scan mode by a high-current Cs^+ beam to implant Cs primary ions in order to collect secondary ions. Secondary ions of ^{12}C , ^{13}C , ^{16}O , ^{27}Al , and ^{28}Si were collected simultaneously in separate electron multipliers. Collected elemental yields from the Cs^+ ion beam insertion in the sample were high for high electron affinity elements, namely Si, O, and C. However, for the low electron affinity element Al, the signal was weak.^[29] In order to obtain higher Al signals, an O^- source was needed to be used instead of the Cs^+ source, but in this case, other important elemental signals would be low. Two types of analyses, i.e., depth profiling and mapping of the cross-sections prepared by FIB-SEM milling were performed.

Two-sided conductive 0.2 mm thick polycarbonate stickers with graphite powder mixed in the adhesive (Plano GmbH, Wetzlar, Germany) were placed on 1 cm diameter Al stubs (Ted Pella). For depth profiling experiments, zeolite ZSM-5 crystals under study were sprinkled onto the carbon tape. Due to the insulating nature of zeolitic materials, samples were covered with a few nm thick layer of conductive Au for charge dissipation. Prepared samples for NanoSIMS measurements are shown before and after gold coating are given in Figure 4.3. Moreover, an electron flood gun was also used to compensate for charging. Due to the loss of Au layer during rastering in-depth profiling, elemental and isotopic signals could not be collected deeper than ~ 150 - 200 nm of the crystal surfaces. Deeper spots in the crystals did not produce any data. As mentioned, the depth of the craters formed by the NanoSIMS ion beam was measured with AFM and FIB-SEM. The sputter-depth profile elemental output was normalized with respect to sputtering

repetitions and sputtering area size for comparability with other depth profiling measurements. Data processing was done with the Matlab based software Look@NanoSIMS.^[30]

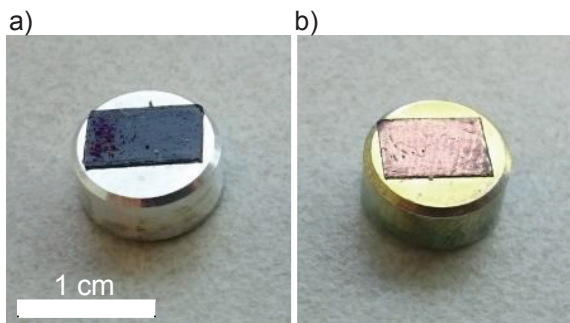


Figure 4.3. Large zeolite ZSM-5 crystals attached on the Al stubs ($\varnothing=1\text{cm}$) using double sided carbon tape. b) Al stub is covered with an Au layer ($\sim 7\text{ nm}$).

4.3. Results and Discussion

4.3.1. UV-Vis Micro-Spectroscopy

Prior to the sample preparation for doing the Electron Micro-Probe (EPMA) and Nano-Secondary Ion Mass Spectrometry (NanoSIMS) measurements, time-resolved UV-Vis micro-spectroscopy measurements were performed to choose the locations to be probed. For this reason, the microphotographs of the zeolite ZSM-5 crystals during the MTH process were taken in order to detect the spatiotemporal coke formation in the UV-Vis range of the spectrum. The UV-Vis diffuse reflectance spectra of the zeolite ZSM-5 crystal under MTH reaction conditions showed an overall increase in intensity. The MTH reaction spectra is given in Figure 4.4a. After an initial formation of absorption bands at around 350 and 400 nm, an absorption band at around 430 nm was increasing in intensity when the reaction progresses. This absorption band was broadening towards lower energy, thereby leading to an overall broad absorption, which is typical for a dark brown colored material. This is indeed the case as the microphotographs of the zeolite ZSM-5 crystal during the MTH reaction, as illustrated in Figure 4.4b, showed the gradual darkening of the initially translucent zeolite crystals. First, the zeolite ZSM-5 crystals turned yellow-brown and then gradually obtained a dark-brown color due to the formation of coke (precursor) species, as exemplified by the absorption bands in the spectral region above 450 nm. One could also observe color differences between the crystal core, edges and tips of a reacting zeolite ZSM-5 crystal. As shown in Figure 4.4c, the zeolite crystal darkening stabilized over time, while the crystal edges and the

triangular crystal tips were darkening both more and faster. Focusing the square-shaped NanoSIMS ion beam turned to be rather difficult on the triangular zeolite ZSM-5 crystal tip. Therefore, the middle region of the zeolite ZSM-5 crystals was chosen to prepare the samples for the EPMA and NanoSIMS measurements.

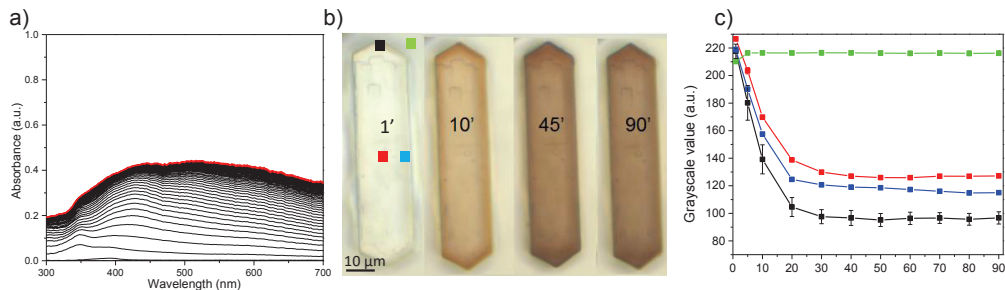


Figure 4.4. a) UV-Vis diffuse reflectance spectra of the zeolite ZSM-5 crystal during the MTH reaction at 350 °C. b) Optical microphotographs of a zeolite ZSM-5 crystal taken during the MTH reaction at 350 °C. The corresponding time is indicated in min. These images were converted into black and white and then corresponding grayscale intensity values for four ROIs that are denoted by black, red, blue, and green squares were counted. c) Grayscale values of the darkening of the zeolite ZSM-5 crystal shown in (b) due to coke formation during Methanol-to-Hydrocarbons (MTH) reaction. The corresponding locations are indicated in (b) that are the crystal tip (■), mid-crystal region (■), edge region (■) and the background (■), respectively. Error bars represent the standard deviation.

4.3.2. Electron Microprobe Analysis

Electron Micro-Probe Analysis (EPMA) was used to map a FIB-made cross-section taken from the middle region of a partially deactivated zeolite ZSM-5 crystal reacted at 350 °C for 90 min. The goal was to determine the spatial distribution of Al, Si and C atoms within a zeolite ZSM-5 crystal. The results are summarized in Figure 4.5a-c. Principal Component Analysis (PCA) and clustering analysis were performed on the EPMA data obtained. This analysis, shown in Figure 4.5d, showed a clear variation in the elemental composition inside the zeolite ZSM-5 crystal under study. EPMA provided the visualization of the Al and C zoning in the outer layers of the zeolite ZSM-5 crystal, with a fairly uniform Si distribution throughout the cross-section. Moreover, we observed a positive correlation between the amount of Al and C atoms. The results are demonstrated in Figure 4.5e-f. Apart from the 2-D mapping of the zeolite cross-section, we also performed lateral-line analyses in order to determine the relative amount of C atoms inside the zeolite ZSM-5 cross-sections. For this reason, a cross-section from another partially deactivated zeolite ZSM-5 crystal (which has been undergoing a MTH reaction at 350 °C for 10 min) was investigated with EPMA. The lateral line measurements were done on both cross-sections, which were reacting for 10 min and 90 min under MTH reaction conditions. Figure 4.6 summarizes the results of these measurements. The cross-sections,

taken from 10 min and 90 min of MTH reaction showed similar coke content in the zeolite ZSM-5 crystal core region. On the other hand, a longer reaction time seemed to produce more coke at the edges of the zeolite crystal cross-section as demonstrated in Figure 4.6c. It is also clear that the coking predominantly took place at the crystal edges. However, EPMA does not provide isotopic elemental information. The carbon signal detected with EPMA shows both reaction species and aforementioned contamination sources.

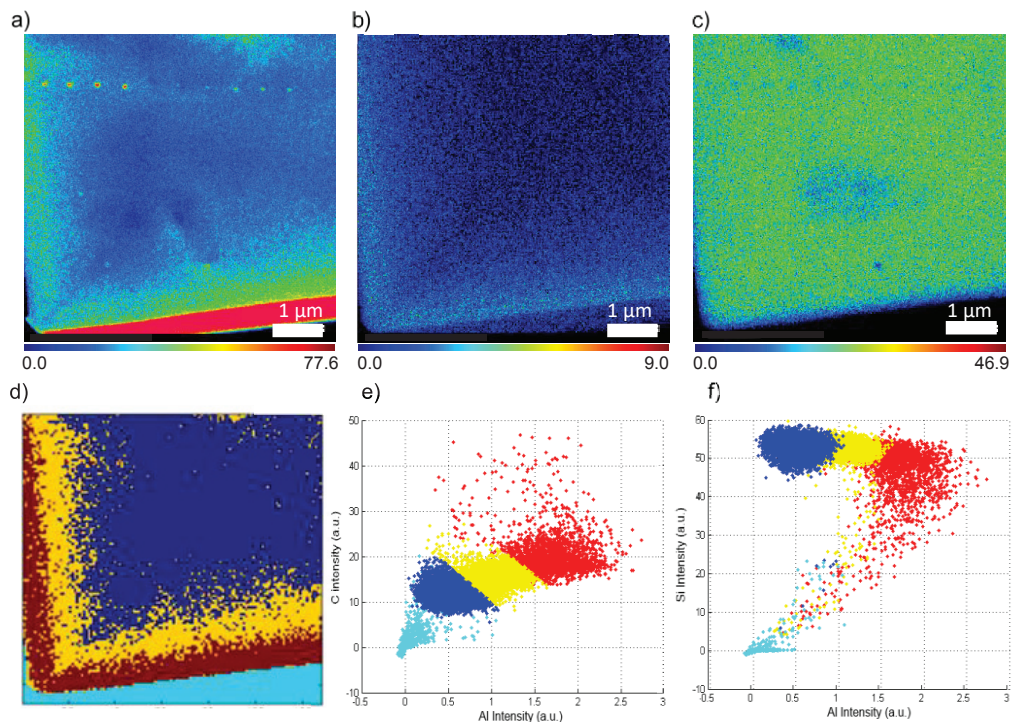


Figure 4.5. a) Carbon b) Al c) Si distribution of a cross-section from a partially deactivated zeolite ZSM-5 crystal reacted at 350 °C for 90 min (Blue spot is due to Gallium insertion during the FIB-reparation and during the EPMA measurement). Color bar scale represent the counts of respective elements. d) PCA clusters same cross-section. e) Si/Al relation, f) C/Al relation of the zeolite ZSM-5 cross-section with the respective clusters shown in (d).

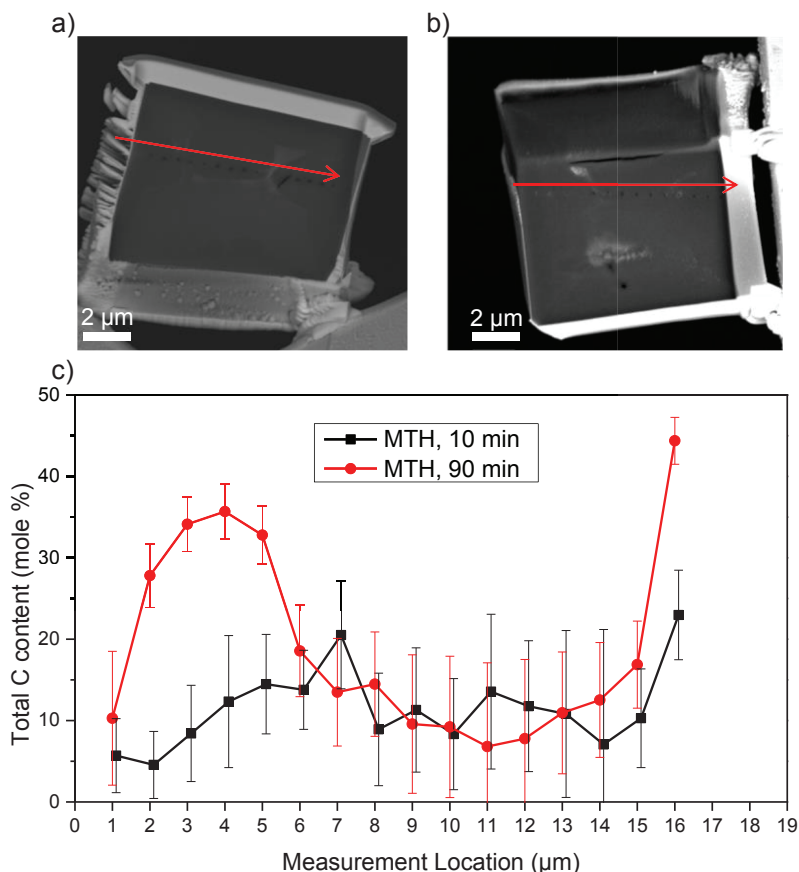


Figure 4.6. SEM image of the analyzed cross-section from a partially deactivated zeolite ZSM-5 crystal after MTH reaction at 350 °C for a) 10 min and b) 90 min. Red arrows on both pictures indicate the direction of the lateral line analysis. c) Lateral distribution of carbon for the two zeolite ZSM-5 cross-sections.

4.3.3. Nano-Secondary Ion Mass Spectrometry

In order to distinguish the differences between the detected carbon signals, we have performed Nano-Secondary Ion Mass Spectrometry (NanoSIMS) measurements that provided isotopic information that was missing in the EPMA measurements. Furthermore, NanoSIMS has a higher elemental resolution than EPMA. Since we have used ^{13}C labeled MeOH as reactant we were able to study the reaction and deactivating hydrocarbon species trapped within the zeolite ZSM-5 crystal. Moreover, we could also obtain detailed information on the spatial distribution of Si and Al atoms within the zeolite ZSM-5 crystals. First, a cross-section taken from the middle of an unreacted zeolite ZSM-5 crystal was performed and the results are shown in Figure 4.7a. It was found that there exists an Al zoning in the

near surface regions of the zeolite ZSM-5 crystal, a finding which is in agreement with the EPMA analyses (Figure 4.7b). In addition, all four of the interfaces of the intergrowth subunits of a zeolite ZSM-5 crystal could be observed. The translucent white dashed cross in Figure 4.7b indicates these interfaces. This finding is in line with the earlier proposed two-component zeolite ZSM-5 crystal model.^[10–12]

Another cross-section that was taken from a partially deactivated zeolite ZSM-5 crystal, which has reacted at 350 °C for 90 min with ¹³C-labeled methanol, was investigated with NanoSIMS at high magnification at one of its corners. The results are shown in Figure 4.7c-f. One can notice the presence of a sub- μm thick Al depleted region, i.e., a silicalite-like zone in the outermost zeolite layer (Figure 4.7d). Below the silicalite layer, one can observe an Al-enriched zone. Furthermore, the amount of Al gradually decreases when moving from the crystal edge to the crystal core. Although the Si/Al ratio of the zeolite ZSM-5 crystals used in this study was reported as 17^[31], the collected NanoSIMS data revealed much higher Si/Al ratios in the measurement spots. NanoSIMS measurements showed the core regions of the zeolite ZSM-5 cross-section had a Si/Al ratio close to 500, as illustrated in Figure 4.7d. The low Al signal is due to the low electron affinity of Al cations with the Cs⁺ primary ion beam used as ion source.^[29] Therefore, absolute quantification of the Al atoms was not possible. On the other hand, the performed NanoSIMS analysis allowed us to visualize the spatial distribution of the Si/Al ratio for a cross-section of the zeolite ZSM-5 crystal, as shown in Figure 4.7e.

In order to separate the contaminant carbon signal from the carbon signal from the reaction and/or deactivating hydrocarbon species, we have normalized the ¹³C signal intensity we have detected to the total carbon signal. In what follows, this ratio will be referred as ¹³C fraction according to Equation. 4.1.

$$^{13}\text{C fraction, \%} = \frac{^{13}\text{C}}{^{13}\text{C} + ^{12}\text{C}} \times 100 \quad (4.1)$$

IUPAC reports the natural abundance of ¹³C as 1.07%.^[32] The observed ¹³C values, which are higher than the natural abundance, indicates that the ¹³C enrichment is from the trapped reaction species inside the zeolite framework structure. Figure 4.7f shows the ¹³C fraction of the quarter cross-section under analysis. The ¹³C fraction increases in the near surface regions of the zeolite ZSM-5 crystal. Furthermore, the diffusion barrier that prevented most probably the coke (precursor) species to migrate through the zeolite subunits can also be revealed. The diffusion barriers formed at the joint locations of the zeolite ZSM-5 crystal

subunits are present in the whole cross-section of the zeolite ZSM-5 crystal and can be observed via ^{13}C fraction mapping. The results are shown in Figure 4.7g.

In the next stage of our study, a lateral line analysis was performed where the pixels within a rectangular area from the outer surface towards the core region of the zeolite ZSM-5 cross-section. The analyzed region is shown in white dashed lines in Figure 4.7d-f. The total carbon, the ^{13}C fraction, as well as the Al and Si distribution in that region of interest were counted. These results are given in Figure 4.8. One could observe an accumulation of the total carbon in the outer region of the zeolite cross-section, where also the Pt/C layer and Si enrichment is located. However, the ^{13}C fraction distribution shows that this enriched total carbon in the zeolite outer layer mostly belongs to ^{12}C species. A sub- μm thick Si shell was followed by a nearly 3 μm thick Al zone, and clearly the relative amounts of ^{13}C and Al correlate and decrease when going from the core to the center of the crystal. In order to obtain a quasi-3-D elemental and isotope distribution throughout the whole zeolite ZSM-5 crystal, another partially deactivated zeolite ZSM-5 crystal was reacted for 90 min at 350 $^{\circ}\text{C}$ in a stream of $^{13}\text{CH}_3\text{OH}$ and this crystal was cut with the FIB method into seven cross-sections. The result of this analysis is shown in Figure 4.9. The SEM image of the cross-sections prepared from this zeolite ZSM-5 crystal is shown in Figure 4.9a. Unlike the previous measurements, the ^{13}C signal from the multi cross-section analyses showed the best contrast upon normalization with the O signal as the possible stress crack formation on the cross-sections caused discrepancies in the ^{12}C signal. Figure 4.9b-c shows the $^{13}\text{C}/\text{O}$ maps of the seven cross-sections taken from this zeolite ZSM-5 crystal.

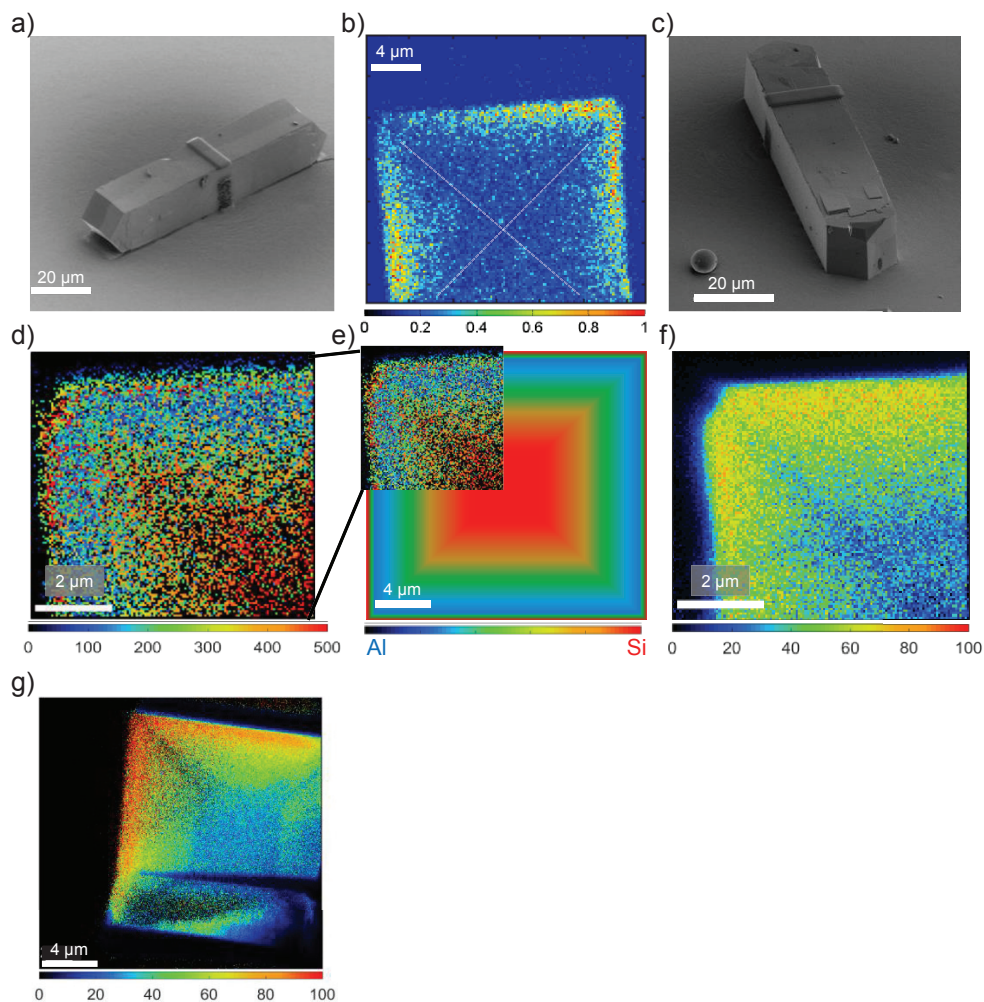


Figure 4.7. a) Protective Pt/C layer applied on top of an a) unreacted zeolite ZSM-5 crystal c) partially deactivated zeolite ZSM-5 crystal reacted for 90 min at 350 °C with $^{13}\text{C}_3\text{H}_7\text{OH}$ where the cross-section was taken. b) NanoSIMS image of the Al distribution of the cross-section, as shown in (a). Dashed white lines indicate the convergence of subunits. d) Si rich (indicated in red) and Al rich (indicated in blue) regions of a corner of a cross-section taken from a coked zeolite ZSM-5 crystal for 90 min at 350 °C in a stream of $^{13}\text{C}_3\text{H}_7\text{OH}$. e) Elemental representation of a zeolite ZSM-5 crystal cross section. Red zones indicate Si, while blue zones indicate Al. f) ^{13}C fraction map of the same cross-section. g) Ratio between the ^{13}C signal and the total C signal of the entire coked zeolite crystal cross-section, shown in Figure 4.9c-e. The horizontal crack-like feature in the lower part of the cross-section is probably a stress crack from the NanoSIMS measurement or FIB-cutting.

It can be observed that each zeolite ZSM-5 crystal cross-section has a ^{13}C accumulation near the crystal edge sites. In addition, the coke distribution revealed the contacts of the interfaces of the intergrowth subunits that act as molecular

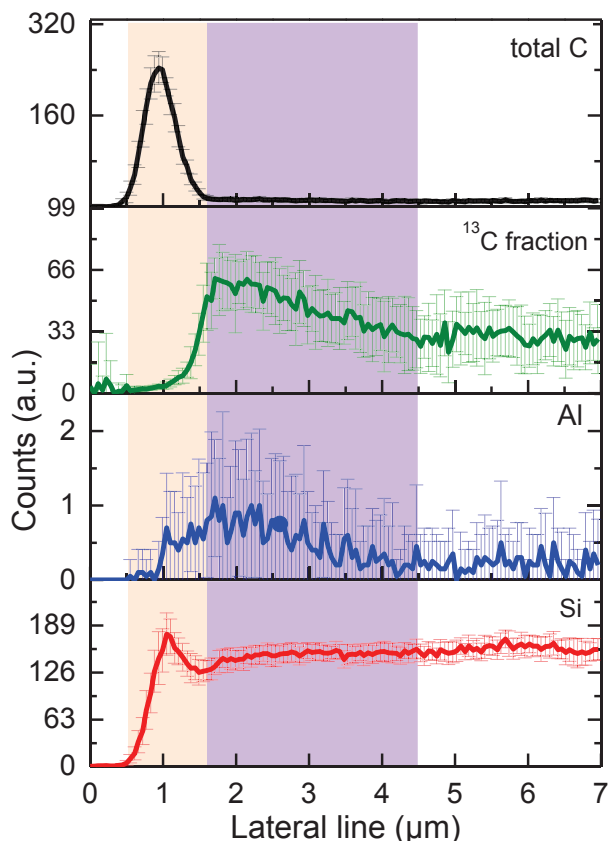


Figure 4.8. The lateral analysis of the total C, ^{13}C fraction, Si, and Al, respectively, for a partially deactivated zeolite ZSM-5 crystal reacted with $^{13}\text{CH}_3\text{OH}$ at 350°C for 90 min. The error bars are representing the Poisson error that shows the theoretical precision of the mean, which is derived from the ion count detected during dwelling time is a random variable with Poisson distribution.^[30]

diffusion barriers. These cross-section analyses with NanoSIMS showed that the MTH process takes place mostly in the outer parts of the zeolite ZSM-5 crystal, where there is an enrichment in Al atoms; hence Brønsted acid sites. Therefore, we have performed sputtering-depth profiling measurements on both parent and various partially deactivated zeolite ZSM-5 crystals, which have been reacting with $^{13}\text{CH}_3\text{OH}$ at 350°C for 10 min, 45 min and 90 min. As shown in Figure 4.10, we have determined the elemental distribution and coke formation on the crystal surface. As explained before, these measurements necessitated a gold layer on the measurement spots for conductivity. With this approach, the first 150 nm from the zeolite crystal surface could be probed. The elemental and isotopic signal disappeared

when the conductive Au layer is completely etched away. The depths of the measurement locations were measured with AFM and FIB-SEM in order to correlate the singular sputter maps to depth. The probed region (~ 150 nm from the external zeolite surface) is the silicalite layer that contains an excess amount of carbon from various contamination sources. However, unlike the cross-section analyses, we did not apply a Pt/C protective layer for the sputtering-depth profiling measurements. Due to this difference in sample preparation, we have detected much less carbon from contamination sources. Figure 4.10a depicts the average of the elemental and isotopic depth profiles of unreacted zeolite ZSM-5 crystals. The Al and Si signals showed that the elemental composition is fairly uniform in the probed volume of the silicalite layer. The ^{13}C fraction was found in unreacted zeolite ZSM-5 crystals to be

~1.15%, which is close to the reported IUPAC value of the ^{13}C fraction in air (1.07%).^[32]

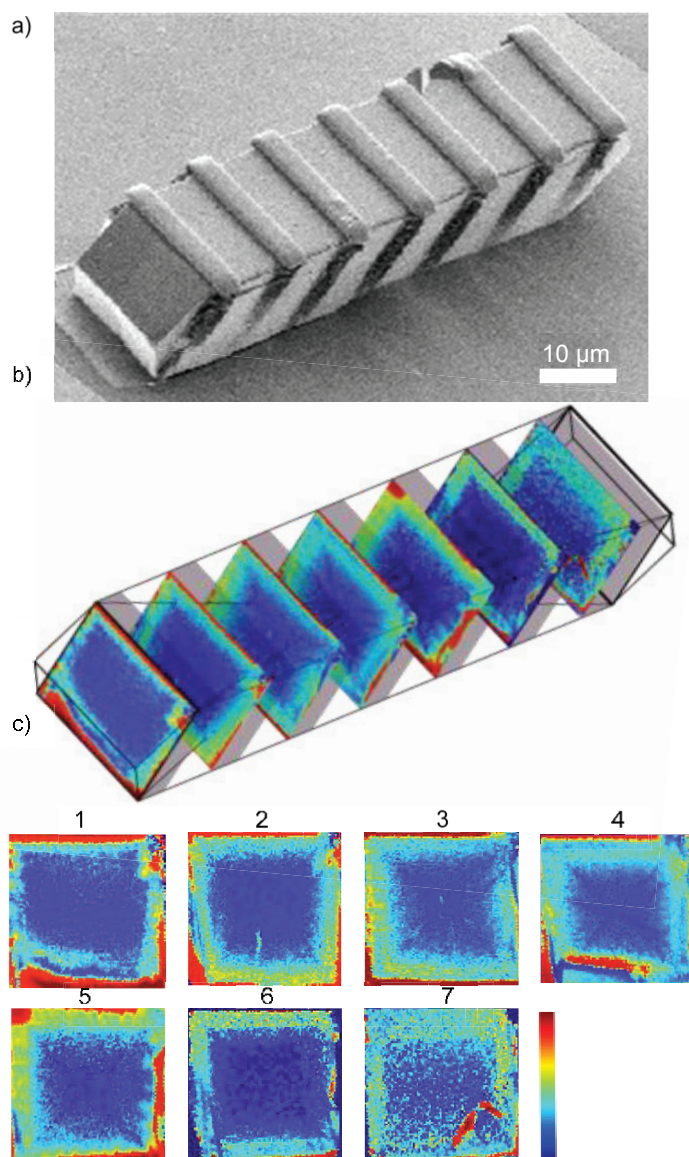


Figure 4.9 a) Cross-sections of a zeolite ZSM-5 crystal which has reacted with $^{13}\text{CH}_3\text{OH}$ at 350 °C for 90 min and then prepared by FIB-cutting. A Pt/C protective layer was applied to 7 different locations on the cross-section. b) The $^{13}\text{C}/\text{O}$ distribution of each cross-section from the first to the last. c) Cross-section isotopic carbon maps for this $^{13}\text{CH}_3\text{OH}$ reacted zeolite ZSM-5 crystal at 350 °C for 90 min.

Figure 4.10b shows the influence of the reaction time on the formation of coke (precursor) species in a 150 nm outer surface region of a zeolite ZSM-5 crystal reacting with ^{13}C -labeled methanol at 350 °C. The sputter depth profiling of the partially deactivated zeolite ZSM-5 crystals showed a stable, 10% ^{13}C fraction after 10 min of MTH reaction. When the reaction time increased to 45 min, the zeolite surface seemed to contain less coke (precursor) species than in the inner regions of the zeolite material, which indicates that there already some Al atoms (hence Brønsted acid sites) are present to perform the MTH reaction. Evidence from this comes from the Si signal intensity, which decreases after ~50 nm, as shown in Figure 4.10a. Another explanation is that the formation of coke (precursor) species mainly took place in the deeper Al-rich region of the zeolite crystal; and was moving towards the outer surface of the crystal. Interestingly, a longer reaction of 90 min caused an increased and rather stable coke formation of ~50%, which was rather equally distributed within the first 150 nm of the zeolite crystal.

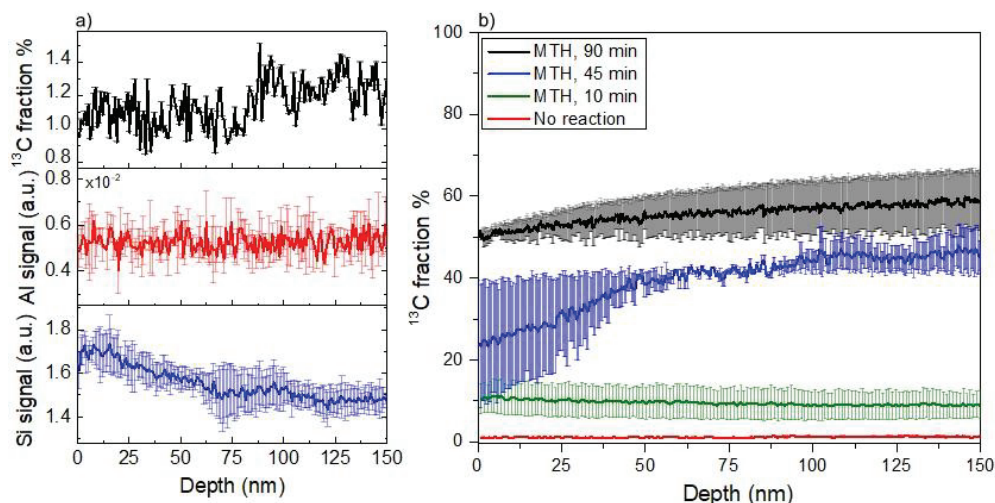


Figure 4.10. a) Normalized Si and Al signal intensity as well as the ^{13}C fraction of an unreacted zeolite ZSM-5 crystal within the first 150 nm from the zeolite crystal surface b) ^{13}C fraction comparison of the unreacted and partially deactivated zeolite ZSM-5 crystals reacted at 350 °C for three different reaction time of 10 min, 45 min and 90 min. Error bars represent the standard deviation from the mean of various datasets from similar reaction conditions.

4.4. Conclusions

The application of operando UV-Vis diffuse reflectance micro-spectroscopy and advanced microprobe techniques, namely EPMA and NanoSIMS, provided new details on the spatial distribution of both Si and Al within large zeolite ZSM-5 crystals as well as on the formation of coke (precursor) species during the MTH process.

Sputter-depth profiling and cross-section analyses of the zeolite ZSM-5 crystals elucidated the crystal architecture where an outermost silicalite layer (~100-200 nm thick) is followed by a gradually decreasing aluminium-rich zone (~2-5 μm thick). The microprobe techniques used revealed a direct relationship between the formation of hydrocarbons and the Al sites (Brønsted acid sites) within the zeolite ZSM-5 crystals. Furthermore, it could visualize the boundaries between the subunits of the large zeolite ZSM-5 crystals. These methods also allowed monitoring the formation of coke (precursor) species within a zeolite ZSM-5 crystal during the MTH process. It was found that this catalyst deactivation is a self-stopping process, as schematically shown in Figure 4.11. Coke build-up was observed mainly in the near surface sites of zeolite ZSM-5 crystals. We suggest a pathway explaining the initial formation of coke species and their evolution that leads to catalyst deactivation. Methanol initially adsorbs at the catalyst surface and immediately starts the (by-) product formation in the silicalite-rich layer where less Brønsted acid sites are present. The desired reaction products as well as coke (precursor) species start forming near the Al sites. Upon further methanol exposure, coke (precursor) species enlarge in size and further diffuse towards the zeolite crystal core. The migration of reaction (by-)products is hindered at the intergrown subunit edges, which are 90° oriented with their neighboring intergrowth components. On the other hand, due to fewer spatial constraints on the zeolite outer surface, coke (precursor) species diffusing outwards, cause surface coverage and enlarge further in size to form graphite-like molecules. This accumulative evolution of coke (precursor) species limits the intracrystalline diffusion properties. While the MTH reaction proceeds, the surface coverage by hydrocarbon deposits increases, and severe diffusion limitations cause the coke (precursor) species to pile up inside the subunits and on the outer surface of the zeolite crystal, which eventually leads to catalyst deactivation.

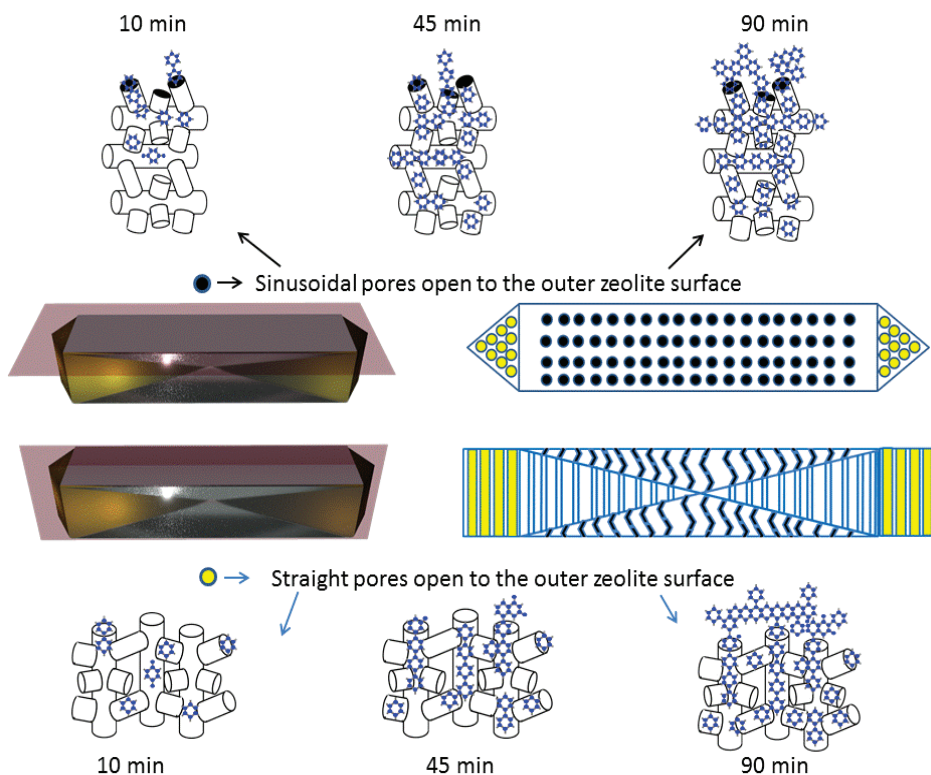


Figure 4.11. a) Surface coverage of coke species formed during the Methanol-to-Hydrocarbons (MTH) process within the sinusoidal pore system, which is open to the outer zeolite surface in the rectangular area of the top surface. b) Schematics of a zeolite ZSM-5 crystal indicating the zeolite crystal surface and the representation of pore orientations on the crystal surface, respectively. c) Schematics indicating the zeolite crystal center and the representation of the pore orientations within the crystal center. d) Surface coverage of coke species formed during the MTH process on the on the straight pore system, which is open to surface in the triangular areas on the crystal top surface.

4.5. Acknowledgments

Machteld Martens (ExxonMobil, Belgium) is acknowledged for providing the large zeolite ZSM-5 crystals. The author thanks Donglong Fu, Abhishek Dutta Chowdhury and Joel Schmidt, all from Utrecht University, for fruitful discussions.

4.6. Contributions

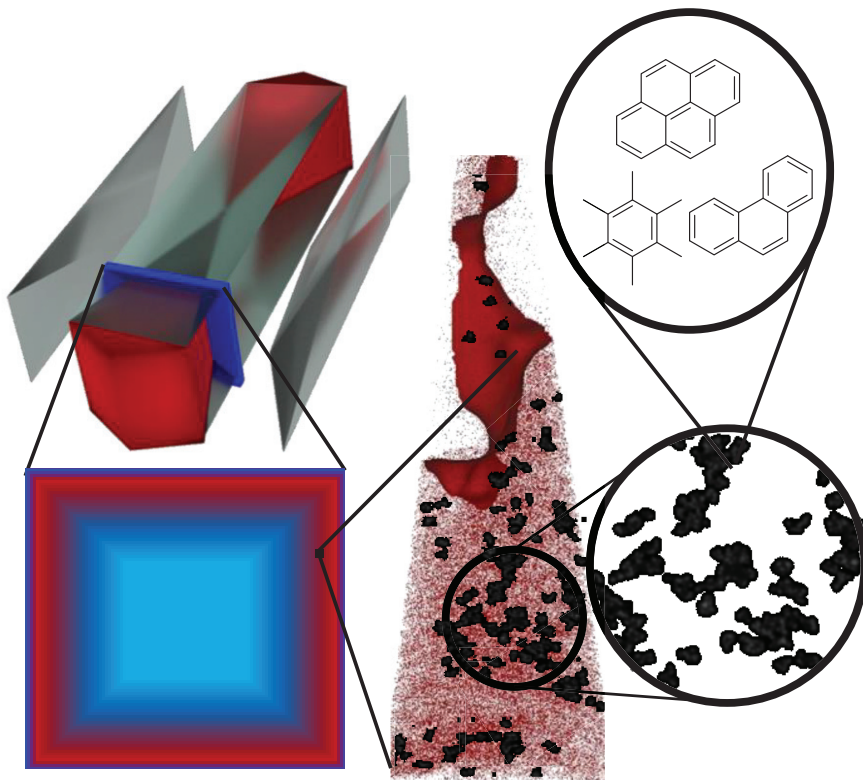
Özgün Attila conceived, together with Bert Weckhuysen (Utrecht University, UU), the research plan. Özgün Attila has performed the MTH reactions, prepared the zeolite samples and performed the experiments. The data analysis was done by Özgün Attila and Florian Meirer (UU). Data interpretation was done by Özgün Attila, Florian

Meier and Bert Weckhuysen (UU). Bert Weckhuysen has made revisions and corrections to the chapter.

References

- [1] International Energy Agency, *World Energy Outlook- Spec. Rep.* **2016**, 266.
- [2] S. Chu, A. Majumdar, *Nature* **2012**, *488*, 294–303.
- [3] S. Svelle, U. Olsbye, F. Joensen, M. Bjørgen, *J. Phys. Chem. C* **2007**, *111*, 17981–17984.
- [4] C. D. Chang, W. H. Lang, R. L. Smith, *J. Catal.* **1979**, *56*, 169–173.
- [5] K. Klier, *Adv. Catal.* **1982**, *31*, 243–313.
- [6] E. G. Derouane, J. G. Fripiat, *Zeolites* **1985**, *5*, 165–172.
- [7] R. J. Argauer, G. R. Landolt, *US Patent 3702886*, **1972**, 3702886.
- [8] G. A. Olah, *Angew. Chem. Int. Ed.* **2013**, *52*, 104–107.
- [9] G. A. Olah, A. Goepfert, G. K. S. Prakash, *Beyond Oil and Gas: The Methanol Economy: Second Edition*, Wiley-VCH, Weinheim, **2009**.
- [10] G. D. Price, J. J. Pluth, J. V. Smith, J. M. Bennett, R. L. Patton, *J. Am. Chem. Soc.* **1982**, *104*, 5971–5977.
- [11] E. Stavitski, M. R. Drury, D. A. M. De Winter, M. H. F. Kox, B. M. Weckhuysen, *Angew. Chem. Int. Ed.* **2008**, *47*, 5637–5640.
- [12] L. Karwacki, M. H. F. Kox, D. A. M. de Winter, M. R. Drury, J. D. Meeldijk, E. Stavitski, W. Schmidt, M. Mertens, P. Cubillas, N. John, A. Chan, N. Kahn, S. R. Bare, M. Anderson, J. Kornatowski, B. M. Weckhuysen., *Nat. Mater.* **2009**, *8*, 959–965.
- [13] D. Mores, E. Stavitski, M. H. F. Kox, J. Kornatowski, U. Olsbye, B. M. Weckhuysen, *Chem. Eur. J.* **2008**, *14*, 11320–11327.
- [14] M. H. F. Kox, E. Stavitski, J. C. Groen, J. Pérez-Ramírez, F. Kapteijn, B. M. Weckhuysen, *Chem. Eur. J.* **2008**, *14*, 1718–1725.
- [15] C. Sprung, B. M. Weckhuysen, *Chem. Eur. J.* **2014**, *20*, 3667–3677.
- [16] L. R. Aramburo, L. Karwacki, P. Cubillas, S. Asahina, D. A. M. De Winter, M. R. Drury, I. L. C. Buurmans, E. Stavitski, D. Mores, M. Daturi, P. Bazin, P. Dumas, F. Thibault-Starzyk, J. A. Post, M. W. Anderson, O. Terasaki, B. M. Weckhuysen, *Chem. Eur. J.* **2011**, *17*, 13773–13781.
- [17] Z. Ristanović, J. P. Hofmann, U. Deka, T. U. Schüllli, M. Rohnke, A. M. Beale, B. M. Weckhuysen, *Angew. Chem. Int. Ed.* **2013**, *52*, 13382–13386.
- [18] R. von Ballmoos, W. M. Meier, *Nature* **1981**, *289*, 782–783.
- [19] E. G. Derouane, S. Determerie, Z. Gabelica, N. Blom, *Appl. Catal.* **1981**, *1*, 201–224.
- [20] R. Althoff, B. Schulz-Dobrick, F. Schüth, K. Unger, *Microporous Mater.* **1993**, *1*, 207–218.

- [21] J. B. Nagy, P. Bodart, H. Collette, J. El Hage-Al Asswad, Z. Gabelica, R. Aiello, A. Nastro, C. Pellegrino, *Zeolites* **1988**, *8*, 209–220.
- [22] G. Debras, A. Gourgue, J. B. Nagy, G. De Clippeleir, *Zeolites* **1985**, *5*, 369–376.
- [23] N. Danilina, F. Krumeich, S. A. Castelanelli, J. A. Van Bokhoven, *J. Phys. Chem. C* **2010**, *114*, 6640–6645.
- [24] M. R. Kilburn, D. Wacey, in *Princ. Pract. Anal. Tech. Geosci.*, Royal Society of Chemistry, Cambridge, **2015**, 1–34.
- [25] J. P. Hofmann, D. Mores, L. R. Aramburo, S. Teketel, M. Rohnke, J. Janek, U. Olsbye, B. M. Weckhuysen, *Chem. Eur. J.* **2013**, *19*, 8533–8542.
- [26] M. Wagner, *Annu. Rev. Microbiol.* **2009**, *63*, 411–429.
- [27] C. Lechene, F. Hillion, G. McMahon, D. Benson, A. M. Kleinfeld, J. P. Kampf, D. Distel, Y. Luyten, J. Bonventre, D. Hentschel, K. M. Park, S. Ito, M. Schwartz, G. Benichou, G. Slodzian, *J. Biol.* **2006**, *5*, 1–30.
- [28] P. Hoppe, S. Cohen, A. Meibom, *Geostand. Geoanalytical Res.* **2013**, *37*, 111–154.
- [29] P. Philipp, T. Wirtz, H. N. Migeon, H. Scherrer, *Appl. Surf. Sci.* **2006**, *252*, 7205–7207.
- [30] L. Polerecky, B. Adam, J. Milucka, N. Musat, T. Vagner, M. M. M. Kuypers, *Environ. Microbiol.* **2012**, *14*, 1009–1023.
- [31] E. Stavitski, M. H. F. Kox, B. M. Weckhuysen, *Chem. Eur. J.* **2007**, *13*, 7057–7065.
- [32] J. R. de Laeter, J. K. Böhlke, P. De Bièvre, H. Hidaka, H. S. Peiser, K. J. R. Rosman, P. D. P. Taylor, *Pure Appl. Chem.* **2003**, *75*, 683–800.



CHAPTER

V

Coke Formation in Large Zeolite ZSM-5 Crystals during the Methanol-to-Hydrocarbons Process as Studied with Atom Probe Tomography

Coke formation is most likely the main deactivation pathway for zeolite-based catalysts used in Methanol-to-Hydrocarbons (MTH) processes. Therefore, understanding the coke formation is vital for improving these catalysts to design superior catalyst materials. In this Chapter, Atom Probe Tomography (APT) was used to resolve the zeolite composition in 3-D with atomic resolution. This first of its kind study revealed agglomerated coke formation from tens of nm to atomic clusters containing 30-60 C atoms. Furthermore, the presence of carbon clusters could correlate with existence of Brønsted acid sites. This sub-nanoscale correlation shows the importance of careful material design to prevent detrimental coke formation.

*This chapter is based on the following paper: Coke Formation in a Zeolite Crystal During the Methanol-to-Hydrocarbons Reaction as Studied with Atom Probe Tomography, J. E. Schmidt, J. D. Poplawsky, B. Mazumder, Ö. Attila, D. Fu, D. A. M. de Winter, F. Meirer, S. R. Bare, B. M. Weckhuysen, *Angew. Chem. Int. Ed.* **2016**, *55*, 11173–11177.

5.1. Introduction

The elucidation of proper structure-property relationships for heterogeneous catalysts necessitates their in-depth physicochemical characterization across a wide variety of length scales. For zeolite-based catalysts, this characterization approach includes the entire range from sub-nanometers to tens of meters, which is the scale of industrial reactors in which these materials are used, most often in the form of shaped catalyst bodies.^[1,2] Numerous studies have provided valuable insights on structure-property relationships at various length scales.^[3-9] Some of these techniques, such as X-Ray Diffraction (XRD) and Nuclear Magnetic Resonance (NMR), are capable of providing sub-nm characterizations of the bulk, the ensemble average of solid catalysts. In previous Chapters, we have performed the (sub)micron- and nano-scale characterization studies on single zeolite ZSM-5 crystals. This has been done via the combination of a variety of spectroscopy and microscopy techniques. This approach provided valuable insights on the elemental distribution, and on the zoning of Al and Si within large zeolite ZSM-5 crystals. We also have obtained information on the formation of coke (precursor) species, and determined their molecular structure, which can range from poly-methylated polyaromatics to rather complex graphite-like carbon species. However, neither vibrational, electronic and X-ray spectroscopy or microscopy, nor ion mass spectrometry, could provide the required sub-nm level information.

The only capable method so far that can probe sub-nm scale chemical information in 3-D is Atom Probe Tomography (APT). It provides elemental distributions with near-atomic scale via creating 3-D elemental reconstructions. APT was proposed for the first time in the 1930s, but even by the mid-1940s researchers could not surpass the 2 nm-resolution barrier.^[10] In 1955 Bahadur and Müller could resolve individual atoms of a tungsten specimen (Figure 5.1a) with a Field Ion Microscope (FIM), as shown in Figure 5.1b.^[11] This was the first time humans literally saw atoms after they were postulated by Leucippus and Democritus more than 2 millennia ago.^[10] The identification of different single atoms was first reported in 1967 by a group of scientists at Pennsylvania State University by the invention of Atom Probe to detect atomic species for alloy research.^[12] To make this possible, the sample is required to be sculpted into a needle-shaped specimen using Focused Ion Beam (FIB). After this treatment, the sample is inserted into a cryogenic stage under Ultra-High Vacuum (UHV) conditions. An electric field (in the order of ~ 10 V/nm) is applied between the sample and the local electrode causing atoms to evaporate as ions. Using the fast laser and/or voltage pulses, one or several ions are evaporated. The time between the start of the event and their detection provide the chemical

identity of ions (with the aid of a time-of-flight mass spectrometer). The ions then are spatially detected on a 2-D position detector. This is schematically shown in Figure 5.1d. A photograph of a modern APT instrument, namely the LEAP 4000 machine, is included in Figure 5.1e.

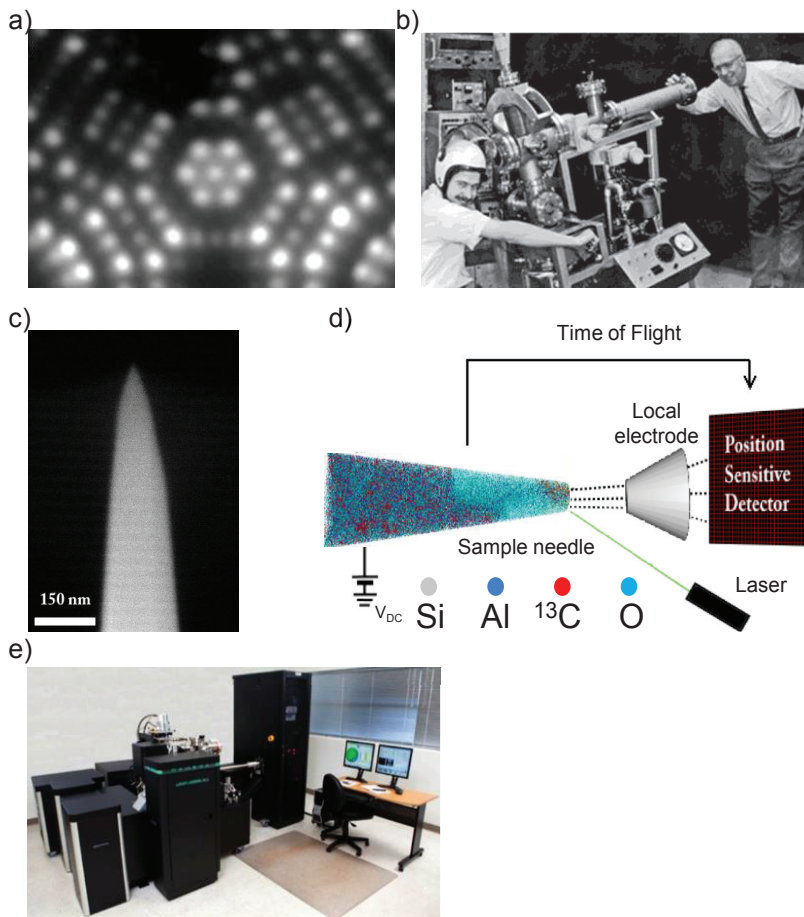


Figure 5.1 a) One of Müller's original FIM images of a W(111) field ion microphotograph showing individual atoms b) John Panitz (left), Erwin Müller (right) and the first all-metal probe Field Ion Microscope (FIM). Photo courtesy of J.A. Panitz. c) Needle-shaped zeolite specimen prepared by Focused Ion Beam (FIB) milling. d) A schematic of the Atom Probe Tomography (APT) instrument with needle-shaped specimen showing Al, O, Si and ^{13}C within a zeolite ZSM-5 needle. e) Modern-day LEAP 4000 APT instrument.^[10]

Although the APT technique was developed to study metal alloys in great depth, which are conductive materials, advancing technology brought us

femtosecond lasers, which allowed the application of APT on non-conductive materials. The first APT study applied to zeolites, which are non-conductive materials have been performed by Perea et al. in 2015.^[13] This study, a cooperation between Pacific Northwest National Laboratory and our group, revealed a non-uniform Al distribution in both parent and steamed large zeolite ZSM-5 crystals, furthermore showing Al atoms mobility during steaming, whereby Al atoms are concentrated in specific places within the zeolite crystal (i.e., Al zoning could be visualized). A recent review from our group, highlighting new insights gained on zeolites via APT method is published recently.^[14]

As explained in Chapter 1, coke formation during hydrocarbon conversion processes, including the Methanol-to-Hydrocarbons (MTH) reaction, is detrimental and cause deactivation of zeolite-based catalysts. The formation of carbonaceous species (that are e.g. mono- and polycyclic poly-methylated aromatics), which become trapped in the zeolite framework especially in the near surface regions of the zeolite crystals was reported to lower the mass transfer properties.^[7,9,15–17] In order to fully understand the mechanism of the coke formation in the early stages of the MTH process on a zeolite ZSM-5 crystal, it is crucial to study these coke deposits at high spatial resolution. The spatial coke distribution near Brønsted acid sites, i.e., the Al atoms of the zeolite framework, was shown at the nanoscale in Chapter 4 using the technique of NanoSIMS. In this Chapter, we report the first APT study on a coked zeolite ZSM-5 crystal, in which we simultaneously measure carbon and aluminium atoms. As a result, we obtained the 3-D spatial distribution of carbon clusters and correlated their formation to zeolite Al atoms at sub-nm resolution. These measurements provide new insights into the deactivation process of zeolite ZSM-5 crystals during MTH.

5.2. Experimental Section

5.2.1 Materials

Large zeolite ZSM-5 crystals with an average size of $100 \times 20 \times 20 \mu\text{m}^3$ (bulk Si/Al = 17) were provided by Exxon-Mobil (Machelen, Belgium) in their sodium form. The starting chemicals for the synthesis of these zeolite ZSM-5 crystals were: Ludox AS40 (Sigma-Aldrich, 40 wt% in H_2O), tetrapropylammonium bromide (TPABr, Fluka, $\geq 98\%$), $\text{Al}_2(\text{SO}_4)_3 \cdot 18\text{H}_2\text{O}$ (Baker, 98%), and NH_4OH (VWR, 29%). The molar composition of the synthesis gel was $6.65 (\text{NH}_4)_2\text{O}/0.67 \text{TPA}_2\text{O}/0.025 \text{Al}_2\text{O}_3/10 \text{SiO}_2/121 \text{H}_2\text{O}$. Their synthesis procedure has been reported elsewhere.^[18] The as-synthesized samples were first calcined at $500 \text{ }^\circ\text{C}$ for 12 h in air to remove the template in a flow oven. Subsequently, a triple ion exchange with a 10 wt% ammonium nitrate (Acros Organics, 99+%) solution at $60 \text{ }^\circ\text{C}$ was performed. After

the repetition of the calcination step, the parent zeolite ZSM-5 crystals were obtained.

Methanol-to-Hydrocarbons (MTH) conversion reactions were performed in an in-situ reaction cell equipped with a quartz window for light microscopy (THMS 600, Linkam Scientific Instruments) with a temperature controller (Linkam TMS94). Large zeolite crystals were placed on quartz plates in the in-situ reaction cell and subsequently heated to 120 °C (5 °C.min⁻¹ for 30 min) under O₂ flow of 20 ml.min⁻¹ as the initial calcination step before reaction. Then, the temperature was increased to 550 °C (5 °C.min⁻¹) for 60 min. This method cleared all possible adsorbents from the zeolite crystal. Upon completion of the calcination process, the temperature was decreased to the reaction temperature of 350 °C under 20 ml.min⁻¹ N₂ flow, and methanol was introduced into the cell as a reactant. MTH was performed using ¹³C labeled methanol (Sigma Aldrich, 99 at.%) to distinguish the reaction species from the residual carbon and adsorbents. A reaction time of 90 min was carefully chosen to ensure the zeolite crystals had sufficient occluded coke species for APT analysis, but were not yet deactivated, as demonstrated in our previous work using this material.^[7]

5.2.2 Sample Preparation and Measurements

After performing the MTH process, the zeolite crystals were taken out for FIB-milling. Various cross-sections were prepared for APT analysis as shown in Figure 5.2a. We have chosen a single cross-section amongst them that is closest to the crystal tip where 5 out of 6 pyramidal sub-units that form the zeolite crystal were expected to be visible (Figure 5.2b). Samples were prepared in needle shapes using standard APT sample preparation methods utilizing micro-tip arrays that are purchased from CAMECA.^[19] The location of the samples for the APT measurements was chosen in the near-surface regions and at the middle of the zeolite crystal cross-sections in order to observe the ¹³C and Al distribution variations inside the crystal. Figure 5.2c shows the Si/Al distribution (as measured with NanoSIMS) of a zeolite ZSM-5 crystal cross-section. The location of the four needles taken out from the sample is indicated in Figure 5.2c-d. Figure 5.2e-h displays the FIB-milling process of the zeolite rod. Eleven needles were prepared via this method from the same cross-section. However, only four of them produced successful APT data as the material easily fractures and data collection failures were encountered. The observed material fracture is due to the nature of the zeolite samples analyzed, mainly due to their low-conductivity. Coked zeolites contain a mixture of organic and inorganic species. In order to collect the ions from the zeolite framework, a higher current has to be used, which caused the occluded organic deposits to explode and hence crack the needle-shaped specimen. The prepared APT needles were

transferred to the LEAP 4000XR local electrode atom probe instrument of CAMECA. The samples were run in laser pulse mode ($E_{\text{laser}}=200$ pJ, $T_{\text{base}}=40$ K, $f_{\text{pulse}}=200$ kHz, Detection rate: 1 atom per 200 pulses). The detector had $\sim 37\%$ efficiency.

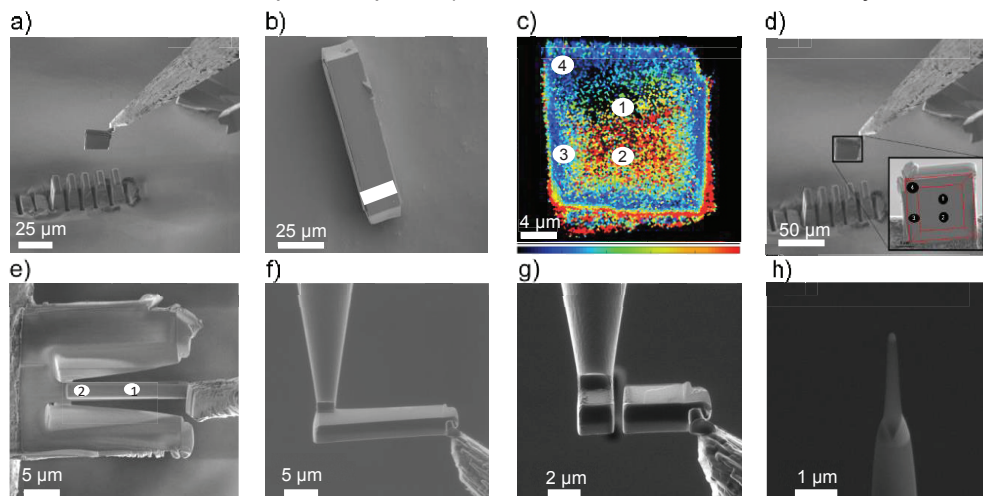


Figure 5.2. a) Variety of cross-sections that were removed for the Atom Probe Tomography (APT) needle preparation. b) Location of the cross-section taken from the zeolite ZSM-5 crystal indicated in the region. c) NanoSIMS measurement of the cross-section showing the Si/Al ratio. Locations of the four needles analyzed with APT are indicated. d) The red dashed lines show the locations of the subunits and the black numbered circles indicate the needle locations on the cross-section analyzed. e) Zeolite rods are prepared by further FIB-milling. Location of the needles 1 and 2 are indicated by the white circles. f) The zeolite rod is attached to a Si needle for further milling. g) Further FIB-milling of the zeolite rod and h) As-prepared zeolite needle.

5.2.3 Data Analysis

The terms used in the following section will be consistent with the APT terminology. ‘*Bulk*’ will refer to the entire needle-shaped sample, while the term ‘*matrix*’ will refer to the leftover atoms after the clustered atoms are taken out from the analyzed volume. ‘*Solute*’ will refer to the elements of interest in the analyzed data.^[10,19] The complexity of the data analysis comes from the non-conductive nature of the zeolite materials under study as well as from the assignments in the mass spectra due to the variety of the hydrocarbon products formed during the MTH process. Sample heating, as it is a part of the data collection process, created thermal tails which cause interference in the mass spectrometry peaks. Adding the complexity of the formed MTH (by-)products to the thermal tail issue, not all the collected datasets gave reliable quantitative results. Another potential problem observed in the collected data was the too high Si/Al ratio found in the needles relative to the reported Si/Al value of 17, as determined with other characterization

methods.^[20] This can be - at least in part - explained by the location of the prepared APT needles. Considering the total zeolite crystal volume ($100 \times 20 \times 20 \mu\text{m}^3$), the APT needles prepared were infinitesimally small. In addition, due to the heterogeneous elemental distribution of the zeolite ZSM-5 crystals under study, they could be chosen from the regions having higher Si/Al ratios. Also, similar to the mass detection problems of Al atoms, observed in the NanoSIMS study (Chapter 4), the detection of Al atoms by the APT detectors could be low. A similar phenomenon was reported for boron detection in previous APT studies.^[10]

Isosurface Analysis (ISA) is a common method in APT research. Initially, a 3-D grid in the concentration space - where the points contain equal elemental composition - is created. Connecting these points with each other provide 3-D surfaces. These surfaces reveal the internal features in the 3-D dataset so that they can be identified and separated. Delocalization and voxel size are defined by the user to create the 3-D voxels. There is a trade-off between the voxel size and the noise. Smaller voxels give a higher spatial resolution, but they create a greater amount of noise.^[10] A *Cluster Analysis* (CA) is used for identifying regions where the solute atoms are closer to each other than the bulk data to effectively determine locally enriched regions that are too small to be identified using the isosurface analysis.^[10] The CA consists of choosing a minimum number of solute atoms that may form a cluster (N_{\min}). The distance between two possible atoms that may form a cluster is defined as D_{\max} . So that, the N_{\min} amount of same atoms that are D_{\max} away from each other form a cluster. With iteration between N_{\min} and D_{\max} , optimal values can be determined where significant clusters can be revealed via comparison to the randomized distribution. Another method used for cluster identification is the *Nearest Neighbor Distribution* (NND) method in which the next neighboring atom of the solute and the randomized dataset are compared.^[19] By this method, the atom pair distance distributions can be obtained. In the randomized dataset, this approach shows a normal distribution. If clustering is present in the real dataset, solute NNDs will be smaller than the random dataset. Then at least two Gaussians would be needed to represent the dataset, one for describing the normal distribution, one for the clusters. Statistically, the deviations from the random dataset can be evaluated via the Frequency Distribution Analysis (FDA)^[21] that is done by the IVASTM software from CAMECA. Finally, the *Radial Distribution Function* (RDF) is used for analyzing the homogeneity of the atoms forming clusters.^[22,23] The analysis is done by the normalization of the local concentration of the selected ion in the bulk and it is conducted radially outward from the center of the clusters, which allows the revelation of the compositional variances within clusters. The approach is illustrated in Figure 5.3. The error of these calculations is based on counting statistics. Since few ions are counted near the cluster center, higher error bars are calculated in these regions.

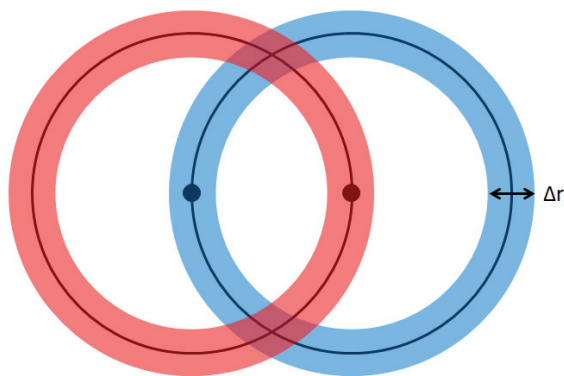


Figure 5.3. 2-D schematic of the Radial Distribution Function (RDF) for analyzing the spatial distribution of different elements in the Atom Probe Tomography (APT) data.

5.3 Results and Discussion

As illustrated in Figure 5.2, four specimens were taken from the same zeolite ZSM-5 cross-section and successfully analyzed with APT. The aim was to study the chemical composition differences in the different subunits of the large zeolite ZSM-5 crystal. Figure 5.4 shows the measured bulk Si/Al ratio as well as the coke content for each needle taken from the cross-section from a partially deactivated zeolite ZSM-5 crystal. The complete compositions were determined for each APT needle as demonstrated in Table 5.1. Between the amount of bulk Si/Al ratio (which determines the Brønsted acid sites) and the ^{13}C (that is a direct indicator of coke species), there is a strong correlation. In addition, there is also another correlation with the location of the APT needle for both Si/Al ratio and coke content. APT needles 1 and 2 which are taken from the center from a cross-section of a zeolite ZSM-5 crystal had less Al and ^{13}C content. In comparison, the APT needles taken from the edge regions of the cross-section had elevated amount of Al and ^{13}C . The small amount of material measured in APT needles that are in order of cubic nanometers makes these correlations even more valuable. Even the APT needles taken from the same location in microscale (see the locations and the Al composition in Table 5.1), had different atomic compositions. The carbon concentrations are consistent with the expected trend as they are highest near the crystal surface sites and decrease towards the center of the crystal.

Reconstructions of all the four needles are shown in Figure 5.5, including the 3-D distributions of the Al, O, Si and ^{13}C atoms in these materials. It is clear that, APT needles 2 and 3 reveal obvious chemical heterogeneities within the samples. It is crucial to emphasize that the size of the analyzed needles were orders of

magnitude smaller than the crystal size of zeolite ZSM-5. ISA was used for identification of these chemical heterogeneities in APT needles 2 and 3.

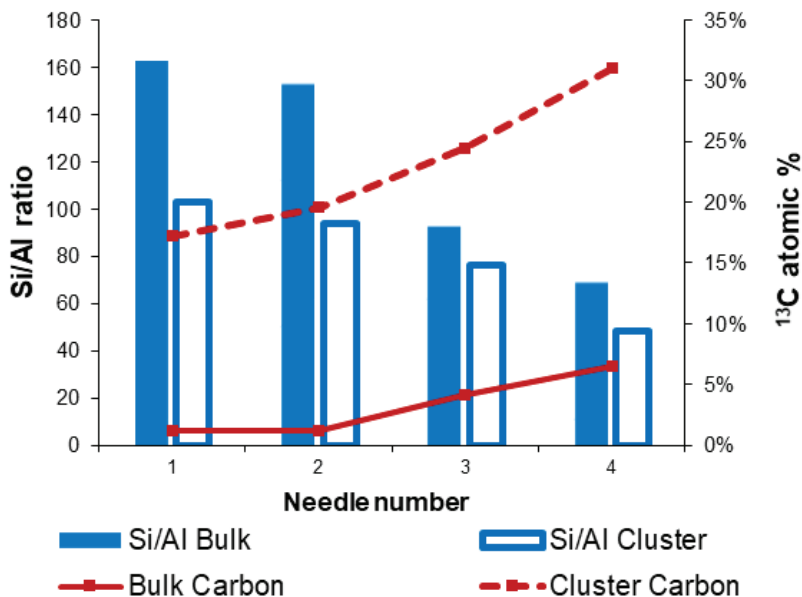


Figure 5.4. Brønsted acid site density (Si/Al) and coke (^{13}C) content of the bulk and detected clusters in all the APT needles measured for the zeolite ZSM-5 crystal which has been MTH reacted for 90 min at 350 °C with ^{13}C labeled methanol.

Table 5.1. Bulk compositions of the reconstructed APT needles for a zeolite ZSM-5 crystal reacted with ^{13}C labeled methanol at 350 °C for 90 min.

Needle	Location	Total matrix atoms	Atomic Composition (%)					Si/Al
			Al	O	Ga ^a	Si	^{13}C	
1	Center	6,114,465	0.22%	62.9%	0.1%	35.6%	1.2%	162.7
2	Center	6,164,300	0.22%	62.7%	0.1%	35.7%	1.2%	152.8
3	Edge	3,580,801	0.36%	61.7%	0.1%	33.6%	4.2%	93.0
4	Edge	1,071,376	0.46%	60.2%	0.7%	32.2%	6.5%	69.0

^aGallium is present from the FIB procedure

Figure 5.6 indicates the detected ^{13}C boundaries in the APT needles 2 and 3 as 0.5% and 3%, respectively. The abrupt change of the ^{13}C concentration with respect to the distance from the isosurface, as illustrated in Figure 5.6c-d, cannot be related directly to variations in Brønsted acidity as the observed changes in Si/Al ratio are not that significant.

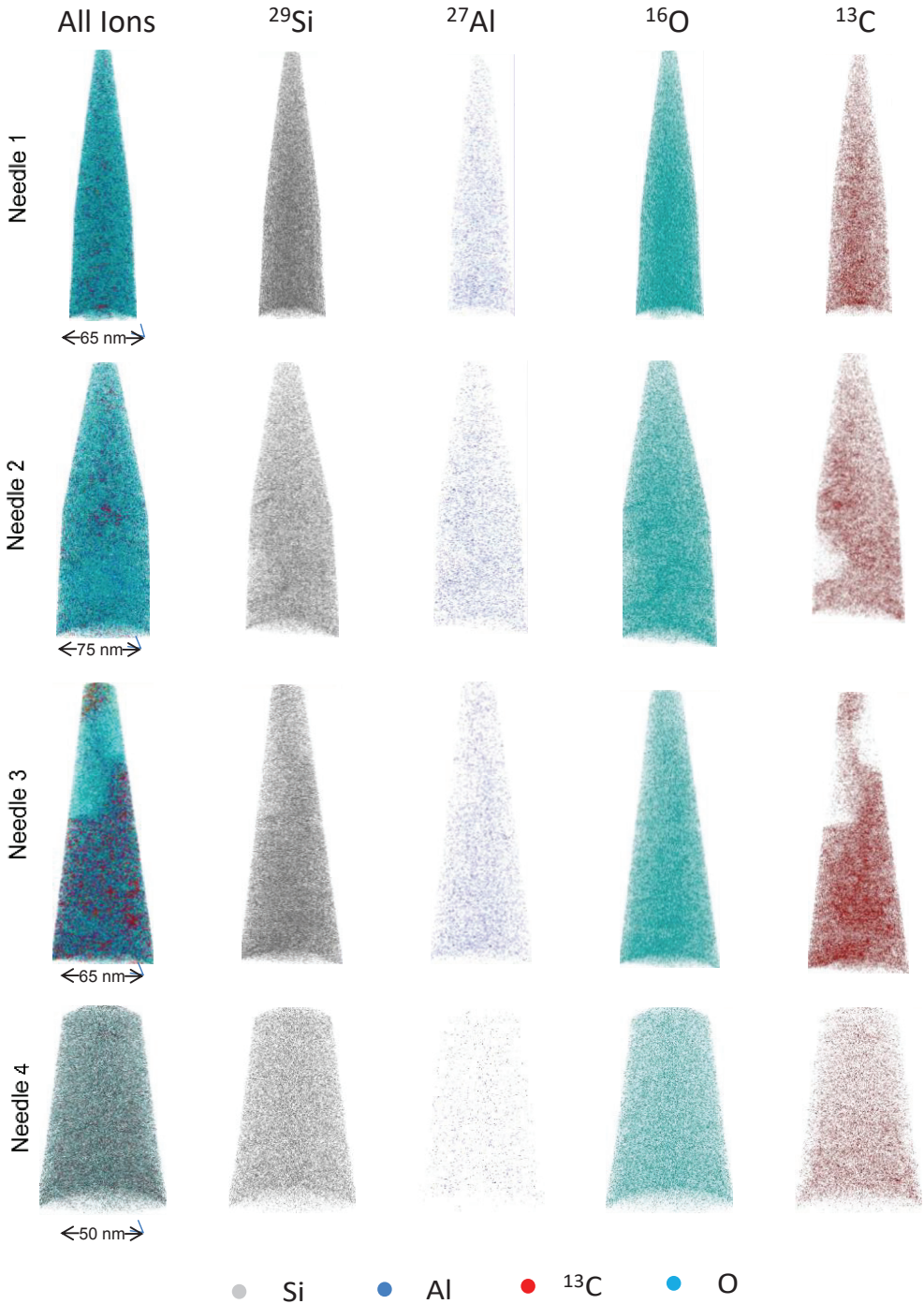


Figure 5.5. 3-D reconstruction of the analyzed APT needles for a zeolite ZSM-5 crystal reacted with ^{13}C labeled methanol at $350\text{ }^\circ\text{C}$ for 90 min. The color scheme of the needles is given at the bottom of the figure.

Possibly, the structural features, that APT could not resolve, such as subunit boundaries and/or crystallographic defects, caused these changes in ^{13}C concentration.

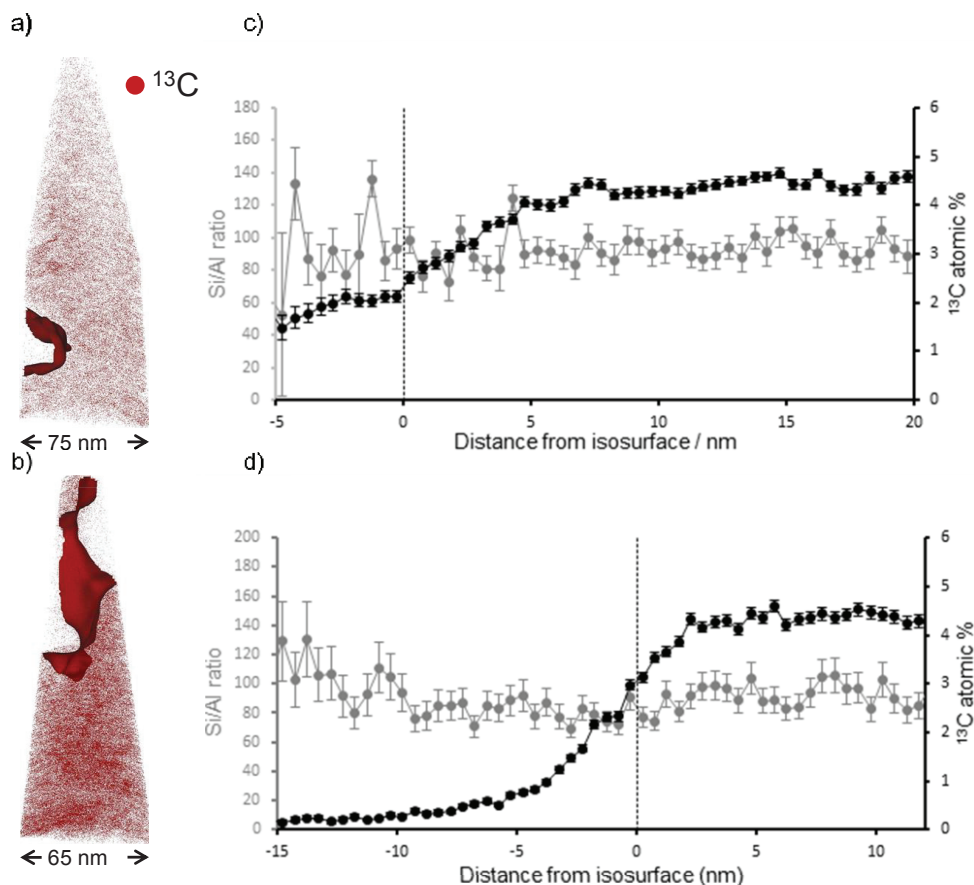


Figure 5.6. The ^{13}C isosurface of a) APT needle 2 (0.5 %, ^{13}C boundary) and b) APT needle 3 (3 %, ^{13}C boundary). The correlation between the Si/Al ratio and ^{13}C % proximity histogram across the isosurface shown on the c) APT needle 2 and d) APT needle 3. The needles are obtained from a zeolite ZSM-5 crystal reacted with ^{13}C labeled methanol at 350 °C for 90 min.

Apart from the ISA, CA is a powerful tool that provides information about elemental segregations that are much smaller than the ISA. Significant clusters are indicated using the NND of the atom pairs in the collected data. Figure 5.7a shows the identified ^{13}C atom clusters (black) and all ^{13}C atoms (red) in APT needle 3. Next to the cluster analysis, an FDA was performed to detect the statistical significance of the heterogeneity of the carbon distribution. These analyses showed notable carbon heterogeneity in all four APT needles. The ^{13}C atom pair distances of the datasets were compared with the randomized datasets and the results are illustrated in Figure

5.7b. The carbon (^{13}C) distribution in the needles was described using two Gaussian functions. One Gaussian was centered near the maxima of the randomized NND and one centered at lower NND values. These locations mean there are two populations of ^{13}C , one with a random distribution and one with a densely packed atomic distribution.

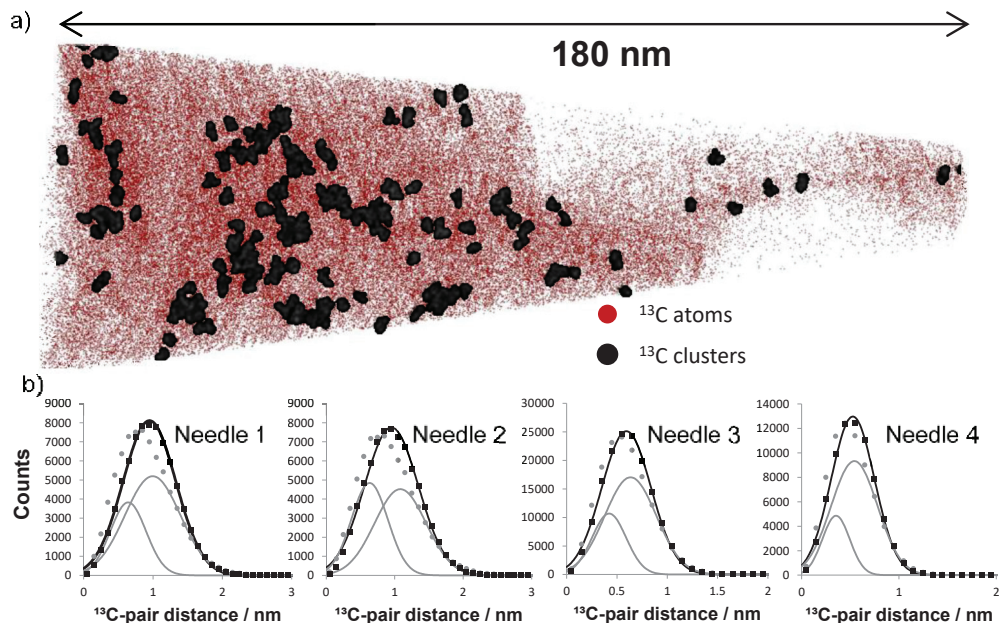


Figure 5.7 a) Reconstruction of the APT needle 3, originating from a zeolite ZSM-5 crystal reacted with ^{13}C labeled methanol at 350 °C for 90 min. The ^{13}C ions are shown in red together with the identified ^{13}C clusters (black). b) Gaussian fits of the ^{13}C -pair distances. The measured data are in gray while the randomized data are plotted in black. The APT needle numbers are given on the corresponding graphs.

An example of a set of zeolite mass spectra of an APT measurement is given in Figure 5.8, showing only ions that contain a best a few atoms. The cluster amounts, sizes and compositions were counted for each APT needle using their mass spectra which is summarized in Table 5.2. The smallest cluster (N_{\min}) contained ten ^{13}C atoms. Considering the $\sim 37\%$ detection efficiency of APT, the detected smallest cluster had approximately thirty ^{13}C atoms which can only be a few molecules or a single methylated polycyclic species. The median cluster size (considering the detection efficiency) contained 36-69 ^{13}C atoms. This number suggests that most of the carbon clusters can contain several trapped coke species. It is crucial to mention here that the APT technique is not capable of molecular fingerprinting as it is a destructive technique. Possible known occluded hydrocarbon species formed during the MTH process in zeolite ZSM-5^[24-26] and their number of carbon atoms are given in Figure 5.9.

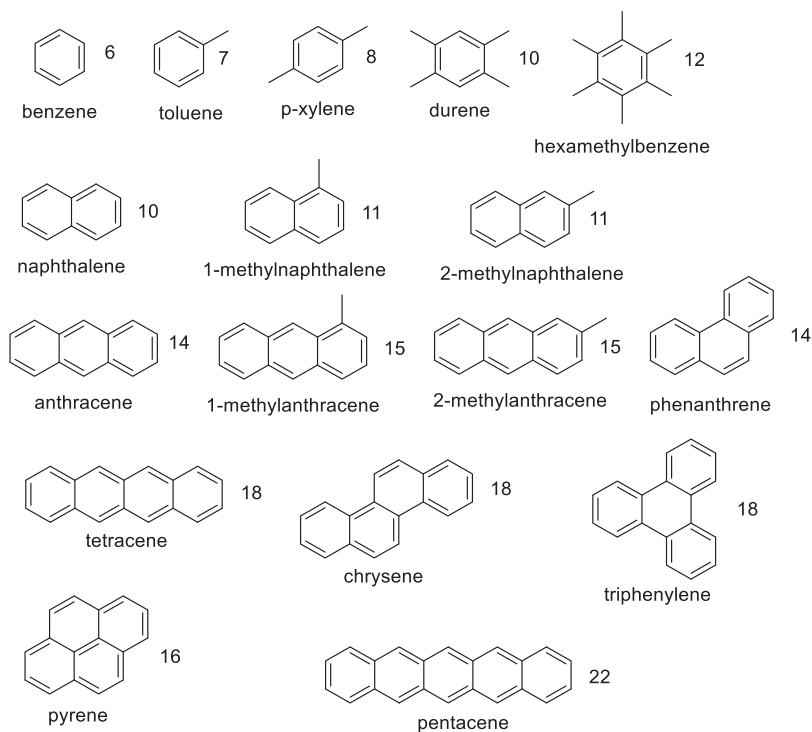


Figure 5.9. Potential trapped coke species formed during the MTH process within zeolite ZSM-5. Coke species are given with numbers of carbon atoms per molecule.

The small carbon clusters detected were probably the first ones to form during the MTH process as this is a 90 min reaction. These small clusters then transform into larger coke-rich regions, shown in the isosurface analysis as illustrated in Figure 5.6a-b. The reason for the detection of ^{13}C in all the APT needles analyzed was due to the methanol presence throughout the entire zeolite ZSM-5 volume. Over time, the Al-rich regions that are near the zeolite ZSM-5 crystals' surface^[27], caused the formation of a greater quantity and size of coke species shown by the higher coke content of the APT needles taken from the near-surface region of the zeolite crystal.

The distribution of Al-pair distances was also considered with CA for all the APT needles. Unlike the ^{13}C clusters, no inhomogeneities in Al distribution could be identified. The Al-pair distances in the APT needles including their comparison with randomized distribution are demonstrated in Figure 5.10. It may seem counterintuitive not to see Al clusters considering the Al concentration was elevated in the ^{13}C clusters. This can be explained as, in order to identify carbon clusters, the increase of the local carbon content detected in the APT needle was at least five-

fold compared to the bulk. However, the aluminum increase was much smaller, preventing statistically relevant aluminum clusters from being identified. A RDF analysis was performed in order to observe the spatial Si/Al changes in the surroundings of the coke content with the four APT needles. The Si/Al ratio with respect to the distance from the clustered coke regions is shown in Figure 5.11.

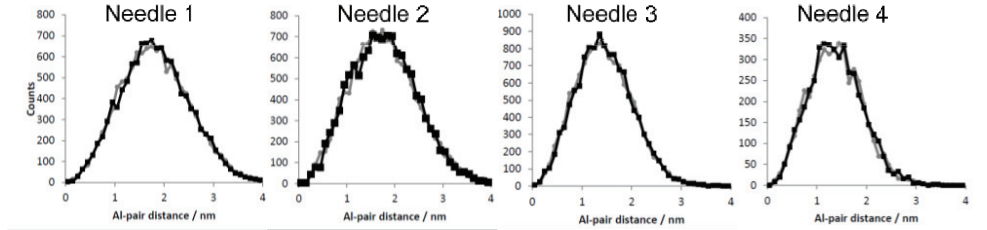


Figure 5.10. NNDs for Al-pair distances. The measured data are shown in grey, while the randomized data are shown in black. The APT needle numbers are given on top of each graph.

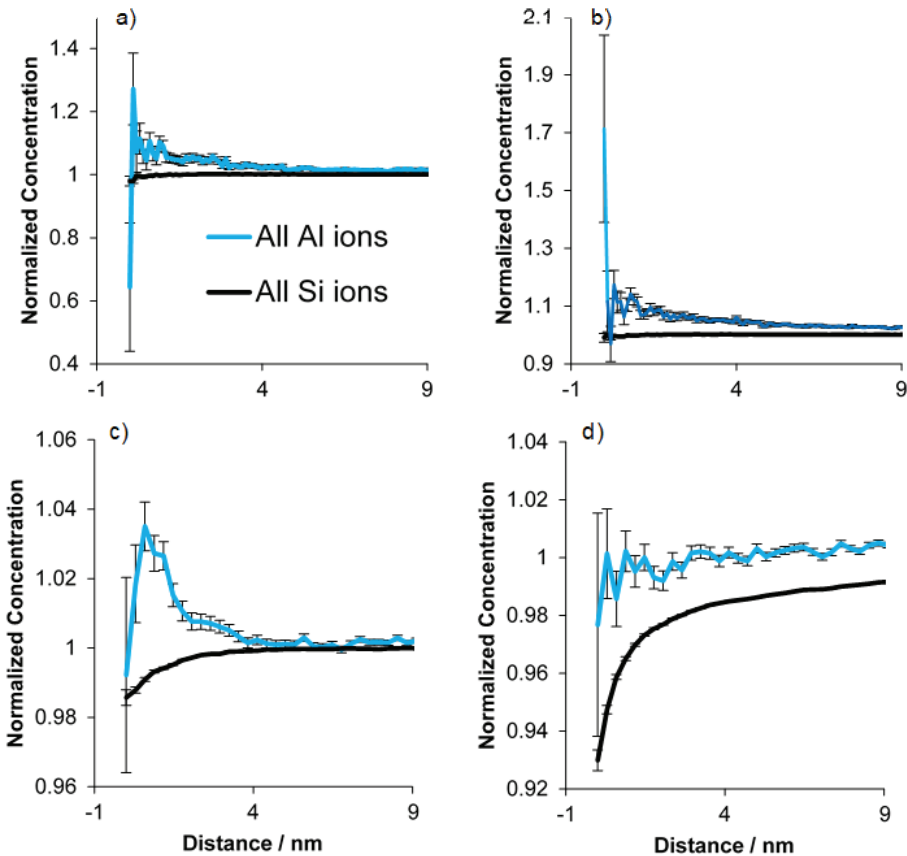


Figure 5.11. RDFs for clusters for Si and Al ions for a) APT needle 1, b) APT needle 2, c) APT needle 3 and d) APT needle 4. The error bars are calculated via counting statistics. The high error near the cluster centers is due to a low number of ions counted.

5.4 Conclusions

Large zeolite ZSM-5 crystals, which were reacted for 90 min in a ^{13}C labeled methanol stream at 350 °C, were studied with Atom Probe Tomography (APT). The carbonaceous species formed and trapped inside the zeolite crystal during the Methanol-to-Hydrocarbons (MTH) reaction were detected. Regions of coke deposits were observed at different length scales as isosurfaces and as clustered carbon atoms. These carbon clusters are possibly the first precursors of coke formation that lead to pore blockage and eventual catalyst deactivation. Moreover, the detected coke species were found in regions where the local Si/Al ratio was decreased. The relationship between Al sites and coke species shown in previous Chapters at the micron and nanometer scale could now be revealed at the sub-nm scale. An increased Al concentration was found close to the ^{13}C sites. Most possibly the (deactivation causing) hydrocarbon pool species preferably form in the Al-enriched regions. This work also demonstrates the importance of controlling the location of the acid sites at the nanoscale for coke prevention. Also, the nanoscopic Al concentration fluctuations are shown to have a high impact on coke formation. This first successful application of the APT methodology on partially deactivated zeolite crystals that are; non-conductive, and consists of organic and inorganic species, show the power of this novel characterization tool in the field of zeolite science and technology. It certainly opens new doors to its application in the much broader field of heterogeneous catalysis, including e.g. metal-loaded zeolites.^[28]

5.5. Acknowledgments

Machteld Martens (ExxonMobil, Belgium) is acknowledged for providing the large zeolite ZSM-5 crystals. The APT measurements were conducted at the Center for Nanophase Material Sciences (CNMS), which is part of Oak Ridge National Laboratory (ORNL). We thank Jonathan D. Poplawsky (ORNL) and Baisakhi Mazumder (ORNL) for the APT experiments. Joel E. Schmidt (Utrecht University, UU) and Donglong Fu (UU) are acknowledged for being part of the experimental team and for fruitful discussions. Florian Meirer (UU) is thanked for productive consultations. Olga Ovchinnikova (ORNL) is thanked for supervising the experimental work at ORNL.

5.6. Contributions

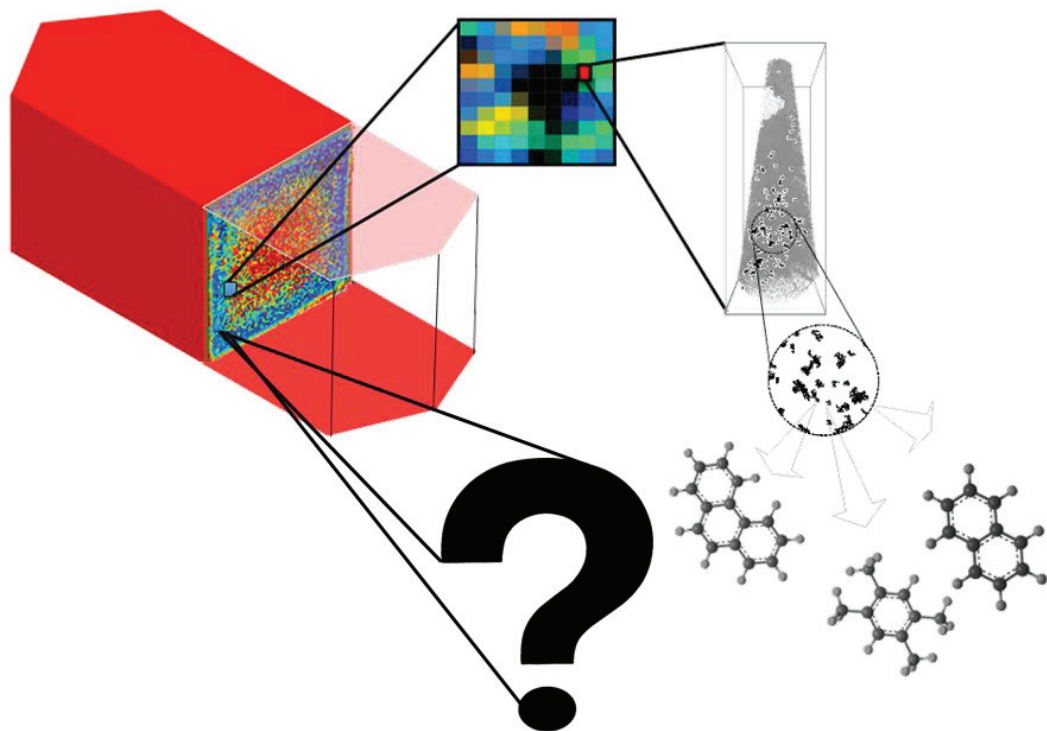
Bert Weckhuysen (Utrecht University, UU), Özgün Attila and Simon R. Bare (Stanford Linear Accelerator Center, SLAC) conceived the idea and wrote the proposal for the experimental plan at ORNL. Özgün Attila prepared the zeolite samples and performed the MTH experiments. Jonathan D. Poplawsky (ORNL) and

Baishakhi Mazumder (ORNL) performed the APT measurements with on-site guidance by Özgün Attila, Joel E. Schmidt (UU) and Donglong Fu (UU). Sample reconstructions and initial data analysis was primarily performed by Jonathan D. Poplawsky with input from Joel E. Schmidt, Özgün Attila and Donglong Fu. Data interpretation was done by Özgün Attila, Joel E. Schmidt, Donglong Fu, Florian Meirer, Simon R. Bare and Bert M. Weckhuysen. The related manuscript was prepared by Joel E. Schmidt, Özgün Attila and Donglong Fu with written contributions from all co-authors. Florian Meirer (UU) and Bert Weckhuysen provided assistance with interpretation of the data and made revisions and corrections to the chapter.

References

- [1] I. L. C. Buurmans, B. M. Weckhuysen, *Nat. Chem.* 2012, 4, 873–886.
- [2] B. M. Weckhuysen, *Angew. Chem. Int. Ed.* 2009, 48, 4910–4943.
- [3] B. M. Weckhuysen, *Chem. Soc. Rev.* 2010, 39, 4557–4559.
- [4] B. M. Weckhuysen, J. Yu, *Chem. Soc. Rev.* 2015, 44, 7022–7024.
- [5] D. Mores, J. Kornatowski, U. Olsbye, B. M. Weckhuysen, *Chem. Eur. J.* 2011, 17, 2874–2884.
- [6] L. R. Aramburo, E. De Smit, B. Arstad, M. M. Van Schooneveld, L. Sommer, A. Juhin, T. Yokosawa, H. W. Zandbergen, U. Olsbye, F. M. F. de Groot, B. M. Weckhuysen, *Angew. Chem. Int. Ed.* 2012, 51, 3616–3619.
- [7] J. P. Hofmann, D. Mores, L. R. Aramburo, S. Teketel, M. Rohnke, J. Janek, U. Olsbye, B. M. Weckhuysen, *Chem. Eur. J.* 2013, 19, 8533–8542.
- [8] D. M. Bibby, C. G. Pope, *J. Catal.* 1989, 116, 407–414.
- [9] D. M. Bibby, N. B. Milestone, J. E. Patterson, L. P. Aldridge, *J. Catal.* 1986, 97, 493–502.
- [10] D. J. Larson, T. J. Prosa, R. M. Ulfing, B. P. Geiser, T. F. Kelly, *Local Electrode Atom Probe Tomography*, Springer, New York, 2013.
- [11] E. W. Müller, *J. Appl. Phys.* 1956, 27, 474–476.
- [12] E. W. Müller, J. A. Panitz, S. B. McLane, *Rev. Sci. Instrum.* 1968, 39, 83–86.
- [13] D. E. Perea, I. Arslan, J. Liu, Z. Ristanović, L. Kovarik, B. W. Arey, J. A. Lercher, S. R. Bare, B. M. Weckhuysen, *Nat. Commun.* 2015, 6, 7589–7596.
- [14] J. Schmidt, L. Peng, J. Poplawsky, B. M. Weckhuysen, *Angew. Chem. Int. Ed.* 2018, 57, 10422–10435.
- [15] B. A. Sexton, A. E. Hughes, D. M. Bibby, *J. Catal.* 1988, 109, 126–131.
- [16] F. L. Bleken, K. Barbera, F. Bonino, U. Olsbye, K. P. Lillerud, S. Bordiga, P. Beato, T. V. W. Janssens, S. Svelle, *J. Catal.* 2013, 307, 62–73.

- [17] L. R. Aramburo, S. Teketel, S. Svelle, S. R. Bare, B. Arstad, H. W. Zandbergen, U. Olsbye, F. M. F. De Groot, B. M. Weckhuysen, *J. Catal.* 2013, *307*, 185–193.
- [18] L. R. Aramburo, L. Karwacki, P. Cubillas, S. Asahina, D. A. M. De Winter, M. R. Drury, I. L. C. Buurmans, E. Stavitski, D. Mores, M. Daturi, P. Bazin, P. Dumas, F. Thibault-Starzyk, J. A. Poost, M. W. Anderson, O. Terasaki, B. M. Weckhuysen, *Chem. Eur. J.* 2011, *17*, 13773–13781.
- [19] K. Thompson, D. Lawrence, D. J. Larson, J. D. Olson, T. F. Kelly, B. Gorman, *Ultramicroscopy* 2007, *107*, 131–139.
- [20] E. Stavitski, M. H. F. Kox, B. M. Weckhuysen, *Chem. Eur. J.* 2007, *13*, 7057–7065.
- [21] T. J. Prosa, P. H. Clifton, H. Zhong, A. Tyagi, R. Shivaraman, S. P. Denbaars, S. Nakamura, J. S. Speck, *Appl. Phys. Lett.* 2011, *98*, 191903.
- [22] C. K. Sudbrack, R. D. Noebe, D. N. Seidman, *Phys. Rev. B - Condens. Matter Mater. Phys.* 2006, *73*, 212101.
- [23] D. Haley, T. Petersen, G. Barton, S. P. Ringer, *Philos. Mag.* 2009, *89*, 925–943.
- [24] I. Yarulina, J. Goetze, C. Gücüyener, L. van Thiel, A. Dikhtiarenko, J. Ruiz-Martinez, B. M. Weckhuysen, J. Gascon, F. Kapteijn, *Catal. Sci. Technol.* 2016, *6*, 2663–2678.
- [25] R. Y. Brogaard, B. M. Weckhuysen, J. K. Nørskov, *J. Catal.* 2013, *300*, 235–241.
- [26] J. E. Schmidt, J. D. Poplawsky, B. Mazumder, Ö. Attila, D. Fu, D. A. M. de Winter, F. Meirer, S. R. Bare, B. M. Weckhuysen, *Angew. Chem. Int. Ed.* 2016, *55*, 11173–11177.
- [27] N. Danilina, F. Krumeich, S. A. Castelanelli, J. A. van Bokhoven, *J. Phys. Chem. C* 2010, *114*, 6640–6645.
- [28] J. E. Schmidt, R. Oord, W. Guo, J. D. Poplawsky, B. M. Weckhuysen, *Nat. Commun.* 2017, *8*, 1666.



CHAPTER
VI

Summary
Future Outlook and
Nederlandse Samenvatting

6.1. Summary

Methanol-to-Hydrocarbons (MTH) conversion over microporous aluminosilicates and silico-aluminophosphates, with special emphasis on zeolite ZSM-5 (with the MFI topology) and zeolite analogue SAPO-34 (with the CHA topology), is considered as a versatile process to synthesize a variety of base chemicals from almost any type of resource, from which methanol can be made. This variety as well as the importance of the base chemicals produced, makes the MTH process one of the most studied chemical reactions within both academia and industries. A variety of mechanistic proposals for the MTH reaction has been proposed in the past two decades, although there are still a lot of unknowns with respect to the activation and deactivation of zeolite-based catalyst materials as well as in the way the reaction product selectivity can be steered.

The scope of this PhD Thesis is to examine the formation of undesired carbonaceous species, often denoted as coke deposits, within zeolite ZSM-5 during the MTH process. For this purpose, a variety of micro- and nano-spectroscopic and chemical imaging techniques have been used. With this toolbox in hand, we have revealed the nature of the desired and undesired reaction products in a time and spatial manner from the micron to the atomic scale. We furthermore, altered the physicochemical properties of the zeolite-based catalysts using a hydrothermal treatment process in order to gain further insights into the mechanisms and the nature of the coke products upon zeolite steaming. The model of choice has been large zeolite ZSM-5 crystals, which have been the subject of several detailed studies of our group, in part reported in the PhD works of Lukasz Karwacki, Marianne Kox, Luis Aramburo, Davide Mores and Zoran Ristanovic. In this PhD work, we make the next step in this research by involving new spectroscopy and microscopy methodologies to research these model zeolite crystal systems in more detail.

In **Chapter 2**, we have investigated the large zeolite ZSM-5 crystals to gain insights into the modifications caused by a hydrothermal treatment at two different reaction temperatures (500 and 700°C) on the zeolite acidity, the 3-D elemental distribution as well as the integrity and stability of the zeolitic framework. These zeolite crystals have been denoted as P-ZSM-5 (parent ZSM-5 crystal), MT-ZSM-5 (mildly treated crystal, treated at 500°C) and ST-ZSM-5 (severely treated crystal, treated at 700°C). For this purpose, confocal Raman micro-spectroscopy has been used. The 3-D distribution of Al and Si sites within the three sets of zeolite ZSM-5 crystals has been identified, as schematically illustrated in Figure 6.1. Raman micro-spectroscopy revealed that the mild and severe steaming conditions promote the formation of heterogeneities in the near surface regions of the zeolites most probably

via the extraction of framework aluminium. Furthermore, some of the dislodged aluminium species were observed to migrate towards the crystal core through the mesopores formed via steaming. Some of the (partially) dislodged aluminium was found to be clustered in the aluminium-rich zone in the near-outer surface regions of the crystals.

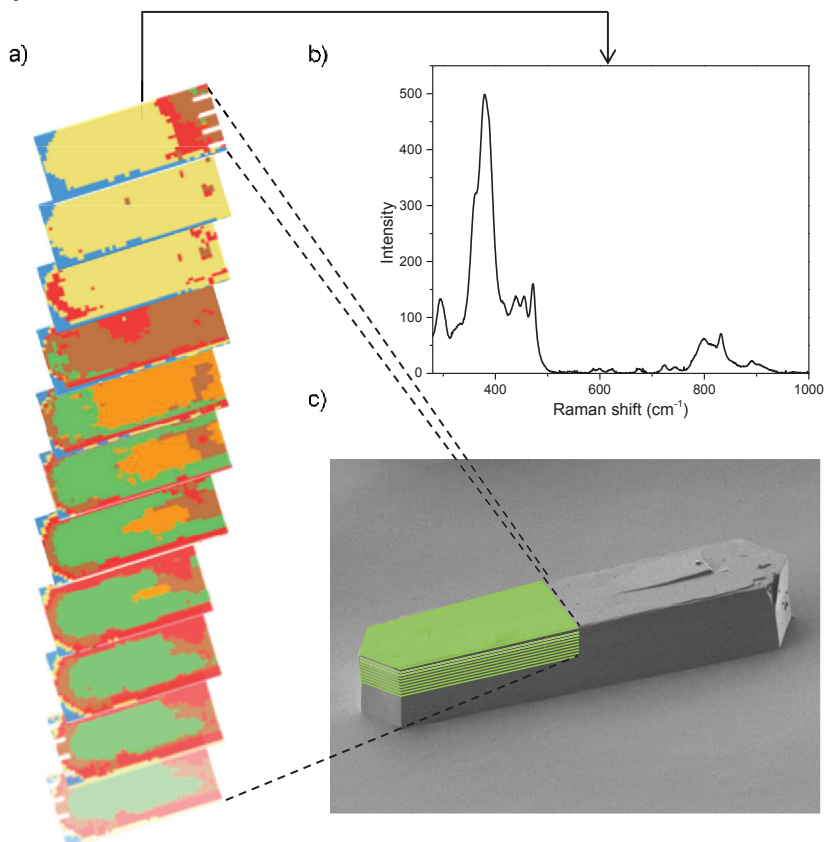


Figure 6.1 a) Clustering results of each individual 3-D Raman micro-spectroscopy map of a P-ZSM-5 zeolite crystal. b) Average Raman spectrum of a P-ZSM-5 zeolite crystal. c) 3-D location of each Raman micro-spectroscopy map on the P-ZSM-5 zeolite, as shown in the SEM picture of the crystal.

Further insights into the porosity modifications and Brønsted acidity caused by the application of the hydrothermal treatment procedures at different temperatures (500°C and 700°C) on the activity and selectivity of the MTH reaction have been obtained in **Chapter 3**. This has been done by using a correlative approach of operando UV-Visible micro-spectroscopy and operando confocal fluorescence microscopy, including on-line mass spectrometry. This approach has revealed that decreasing the Brønsted acid site density via increasing the severity of

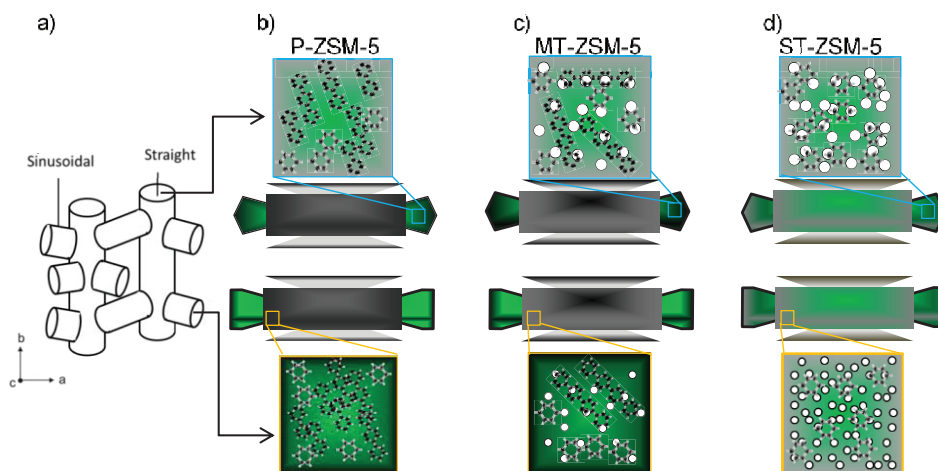


Figure 6.2. a) Zeolite ZSM-5 pore system. Schematic representation of the coking mechanism at the roof and side orientations of a b) P-ZSM-5 c) MT-ZSM-5 d) ST-ZSM-5 crystal. Coke formation is described with black gradient. Upper row shows the roof orientation of the crystals and the lower row shows the side view of the zeolite ZSM-5 crystal.

the steaming conditions, prevented the further methylation of the formed reaction (by-)products. The steaming conditions played an important role in the formation of carbonaceous species. Zeolite mesoporosity, introduced under mild steaming conditions, allowed the formation of larger hydrocarbon species due to presence of mesopores and an adequate number of Brønsted acid sites. Under severe steaming conditions, the decreased Brønsted acid site density hindered the formation of larger hydrocarbon species, no matter the presence of additional mesopores created upon steaming in this zeolite material. Furthermore, the increased diffusion capabilities of the zeolite ZSM-5 crystals brought via (severe) steaming were followed under operando conditions with confocal fluorescence microscopy. Coking of the zeolite ZSM-5 crystals started at the edge sites of the crystals. Steaming increased the diffusion capabilities, which prevented the complex and conjugated coke formation under MTH conditions. The main findings of this Chapter are summarized in Figure 6.2.

In **Chapter 4**, rather than focusing on the hydrothermally treated zeolite ZSM-5 crystals, we have studied the elemental composition of the zeolite ZSM-5 crystals and its relationship with the spatial coke formation during MTH reaction. We have developed and used the method of ion mass spectrometry to distinguish the Brønsted acid sites within the zeolite ZSM-5 crystals via the Al distribution, down to the nanoscale. Simultaneously, we have been able to determine the coke distribution within these crystals, which were subjected to the MTH reaction. Heterogeneities

have been observed within the ZSM-5 crystal as we detected a sub- μm thick silicalite layer surface crust that is poor in aluminium. An aluminium enriched zone that is a few μm thick was observed to follow the surface silicalite layer. Furthermore, this amount of Al was detected to gradually decrease towards the core of the zeolite ZSM-5 crystal. This is schematically shown in Figure 6.3a. Probing the nano-scale elemental distribution of the zeolite ZSM-5 crystal has validated the two-component

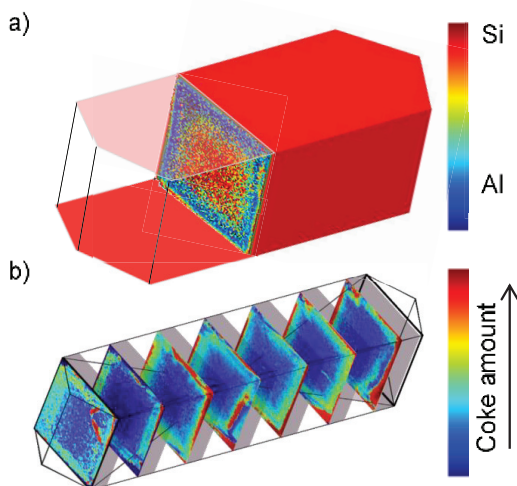


Figure 6.3. a) Si/Al distribution within a zeolite ZSM-5 crystal b) Coke distribution within a ZSM-5 crystal.

ZSM-5 crystal model that states the presence of six pyramidal subunits. Ion mass spectrometry has further revealed the presence of diffusion barriers at the shared facets of the six zeolite subunits. Carbonaceous species start forming in the near-

surface areas where Brønsted acid sites are present and then further penetrate into the zeolite crystal with increasing reaction time. The coke species enlarge in their molecular size with increasing time-on-stream and mostly accumulate near the Al zone of the crystal, although they also accumulate near the diffusion barriers. The coke distribution inside a zeolite ZSM-5 crystal is shown in Figure 6.3b. Eventually, the MTH process suffers from diffusion limitations, which may be considered as the main cause for catalyst deactivation.

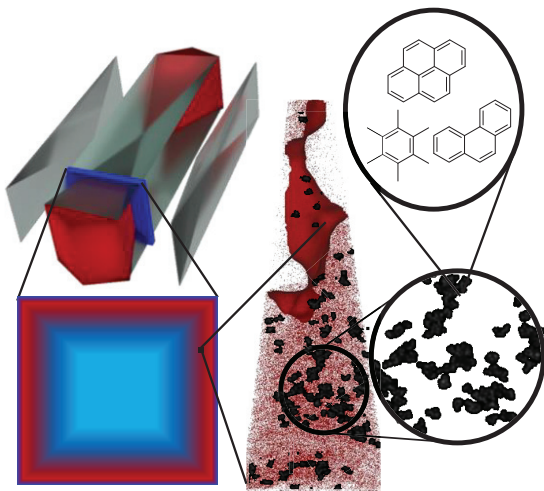


Figure 6.4. Reconstruction of an APT needle. The location of the needle on the zeolite ZSM-5 crystal is shown in the panel (low left). The ^{13}C ions are shown in red together with the identified ^{13}C clusters (black). Possible coke species that are present in these clusters are given (top right).

Chapter 5 illustrates the final piece of the puzzle of how coke formation takes place within a zeolite ZSM-5 crystal during the MTH process. Here, the first application of Atom Probe Tomography (APT) on both fresh and partially deactivated zeolite ZSM-5 crystals has been explored. The successful application of APT to a catalyst system that contains both organic and inorganic species has revealed the exact atom positions inside the zeolite ZSM-5 structure. The distribution of zeolite framework atoms and the carbon atoms present in the trapped carbonaceous species were determined with sub-nanometer resolution. Due to the destructive nature of the APT method, we could not identify the exact molecular structure of the formed carbonaceous species, but we could estimate the number of carbon atoms present in the surroundings of Brønsted acid sites. A typical carbon cluster size is comprised of between 36 and 69 carbon atoms. These observations are in line with the proposed hydrocarbon pool mechanism, as initially proposed by Dahl and Kolboe, and briefly discussed in Chapter 1. A summary of the main findings of Chapter 5 is shown in Figure 6.4. The general overview of our complementary zeolite characterization approach is schematically illustrated in Figure 6.5.

The goal of this PhD Thesis was to provide a better understanding of the mechanism and finding causes for catalyst deactivation of zeolite ZSM-5 crystals during the MTH process. Considering the work presented, we can draw some more general conclusions. Indeed, the large zeolite ZSM-5 crystals used in this study are inherently heterogeneous. They have a silicalite crust that is followed by a gradually decreasing Al zone towards the zeolite ZSM-5 crystal core. The Al atoms present in the zeolite ZSM-5 framework give rise to the formation of Brønsted acid sites, which are the active sites for the hydrocarbon conversion processes. Since the Al enrichment is on the edge sites, the formation of coke species under MTH conditions takes place mostly in the outer surface and the near surface regions of the zeolite ZSM-5 crystals under study. The decreased spatial constraints in the outer crust allow the enlarged pseudo-graphitic carbonaceous species to be formed and introduce hindered molecular transport. The diffusion barriers, that cause anisotropic diffusion, are intrinsic to the large zeolite ZSM-5 crystal framework and fasten the catalyst deactivation. We have also applied post-treatment methods i.e., steaming to the zeolite ZSM-5 at two different temperatures, in order to alter the molecular transport properties as well as the acidity of the catalyst materials. Steaming increased the heterogeneities in the zeolite ZSM-5 crystals. The formation of mesopores, Al migration and the increase in extra-framework Al species also took place. All these alterations prevented the further conjugation of hydrocarbon species and caused better diffusion of the reaction species, albeit at the expense of a decreasing overall activity. These observations are schematically illustrated in Figure 6.6.

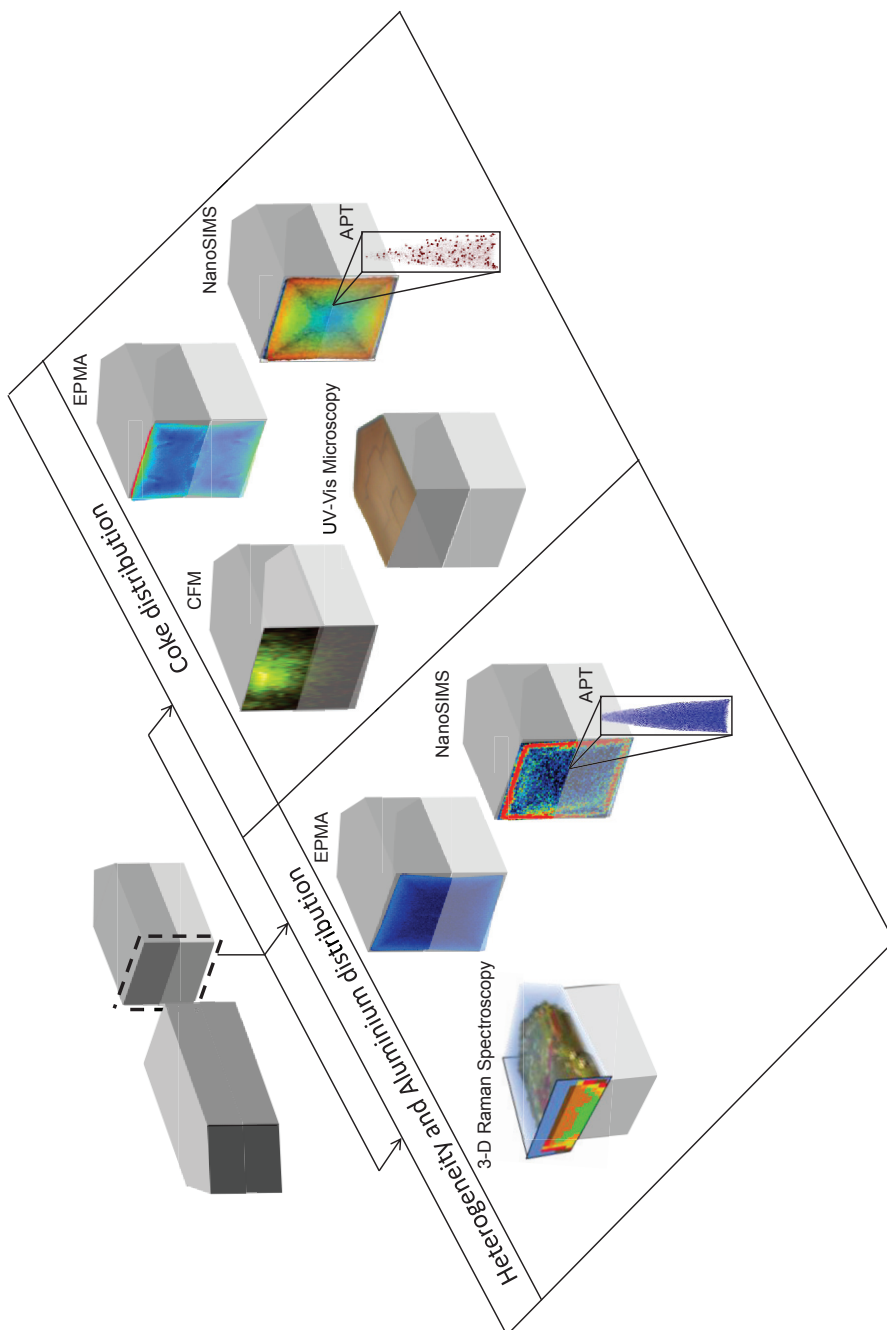


Figure 6.5. The general overview of the techniques used for the characterization of zeolite ZSM-5 crystals used for the MTH process in this PhD study.

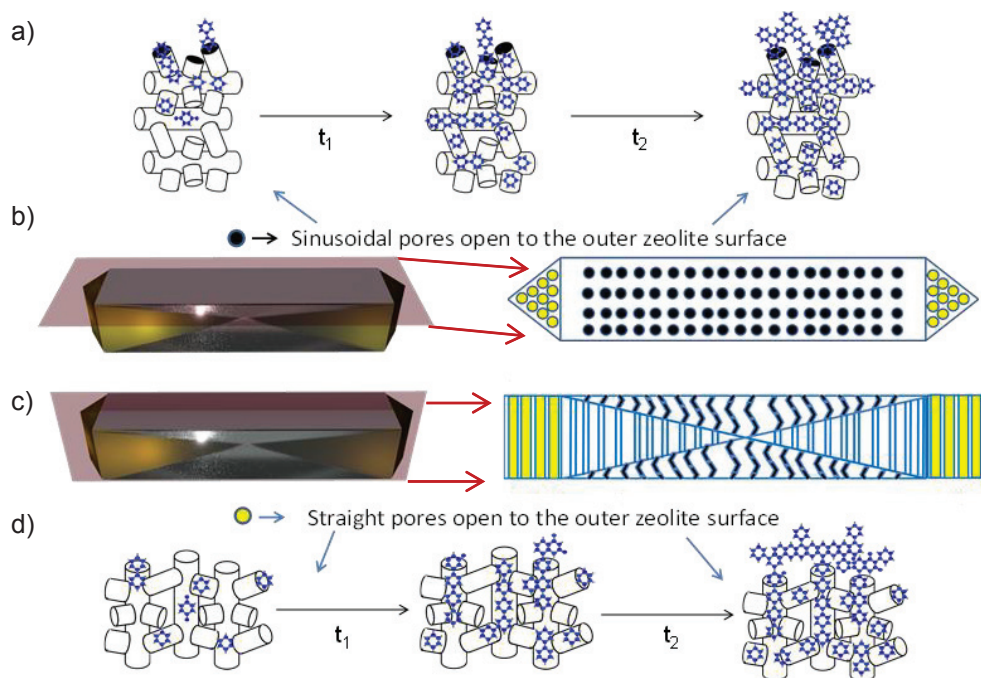


Figure 6.6. a) Surface coverage of coke species formed during MTH on the sinusoidal pore system, which is open to the middle region of the outer zeolite surface ($t_1 < t_2$). b) Left: illustration of a horizontal surface oriented cross section of a zeolite ZSM-5 crystal. Right: a schematic representation of the pore orientations on the crystal surface. c) Left: illustrations of a vertical cross section to the center of a zeolite ZSM-5 crystal, with on the right the schematic representation of the pore orientations in the crystal center. d) Surface coverage of coke species formed during MTH on the straight pore system which is open to surface in the triangular areas on the crystal top surface ($t_1 < t_2$).

6.2. Future Outlook

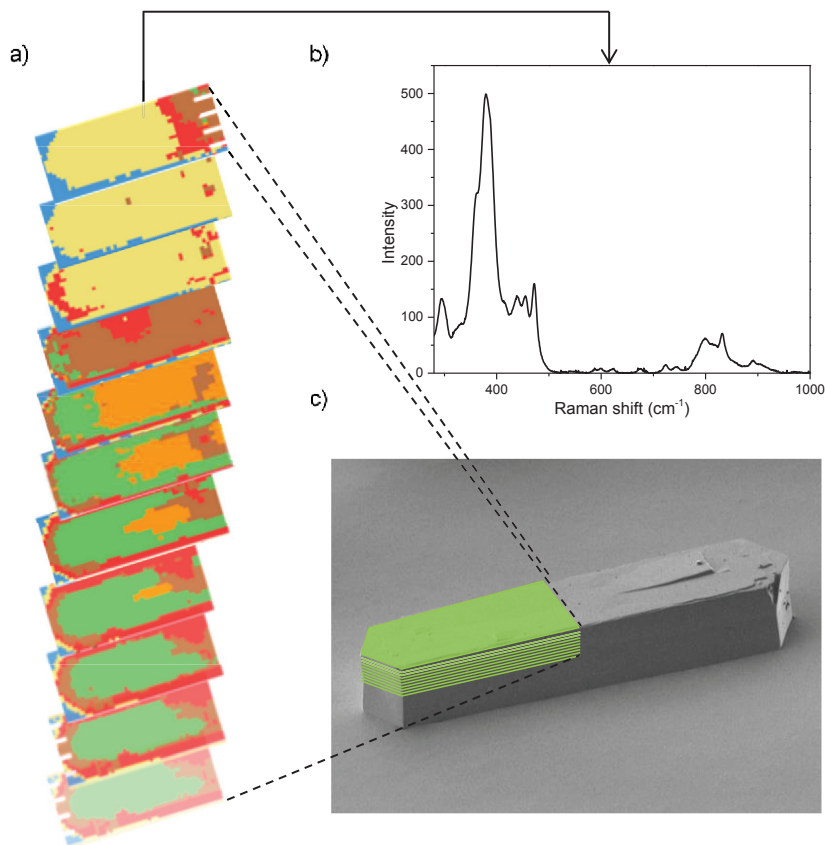
This PhD Thesis focuses on the relevant problems and bottlenecks that are encountered in modern catalysis. The industrially relevant problem of carbonaceous species formation during hydrocarbon conversion processes on solid acid catalysts was studied by using a combination of spectroscopy and microscopy. Assessment of zeolite structure-property relationships as well as the crystallographic orientation of micropores within zeolite frameworks are essential ingredients for better understanding the catalytic performance. The complex and dynamic nature of the catalytic hydrocarbon conversion processes within molecular sieves can only be understood upon the observation of the real-time changes in both structure and activity; hence the focus of this work was to try to connect the distribution or zoning

of Al with the formation of hydrocarbon deposits within large zeolite ZSM-5 crystals, as outlined in Figure 6.5.

Through conventional Raman microscopy, we mapped our model system, namely large crystals of zeolite ZSM-5, in 3-D. We were able to map the heterogeneities and the elemental distribution through the molecular bond distribution of the complex structure of the zeolite ZSM-5. Extrapolating this 3-D mapping approach to a variety of relevant topologies e.g., CHA (SAPO-34), TON (ZSM-22) and RHO (DNL-6) to create a library for identification of porous materials can be crucial for the characterization of porous materials. In this way, the influence of post-treatment methods, detemplation processes, and regeneration on the molecular structure and elemental distribution can be defined. In this regard, Principal Component Analysis (PCA) has shown to be indispensable to understand the complex structure as well as chemical composition of these porous materials. The microscale resolution of conventional Raman spectroscopy causes a spatial limitation as one is averaging out the chemical information from the nanoscale. A way to further improve the spatial resolution of Raman spectroscopy is to use Tip Enhanced Raman Spectroscopy (TERS). TERS uses a specially coated Atomic Force Microscopy (AFM) tip for reflecting the Raman laser into much smaller areas to enhance the Raman signal of e.g. organic deposits. A similar approach can be followed for infrared light. Here, Photoinduced Force Microscopy (PiFM) provides nanometer-scale resolution across the infrared spectral range. As infrared spectroscopy is an established tool in catalysis, one can envisage investigating e.g. the adsorption of organic molecules at the surface of zeolites and analyzing in 2-D the number and strength of acid sites with nanometer resolution. In the same family of AFM methods, one can also envisage Kelvin Probe Force Microscopy (KPFM). Here, the work function of surfaces can be studied with high spatial resolution via the application of the surface potential, which is related to e.g. the elemental distribution and oxidation level of the material under study. Clearly, the exploration of AFM-based characterization methods, including TERS, PiFM and KPFM, are valuable tools to further characterize the large zeolite ZSM-5 crystals as model systems for the MTH process and other hydrocarbon conversion processes.

6.3. Nederlandse Samenvatting

De omzetting van methanol naar koolwaterstoffen (MTH) over microporeuze aluminosilicaten en silico-aluminofosfaten, vooral zeolieten ZSM-5 (met de MFI topologie) en zijn analoog SAPO-34 (met de CHA topologie), wordt gezien als een veelzijdig proces om verschillende veelgebruikte chemicaliën te maken vanuit bijna elke grondstof, waar methanol van kan worden gemaakt. Deze flexibiliteit, samen



Figuur 6.7 a) Clustering resultaat van elke individuele 3-D Raman micro-spectroscopie map van een P-ZSM-5 zeoliet kristal. b) Gemiddelde Raman spectrum van een P-ZSM-5 zeoliet kristal. c) 3-D locatie van elke Raman micro-spectroscopie map op het P-ZSM-5 zeoliet, zoals weergegeven in het SEM plaatje van het kristal.

met het belang van de gemaakte chemicaliën, maken het MTH proces tot een van de meest bestudeerde chemische reacties in zowel de academische wereld als de chemische industrie. Er zijn een groot aantal verschillende mechanistische voorstellen voor de MTH reactie gedaan gedurende de laatste twee decennia, maar toch zijn er nog veel onzekerheden met betrekking tot de activatie en deactivatie van zeoliet-gebaseerde katalytische materialen, en ook over hoe de product selectiviteit gevarieerd kan worden.

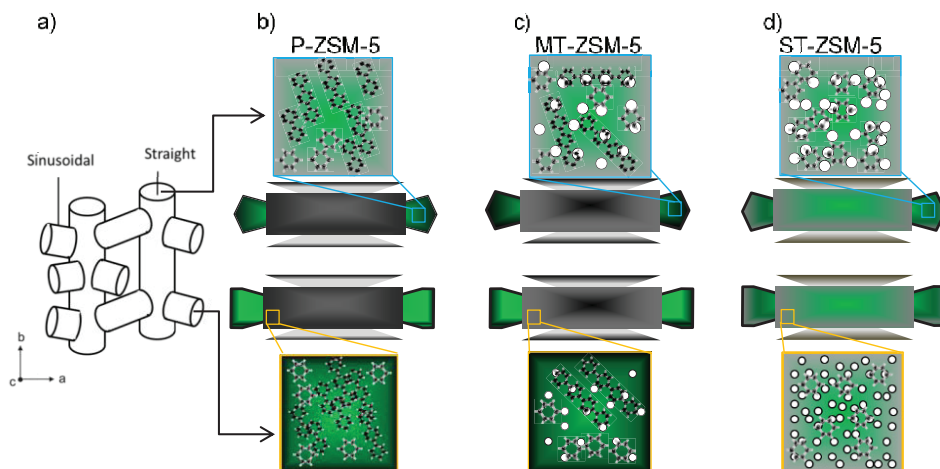
Het doel van dit proefschrift is het monitoren van ongewenste koolwaterstoffen, vaak gedefinieerd als cokemoleculen, binnenin de zeoliet ZSM-5 tijdens het MTH proces. Voor dit doeleinde zijn verschillende micro- en nano-spectroscopische en chemische visualisatie technieken gebruikt. Met deze toolbox ter beschikking, hebben we de aard van de gewenste en ongewenste

reactieproducten aangetoond in een tijd en ruimte-afhankelijke wijze van de micro tot atomische schaal. Verder hebben we de fysisch-chemische eigenschappen van de zeoliet-gebaseerde katalysatoren veranderd met behulp van een hydrothermaal proces, om zo meer te weten te komen over de oorsprong van cokesvorming na het stomen van zeolieten. Grote ZSM-5 zeoliet kristallen zijn gekozen als model, die eerder in detail bestudeerd zijn in de proefschriften van Lukasz Karwacki, Marianne Kox, Luis Aramburo, Davide Mores en Zoran Ristanovic. In dit proefschrift maken we een volgende stap door nieuwe spectroscopische en microscopische methodes te gebruiken om deze zeoliet model kristallen in detail te bestuderen.

In Hoofdstuk 2 hebben we grote zeoliet ZSM-5 kristallen onderzocht om zo inzichten te krijgen in de veranderingen van de zuurheid van de zeoliet, de 3-D distributie van elementen en de integriteit en stabiliteit van de zeoliet structuur, die plaatsvinden door te stomen op twee verschillende temperaturen (500 en 700°C). Deze zeoliet kristallen zijn aangeduid als P-ZSM-5 (parent ZSM-5 kristal), MT-ZSM-5 (mild behandeld kristal, gestoomd op 500°C) en ST-ZSM-5 (zwaar behandeld kristal, gestoomd op 700°C). Voor dit doeleinde is confocale Raman micro-spectroscopie gebruikt. The 3-D distributie van Al en Si plekken in de drie types zeoliet ZSM-5 kristallen is bepaald, zoals schematisch weergegeven in Figuur 6.7. Raman micro-spectroscopie liet zien dan milde en zware stoom omstandigheden de vorming van heterogeniteiten bevordert in plekken dicht bij het oppervlakte, zeer waarschijnlijk door de extractie van aluminium uit de zeoliet structuur. Daarnaast bleken sommige losgekomen aluminium atomen te migreren naar de kristalkern door de mesoporiën die gevormd zijn tijdens het stomen. Een deel van de losgekomen aluminium bleek te zijn geclusterd in een aluminium-rijk gebied in de bijna-buitenste oppervlakte regio's.

Verdere inzichten in de invloed van porositeit en Brønsted zuurheid, veroorzaakt door de verschillende stoom behandelingen, op de activiteit en selectiviteit in het MTH proces zijn behaald in Hoofdstuk 3. Dit is gedaan door een correlatieve benadering te gebruiken van operando UV-zichtbare micro-spectroscopie en operando confocale fluorescentie microscopie, inclusief online massa spectrometrie. Deze benadering heeft aangetoond dat de afnemende Brønsted zuurdichtheid door het verzwaren van de stoombehandeling verdere methylatie van de gevormde reactie (bij)producten voorkwam. De stoomomstandigheden speelden een belangrijke rol in de vorming van koolwaterstoffen. De zeoliet mesoporeusheid, gevormd onder milde stoomomstandigheden, stond de vorming van grotere koolwaterstoffen toe door de aanwezigheid van mesoporiën en een adequaat aantal Brønsted zure plekken. Onder zware stoomomstandigheden verhinderde de afgenomen Brønsted

zuurdichtheid de vorming van grotere koolwaterstoffen, onafhankelijk van eventueel aanwezige extra mesoporiën die gevormd zouden zijn door het stomen van de zeoliet. Daarnaast waren de toegenomen diffusie mogelijkheden van het zeoliet ZSM-5 kristal, als resultaat van het stomen, gevolgd onder operando omstandigheden met confocale fluorescentie microscopie. De ophoping van cokemoleculen in het zeoliet ZSM-5 kristal begint aan de randen van het kristal.



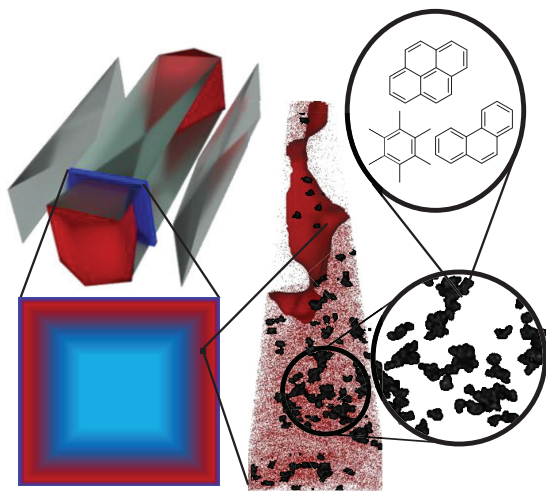
Figuur 6.8. a) Zeoliet ZSM-5 poriënsysteem. Schematische weergave van het cokevorming mechanisme van de top en zijde oriëntaties van een b) P-ZSM-5 c) MT-ZSM-5 d) ST-ZSM-5 kristal. Cokevorming is omschreven met de zwarte gradiënt. De bovenste rij geeft de top oriëntatie van de kristallen weer en de onderste rij laat de zijde oriëntatie van het zeoliet ZSM-5 kristal zien.

Doordat stomen de diffusie mogelijkheden vergroot, werd de vorming van complexe en geconjugeerde coke moleculen voorkomen onder MTH omstandigheden. De voornaamste bevindingen van dit Hoofdstuk zijn samengevat in Figuur 6.8.

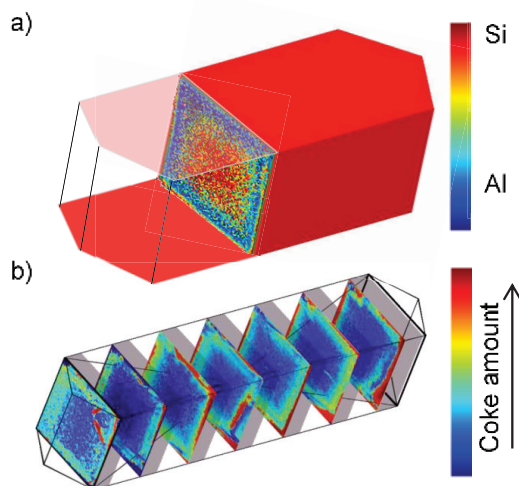
In Hoofdstuk 4 wordt in plaats van te focussen op de hydrothermaal behandelde zeoliet kristallen, de elementsamenstellingen van zeoliet ZSM-5 kristallen bestudeerd, en hun relatie met de plaatselijke cokevorming tijdens de MTH reactie. We hebben de methode van ion massa spectrometrie ontwikkeld en gebruikt om de Brønsted zure plekken in het zeoliet ZSM-5 kristal te onderscheiden via de Al distributie, tot op de nanoschaal. Gelijktijdig zijn we in staat geweest om de coke distributie in deze kristallen, blootgesteld aan de MTH reactie, te bepalen. Heterogeniteiten zijn gevonden binnenin het ZSM-5 kristal, aangezien we een sub- μm dikke silica 'korst' arm aan aluminium hebben waargenomen. Vervolgens werd een paar μm dikke aluminium rijke laag gevonden na de oppervlakte silicaliet laag. Daarnaast nam de hoeveelheid aluminium geleidelijk af richting de kern van het zeoliet ZSM-5 kristal. Dit is schematisch weergegeven in Figuur 6.9a. Het monitoren

van de elementen distributie van het zeoliet ZSM-5 kristal op de nanoschaal heeft erop gewezen dat het twee-componenten model toepasbaar is op het ZSM-5 kristal, wat betekent dat er zes piramidale sub-eenheden aanwezig zijn. Ion massa spectrometrie heeft verder laten zien dat er diffusie barrières aanwezig zijn op de gedeelde facetten van de zes sub-eenheden. Koolstofhoudende soorten beginnen te vormen dichtbij de oppervlakte gebieden waar Brønsted zure plekken aanwezig zijn, en dringen dieper

door in het zeoliet kristal naarmate de reactie vordert. De cokemoleculen worden groter in hun moleculaire grootte bij langere reactie tijd en accumuleren bij de Al regio van het kristal, ondanks dat ze ook accumuleren bij diffusie barrières. The coke verdeling in een zeoliet ZSM-5 kristal is te zien in Figuur 6.9b. Uiteindelijk leidt het MTH proces onder diffusie limitatie, dat wellicht gezien kunnen worden als de voornaamste reden voor de deactivatie van de katalysator.



Figuur 6.10. Reconstructie van een APT naald. De locatie van de naald uit het zeoliet ZSM-5 kristal is weergegeven in het paneel (linksonder). De ^{13}C ionen zijn weergegeven in rood samen met de geïdentificeerde ^{13}C clusters (zwart). Mogelijke cokemoleculen aanwezig in deze clusters zijn aangegeven (rechtsboven).



Figuur 6.9 a) Si/Al verdeling binnenin een zeoliet ZSM-5 kristal b) Coke verdeling binnenin een ZSM-5 kristal.

Hoofdstuk 5 illustreert het laatste stukje in de puzzel van hoe cokevorming plaatsvindt binnenin een zeoliet ZSM-5 kristal tijdens het MTH proces. In dit hoofdstuk omschrijven we de eerste toepassing van Atoom Probe Tomografie (APT) op zowel verse als deels gedeactiveerde zeoliet ZSM-5 kristallen. De succesvolle toepassing van APT op een katalytisch systeem dat beiden

organische en anorganische stoffen bevat heeft de exacte atoomposities aangetoond in de zeoliet ZSM-5 structuur. De verdeling van zeoliet structuur atomen en de koolstof atomen uit de gevangen koolstof houdende soorten is bepaald met sub-nanometer resolutie. Door de permanente vernietigende natuur van de APT methode, konden we niet de exacte moleculaire structuur van de gevormde koolstof houdende soorten bepalen, maar we konden wel een schatting maken van het aantal koolstof atomen dat aanwezig is rondom de Brønsted zure plekken. Een typische koolstofcluster grootte ligt tussen de 36 en 69 koolstof atomen. Deze observaties zijn in overeenstemming met het voorgestelde koolwaterstof-bad mechanisme, zoals voorgesteld door Dahl en Kolboe, en kort besproken in Hoofdstuk 1. Een samenvatting van de voornaamste bevindingen uit Hoofdstuk 5 zijn weergegeven in Figuur 6.10. Het algemene overzicht van onze complementaire zeoliet karakterisering benaderingen zijn geïllustreerd in Figuur 6.5.

Het doel van dit proefschrift was om een grotere kennis te vergaren over het mechanisme, en de oorzaken voor katalysator deactivatie te vinden van zeoliet ZSM-5 kristallen tijdens het MTH proces. Als we al het gepresenteerde werk beschouwen, kunnen we wat meer algemene conclusies trekken. De grote zeoliet ZSM-5 kristallen, gebruikt in dit onderzoek, zijn inderdaad inherent heterogeen. Ze hebben een silicaat korst dat opgevolgd wordt door een geleidelijk afnemende Al regio richting de zeoliet ZSM-5 kristal kern. De Al atomen aanwezig in de zeoliet ZSM-5 structuur leiden tot de vorming van Brønsted zure plekken, welke de actieve plekken zijn voor de koolwaterstof omzettingsprocessen. Omdat de Al verrijking vooral op de rand plekken is, vormen de cokemoleculen voornamelijk in het buitenste oppervlakte en bijna-oppervlakte gebieden in het zeoliet ZSM-5 kristal dat bestudeerd is. De afnemende ruimtelijke beperkingen in de buitenste korst maken het mogelijk de vergrote pseudo-grafiet koolstofhoudende moleculen te vormen en leiden tot een gehinderd moleculair transport. De diffusiebarrières, die anisotropische diffusie veroorzaken, zijn intrinsiek aan de grote zeoliet ZSM-5 kristal structuur en versnellen de deactivatie van de katalysator. Ook hebben we post-behandeling methodes, bijvoorbeeld het stomen van de ZSM-5 op twee verschillende temperaturen, toegepast om zo de moleculaire transporteigenschappen én de zuurheid van het katalysatormateriaal te veranderen. Stomen leidt tot een toename in de hoeveelheid aan heterogeniteiten in de zeoliet ZSM-5 kristallen. De vorming van mesoporiën, Al migratie en de toename van extra-structuur Al soorten vond ook plaats. Al deze aanpassingen voorkwamen de verdere conjugatie van koolwaterstoffen en zorgde voor een betere diffusie van de reactie soorten, maar wel ten koste van een afnemende totale activiteit. Deze waarnemingen zijn schematisch weergegeven in Figuur 6.12.

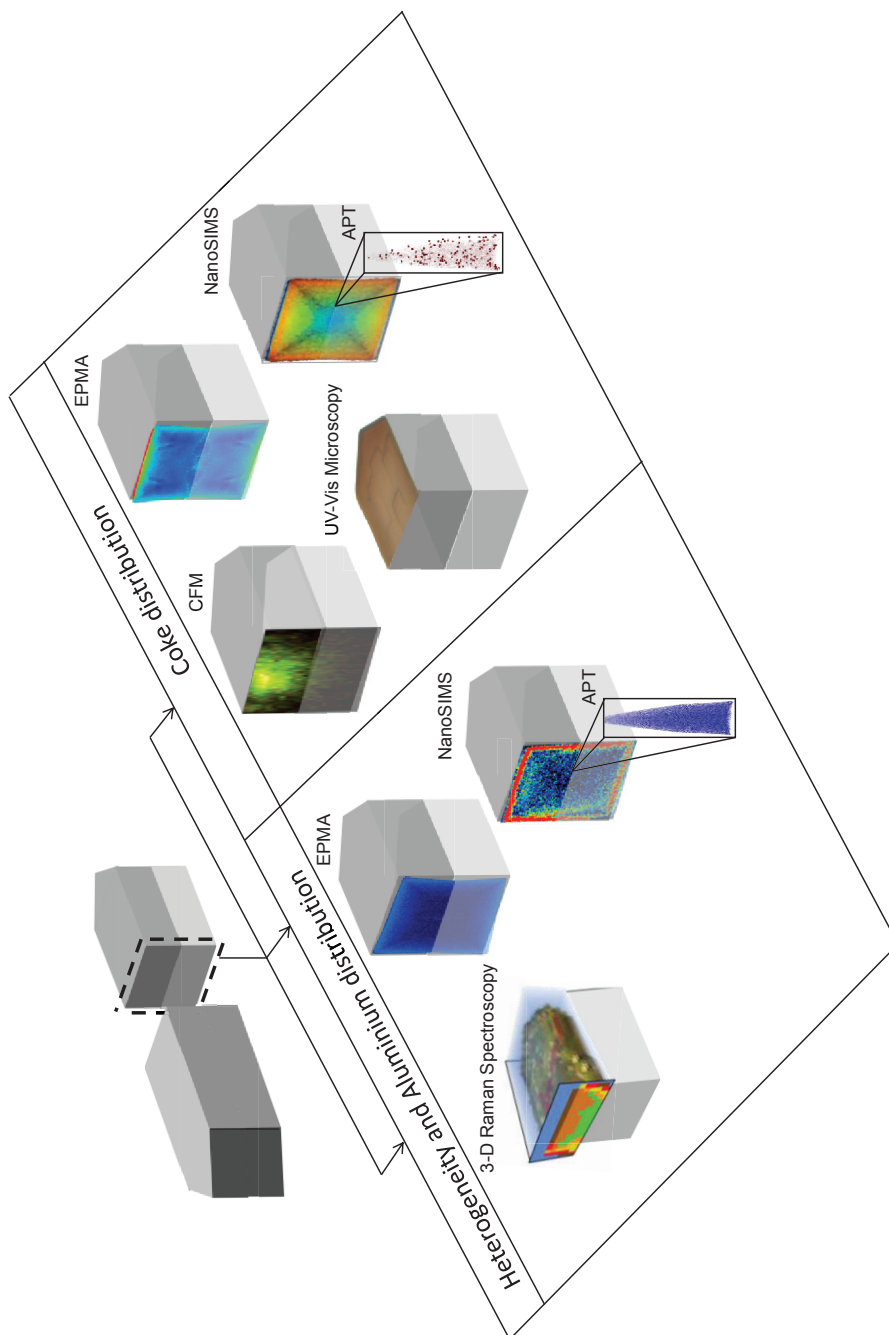
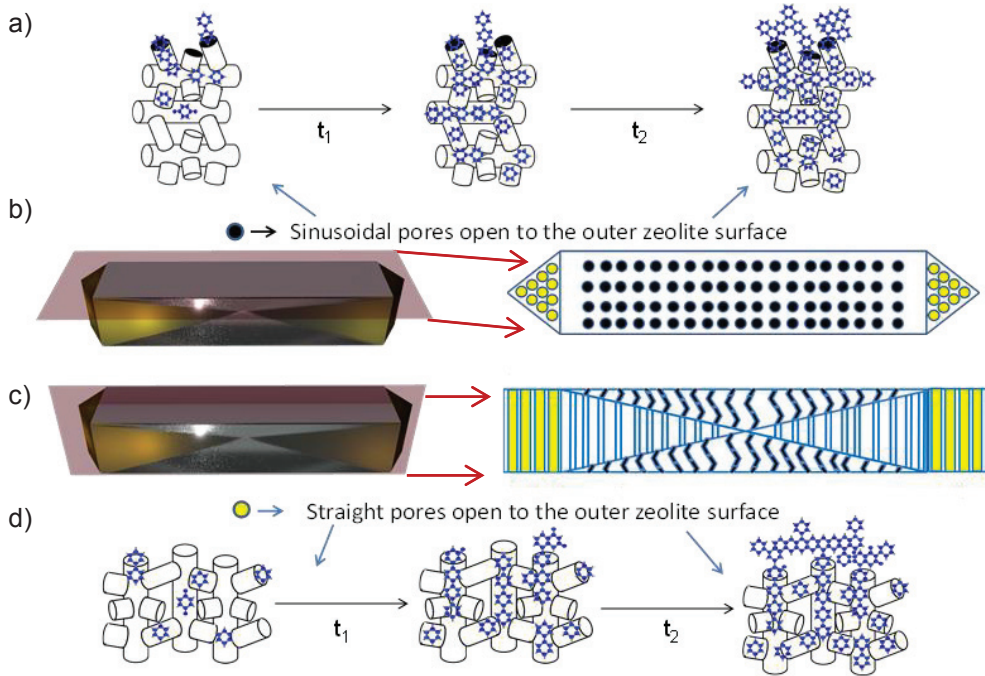


Figure 6.11. Het algemene overzicht van de technieken gebruikt voor de karakterisatie van zeoliet ZSM-5 kristallen gebruikt voor het MTH proces in dit proefschrift.



Figuur 6.6. a) Oppervlakte dekking van cokemoleculen gevormd tijdens het MTH proces in het sinusoïde porie systeem, welke open is vanuit het buitenste zeolietoppervlak in het rechthoekige gebied van het bovenste oppervlak ($t_1 < t_2$). b) Links: weergave van de horizontale dwarsdoorsnede van het zeoliet ZSM-5 kristal oppervlakte, met rechts de schematische weergave van porie oriëntaties op het kristal oppervlak. c) Links: weergave van een verticaal en mediaal dwarsdoorsnede van het zeoliet ZSM-5 kristal, met rechts de schematische weergave van porie oriëntaties in dit gebied (binnenkant van het kristal). d) Oppervlakte dekking van cokemoleculen gevormd tijdens het MTH proces in het rechte poriesysteem, welke open is in de driehoekige gebieden van het bovenste zeolietoppervlak.

List of Abbreviations

AFM	Atomic Force Microscopy
APT	Atom Probe Tomography
CA	Cluster Analysis
CFM	Confocal Fluorescence Microscopy
CHA	Zeolite Framework Structure Chabazite
CCD	Charge-Coupled Device
DNL-6	Zeolite Dalian National Laboratory-6
DME	Dimethyl ether
EPMA	Electron Probe Micro-Analysis
FAU	Zeolite Framework Structure Faujasite
FER	Zeolite Framework Structure Ferrierite
FDA	Frequency Distribution Analysis
FIB-SEM	Focused-Ion-Beam Scanning Electron Microscope
FIM	Field Ion Microscope
FTIR	Fourier-Transform Infrared Spectroscopy
FTS	Fischer Tropsch Synthesis
FWHM	Full Width Half Maximum
HCP	Hydrocarbon Pool Mechanism
HMB	Hexamethylbenzene
ISA	Isosurface Analysis
IZA	International Zeolite Association
KPFM	Kelvin Probe Force Microscopy
MFI	Zeolite Framework Structure ZSM-Five
MS	Mass Spectrometry
MT-ZSM-5	Mildly Steamed (at 500 °C) zeolite ZSM-5
MTG	Methanol-to-Gasoline
MTH	Methanol-to-Hydrocarbons
MTO	Methanol-to-Olefins
MTP	Methanol-to-Propylene
NanoSIMS	Nano-Secondary Ion Mass Spectrometry
NMR	Nuclear Magnetic Resonance
NND	Nearest Neighbor Distribution
P-ZSM-5	Parent zeolite ZSM-5
PCA	Principal Component Analysis
PiFM	Photoinduced Force Microscopy
PMB	Pentamethylbenzene
RDF	Radial Distribution Function
S/N	Signal-to-Noise ratio
SAPO-34	Molecular Sieve Silico-Alumino-Phosphate-34
SAXS	Small Angle X-Ray Scattering
SMS	Surface Methoxy Species
ST-ZSM-5	Severely Steamed (at 700 °C) zeolite ZSM-5
TERS	Tip Enhanced Raman Spectroscopy
TMB	Trimethylbenzene
ToF-SIMS	Time-of-Flight Secondary Ion Mass Spectrometry

TON	Zeolite Theta-ONE
TPA	Tetrapropylammonium
USY	Zeolite Ultrastable Y
UHV	Ultra-High Vacuum
UV	Ultra Violet
WDX	Wavelength Dispersive X-Ray Spectroscopy
XEOL	X-Ray Excited Optical Luminescence
XRD	X-Ray Diffraction
ZSM-5	Zeolite Socony Mobil-5

List of Publications

Coke Formation in a Zeolite Crystal During the Methanol-to-Hydrocarbons Reaction as Studied with Atom Probe Tomography

J. E. Schmidt, J. D. Poplawsky, B. Mazumder, Ö. Attila, D. Fu, D. A. M. de Winter, F. Meirer, S. R. Bare, B. M. Weckhuysen; *Angew. Chem. Int. Ed.* **2016**, *55*, 11173–11177.

Nanoscale Infrared Imaging of Zeolites using Photoinduced Force Microscopy

D. Fu, K. Park, G. Delen, Ö. Attila, F. Meirer, D. Nowak, S. Park, J. E. Schmidt, B. M. Weckhuysen; *Chem. Commun.* **2017**, *53*, 18–21.

Isolating Clusters of Light Elements in Molecular Sieves with Atom Probe Tomography

J.E. Schmidt, L. Peng, A. L. Paioni, H. Ehren, W. Guo, B. Mazumder, D. A. M. de Winter, Ö. Attila, D. Fu, A. D. Chowdhury, K. Houben, M. Baldus, J. D. Poplawsky, B. M. Weckhuysen, submitted for publication.

Coke Formation during the Methanol-to-Hydrocarbons Conversion over a Zeolite H-ZSM-5 Crystal as probed with Nano Secondary Ion Mass Spectrometry and Electron Micro-Probe Analysis

Ö. Attila, D. A. M. de Winter, R. Brand, M. V. M. Kienhuis, L. Polerecky, F. Meirer, and B. M. Weckhuysen, in preparation.

3-D Raman Spectroscopy of Zeolite ZSM-5 Crystals

Ö. Attila, H. E. King, F. Meirer, and B. M. Weckhuysen, in preparation.

Oral Presentations

3-D Raman Spectroscopy of Large Zeolite ZSM-5 Crystals

Ö. Attila, H. E. King, F. Meirer and B. M. Weckhuysen, New perspectives in chemical analysis with correlative New perspectives in chemical analysis with correlative 3-D Raman Imaging, Utrecht, The Netherlands 19-20 July 2018

Multiscale Investigation of Zeolite Deactivation during Hydrocarbon Conversion Processes

Ö. Attila, D. A. M. de Winter, J. E. Schmidt, J. D. Poplawsky, B. Mazumder, D. Fu, R. Brand, S. Matveev, M. V. M. Kienhuis, L. Polerecky, F. Meirer, S. R. Bare and B. M. Weckhuysen, 13th European Congress on Catalysis, Florence, Italy, 27-31 August 2017

Investigation of Zeolite Deactivation during Hydrocarbon Conversion

Ö. Attila, D. A. M. de Winter, R. Brand, S. Matveev, M. V. M. Kienhuis, L. Polerecky, F. Meirer, and B. M. Weckhuysen, 18th NCCC, Noordwijkerhout, The Netherlands, 7-9 March 2017

Poster Presentations

Nanoscale Chemical Imaging of Carbon Deposits on Zeolite H-ZSM-5 Crystals with Secondary Ion Mass Spectrometry

Ö. Attila, D. A. M. de Winter, R. Brand, M. V. M. Kienhuis, L. Polerecky, F. Meirer, and B. M. Weckhuysen, 25th North American Catalysis Society Meeting, Denver, United States of America, 4-9 June 2017

Chemical Imaging of Carbon Deposits on Zeolite ZSM-5 Crystals with Secondary Ion Mass Spectrometry

Ö. Attila, D. A. M. de Winter, R. Brand, M. V. M. Kienhuis, L. Polerecky, F. Meirer, and B. M. Weckhuysen, CHAINS 2016, Veldhoven, the Netherlands, 6-8 December 2016

Investigation of zeolite deactivation during hydrocarbon conversion processes using NanoSIMS

Ö. Attila, D. A. M. de Winter, R. Brand, M. V. M. Kienhuis, L. Polerecky, F. Meirer, and B. M. Weckhuysen, 17th NCCC, Noordwijkerhout, The Netherlands, 7-9 March 2016

Chemical Imaging of Carbon Deposits on Zeolite ZSM-5 Crystals with Secondary Ion Mass Spectrometry

Ö. Attila, D. A. M. de Winter, R. Brand, M. V. M. Kienhuis, L. Polerecky, F. Meirer, and B. M. Weckhuysen, Pathways to Sustainability Symposium 2016, Utrecht, The Netherlands, 28 October 2016

Chemical Imaging of Large H-ZSM-5 Zeolite Crystals with NanoSIMS

Ö. Attila, D. A. M. de Winter, R. Brand, M. V. M. Kienhuis, L. Polerecky, F. Meirer, and B. M. Weckhuysen, NanoSIMS user meeting 2016, Utrecht, The Netherlands, 26-27 September 2016

Acknowledgments

Flashbacks are the most hurtful parts of every farewell. While this journey is coming to an end, I am embracing all the flashbacks of my last four years with some of the most special people I met in this remarkable research group ICC.

First of all I would like to sincerely thank my supervisor Bert. When he gave me the chance of being a member of the ICC family, I could not dare to imagine all the possibilities I would achieve during these four years of my life. This ride went with all its ups and downs, thrills and chills and finally arrived to its final destination. As I am departing to my next path I can only tell my appreciation towards Bert for teaching me all the valuable lessons that will be cornerstones of my yet unexplored future adventures.

Iris, it has been some time since you became my other half. I have discovered so much about myself during our time together. I cannot thank you enough for being by my side in my good or bad days. This thesis might not have been completed without your support.

Benim bu yaşıma gelmemde, benliğime kavuşmamda hiçbir engel tanımaksızın yanımda olan aileme yazılı veya sözlü olarak kurabileceğim tümceler onlara karşı olan sevgi ve minnet ile dolu duygularımı anlatmak için yeterli gelmiyor. Ne bugün yazdığım doktora tezi, ne de hayatımda başarabildiğim hiçbirşey sizin destekleriniz olmadan elbette ki olmazdı. Biliyorum ki son 12 yıldır fiziksel olarak yanınızda bulunamadım. Fakat on sekiz yaşımda sizlerden uzaklarda bir hayata adım attığım günden beri size karşı olan özlemim hiç azalmadı, aksine katlanarak arttı. Biliyorum ki sizler de bu satırları okurken zamanda kısa bir yolculuğa çıkacaksınız. Umuyorum bu yolculuk, gurur ve sevinç yollarından geçsin, asla üzüntü sapaklarına sapsın. Size edebileceğim teşekkürleri bu kitaba sığdıramayacağımı belirterek yine de sizlere çok teşekkür ediyorum. İyi ki varsınız.

Every story is only as good as the powerful characters it contains. I was fortunate enough to meet, work and learn from so many astonishing people on the way. I would like to thank Zafer for being the first person I met in the group who helped me in adapting to my new reality.

Since my first days, I knew that I was very lucky to be neighbors with Pasi, Ivan, Sang-ho, Antonio, Sandra and Fang. I am cherished to be with you through my professional and private life. From work place to concerts, from dinner parties, to trips I have learned a lot from you and enjoyed my time very much. Thank you for your patience with me.

My PhD work in the ICC consisted of many trips to far-lands. These journeys were not possible with all the most amazing scientists and engineers. I would like to specially thank to the people who joined my experimental trips which became a big part of this PhD thesis. Thank you so much Pasi, Joel, Donglong, Tom D., Thomas G. and Zoran. You as capable scientists and engineers were not only doing an excellent work no matter if there is a >14h shift or not, but you were great travel companions as well.

Dear postdoc room residents Matthijs, Tao, Jan F. and Pierre; It was a pleasure for me to be in the same professional environment with you and more importantly spending time outside of work hours. I have spent some of my greatest times in my time in Utrecht while I was having a conversation with you no matter the subject was. Thank you for sharing your perspectives with me.

I already miss the lunches at the “Michelin star worthy” UMC cafeteria. I would like to thank to the lunch team of Matthias F., Abhishek, Gareth and many more for making the lunch breaks special.

I would like to thank Lennart for the magical time I had at ICC. I would like to thank Laurens for helping his work in my thesis and for being such a great person.

I have already counted so many brilliant researchers in ICC however, it is not possible to forget all the supportive staff (heroes) of the group who helped me in my time in the department. I would like to thank AdE, AdM, Marjan, Oscar, Ramon, Monique and Dymph.

I would like to thank Florian for his support on my time at ICC. You helped me a lot academically but also you supported me throughout my PhD work. I really appreciate your help and guidance.

Dear Ahmed, Beatriz L., Beatriz C., Boyang, Carlos, Egor, Frank H., Gang, Heba, Katarina, Katinka, Koen, Marjolein, Marthe, Marianna, Martin, Matteo, Miguel, Naresh, Nazila, Nikos, Rogier, Patric, Peter B., Peter N., Rolf, Roozbeh, Rupan, Sam, Silvia, Stanislav, Suzanne and Thomas H., Yannis and all the other past and the current ICC members, I would like to thank you all for being such great coworkers.

Olia, you were the first person I already knew before I came to the Netherlands. I am very glad you are still in my life. Thank you for your ongoing support. I wish you a very happy life with Greg.

Arda, Grkem ve Onur. Beyler elbette sizleri de bu sayfalara eklemem zaruri bir ihtiya. On yıldan fazladır hayatımdaki en önemli itici güçlerden biri olduğunuz için teşekkür ederim. Günlük, haftalık veya aylık psikoterapi seansları sanırım beni ayakta tutan, kariyerimde ve şahsi hayatımda beni şu anda bulunduğum yere getiren başlıca sebeplerin arasındadır. Sizler de iyi ki varsınız.

Stories only end to give space to the beginning of new ones. The time between hello and goodbye in this story is over.

So long and thank you for the ride.

About the author

Özgün Attila was born on March 15th 1988 in Izmir, Turkey. At the age 18, he started his academic career in the Department of Chemical Engineering of the Middle East Technical University (Ankara, Turkey). In 2011 he obtained his Bachelor degree after completing his finishing project on “DME synthesis”. In the same year, upon obtaining his bachelor degree, he started his Master degree in Energy Science and Technology at Ulm University (Ulm, Germany). In the second year of his master studies, he started his internship in the laboratory of Prof. Dr. Rolf Jürgen Behm working on the characterization of gold catalysts used in CO oxidation. 6 months into his internship, he started his Master thesis on the same topic. In 2014 he completed his studies and thesis, entitled “Oxygen-assisted carbonate decomposition on highly dispersed gold/ceria catalysts”. Upon his graduation in 2014, he started working as a PhD candidate in the Inorganic Chemistry and Catalysis group at Utrecht University (Utrecht, the Netherlands) under the supervision of Prof. Dr. Ir. Bert Weckhuysen. His research formed the basis of this PhD thesis.

Dünyada her şey için, maddiyat için, maneviyat için, hayat için, başarı için en hakiki yol gösterici ilimdir, fendir. İlim ve fennin dışında yol gösterici aramak gaflettir, cahilliktir, doğru yoldan sapmaktır. Yalnız ilmin ve fennin yaşadığımız her dakikadaki safhalarının gelişimini anlamak ve ilerlemeleri zamanında takip etmek şarttır.

-M.K. Atatürk, 1924

